3

The Recent Development of Rare Earth-Doped Borate Laser Crystals

Chaoyang Tu* and Yan Wang
Key Laboratory of Optoelectronic Materials Chemistry and Physics of CAS, Fujian Institute of Research on the Structure of Matter, Chinese Academy of Sciences, P. R. China

1. Introduction

As a laser host, borates possess favourable chemical and physical characteristic and higher damnification threshold. $Ln_2Ca_3B_4O_{12}$ (Ln = La, Gd, or Y) double borate family crystals,$Ca_3(BO_3)_2$ (CBO) and LaB_3O_6 crystals are the potential laser host materials. They have the suitable hardness and good chemical stability and are moisture free. Furthermore, they melt congruently and can be grown by Czochralski method [1-5], so the high optical quality crystal with large dimension can be easily grown.

The $Ln_2Ca_3B_4O_{12}$ (Ln = La, Gd, or Y) double borate family was first grown by the Czochralsky method with the Nd^{3+} doping[3,5]. The orthorhombic crystallographic structure of Yb^{3+}-doped $Y_2Ca_3B_4O_{12}$ (CYB) was determined in Ref. [6], it is made of three sets of M-oxygen distorted polyhedrons and three sets of BO_3 planar triangles. The Yb^{3+}, Y^{3+} and Ca^{2+} cations occupy statistically the three M sets. This structure disorder contributes to the line broadening of spectra of rare earth doping ions, such as Yb^{3+}, Nd^{3+}, and can lead to a tunable laser.

In the rare earth-doped CBO crystal, the rare earth ions substitute for the divalent cation (Ca^{2+}) and charge compensation is required. Because of the charge compensation effects, the rare earth-doped CBO crystals show partly distorted structure, and the inhomogeneous broadening of the emission similar to amorphous materials can be also expected.[7]

Furthermore, rare earth-doped LaB_3O_6 crystal can serve as a microchip laser crystal without any processing because of the cleavage of LaB_3O_6 crystal[8~10].

The study on the rare earth-doped $Ca_3(BO_3)_2$, LaB_3O_6 and $Ca_3Re_2(BO_3)_4$ laser crystals will be covered in this chapter. The growth, thermal, optical and spectrum characteristics of these crystals are presented. Their laser characteristics are also covered.

2. Rare earth-doped $Ca_3(BO_3)_2$ crystals

$Ca_3(BO_3)_2$ (CBO), which belongs to the trigonal system with the space group R_{-3C}, and the cell parameters are as follows: a=b=8.6377(8) Å, c=11.849(2) Å, v=765.61 Å^3, z=6, and Dc=3.096 g/cm^3 is a good laser host material. It has the suitable hardness and good chemical

---

*Corresponding Author

stability and is moisture free. The Ca^{2+} ion in CBO is surrounded by eight nearest oxygen to form a distorted polyhedron, in which the only symmetry is a two-fold axis passing through the Ca ion. Thereby the calcium ions belong to the C_2 point symmetry. As in this borate the trivalent rare earth ion is introduced on the divalent cation site, a mechanism for charge compensation should be considered.

2.1 The crystal growth

Pure, Er^{3+}-, Dy^{3+}-, and Nd^{3+}-doped CBO crystals were grown by the Czochralski method along the [0 1 0] orientation (by using the *b*-axis seeds). The raw materials were analytical grade, $CaCO_3$, H_3BO_3, Na_2CO_3, and some spectral grade, Dy_2O_3, and Nd_2O_3. In fact, in the case of rare earth-doped CBO crystal, the co-doping Na_2CO_3 as charge compensator was introduced to obtain crystal with a large concentration of the rare earth ions. The melt composition ratio of $CaCO_3$ and H_3BO_3 is 3:2 for the pure CBO and rare earth (RE)-doped CBO crystals according to the following reactions:

$$(3\text{-}6x)\ CaCO_3 + 2H_3BO_3 + 3x/2\ Na_2CO_3 + 3x/2\ Ln_2O_3 = (Ca_{1\text{-}2x}Na_xLn_x)_3(BO_3)_2$$

$$+\ 3H_2O\uparrow +\ (3\text{-}9x/2)\ CO_2\uparrow$$

The polished sample of the pure CBO crystal is shown in Fig.2.1. Its optical homogeneity was determined using Zygo optical interferometer (shown in Fig.2.2). Its homogeneity is 2.57×10-5, and its thickness is 5.00 mm.

2.2 The thermal characteristic

Measurements of thermal expansion have greatly increased our knowledge of material properties such as lattice dynamics, electronic and magnetic interactions, thermal defects, and phase transitions [12]. As a significant part of the power pump is converted into heat inside the material during laser operation, it is important to know its linear thermal expansion coefficients to predict how the material behaves when the temperature increases [13]. The figure of linear expansions versus temperature was shown in Fig.2.3. The linear thermal expansion coefficient is defined as:

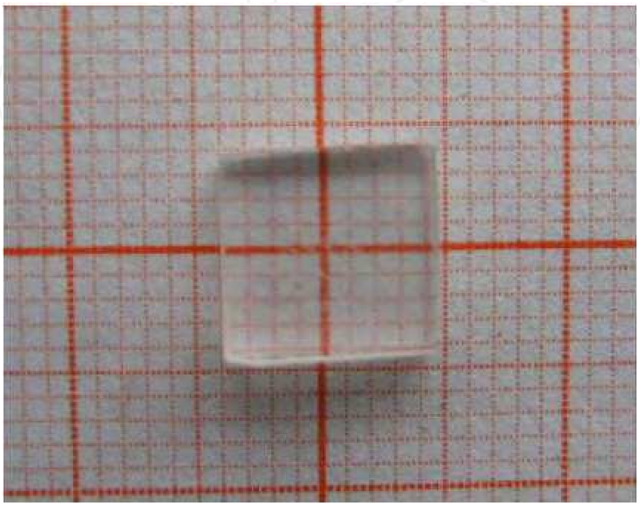

Fig. 2.1. The polished sample of the pure CBO crystal

Fig. 2.2. Interference fringe of CBO crystal.

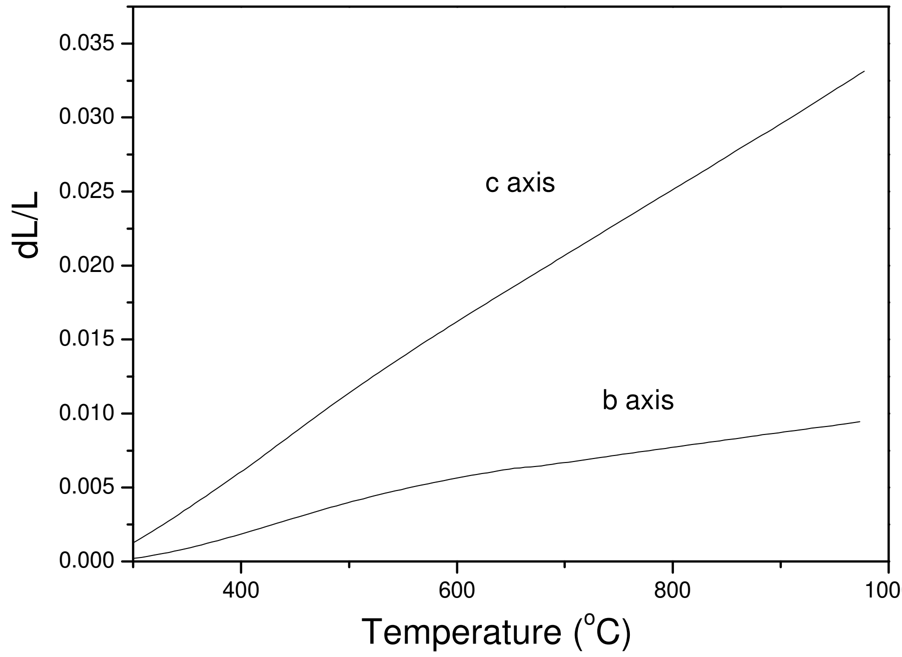

Fig. 2.3. Thermal expansion of the CBO crystal

$$\alpha = \frac{1}{T}\frac{\Delta L}{\Delta T} \tag{2.1}$$

Where L is the initial length of the sample at room temperature and ΔL is the change in length when the temperature changes ΔT. We can calculate the thermal expansion coefficient from the slope of the linear fitting of the linear relationship between $\Delta T/T$ and the temperature. In this case, the linear thermal expansion coefficients for different crystallographic directions c-, and b-axes are 4.69×10^{-5} K^{-1}, 1.37×10^{-5} K^{-1}, respectively[14]. The thermal expansion coefficients of the *a* and *b* axes are comparable. Thermal expansion coefficient along the *c*-axis is about two times larger than those of *b* and *a* axes. Although the thermal expansion property of YVO_4 crystal has little different from that of CBO crystal, the CBO crystal has no cleavage plane.

$$\alpha_{ij(CBO)} = \begin{vmatrix} 1.37 & 0 & 0 \\ 0 & 1.37 & 0 \\ 0 & 0 & 4.69 \end{vmatrix} \times 10^{-5}\ {}^{o}C \qquad (2.2)$$

It is well known that the higher the consistency of atom in the crystal structure, the larger the heat expansion coefficient, and vice versa. Obviously, it was demonstrated from the Fig.2.4 that the consistency of atom along c axis is higher than that along b axis, which is comparable to a axis. Therefore, the heat expansion coefficient along c axis is much larger than those along b axis and a axis.

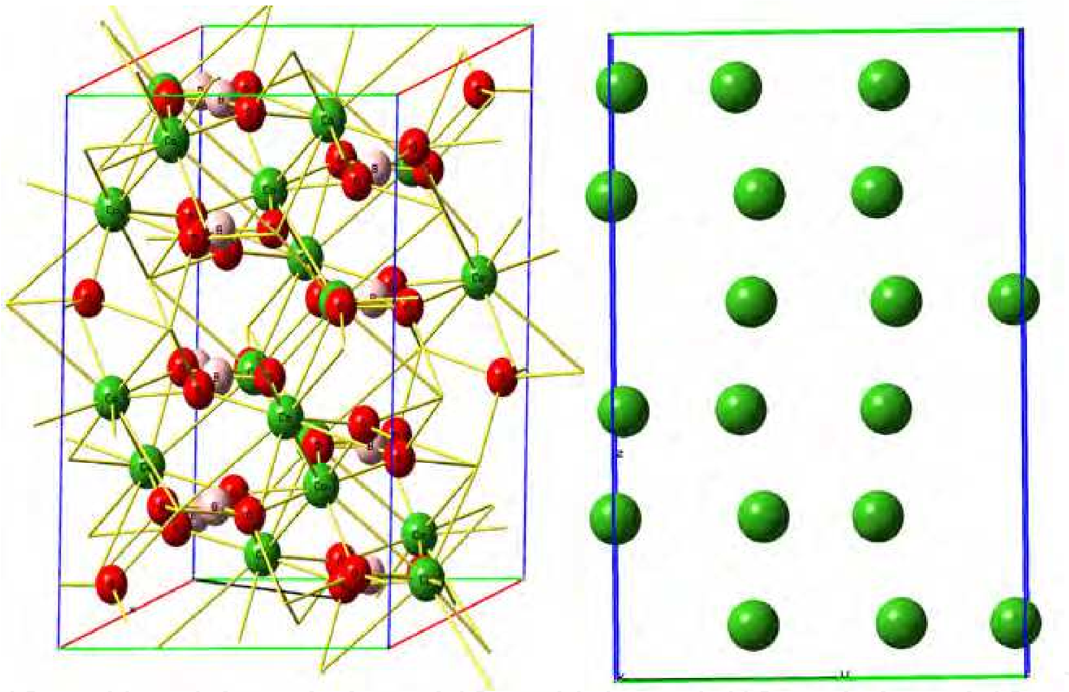

(a) (b)

Fig. 2.4. (a) The structure of CBO crystal; (b) The cb section of the structure of CBO crystal

2.3 The spectrum characteristics

2.3.1 The spectrum characteristics of Nd^{3+}:$Ca_3(BO_3)_2$ crystal

Fig.2.5 shows the transmission spectrum of CBO crystal. It has high transmittance in the 190–3300 nm optical ranges.[14]

Fig.2.6 shows the absorption spectrum measured at room temperature in the 300~950 nm ranges[15]. There are three main strong absorption peaks in the spectrum centered at 588, 751 and 808 nm, respectively, corresponding to the transitions from the $^4I_{9/2}$ ground state. The

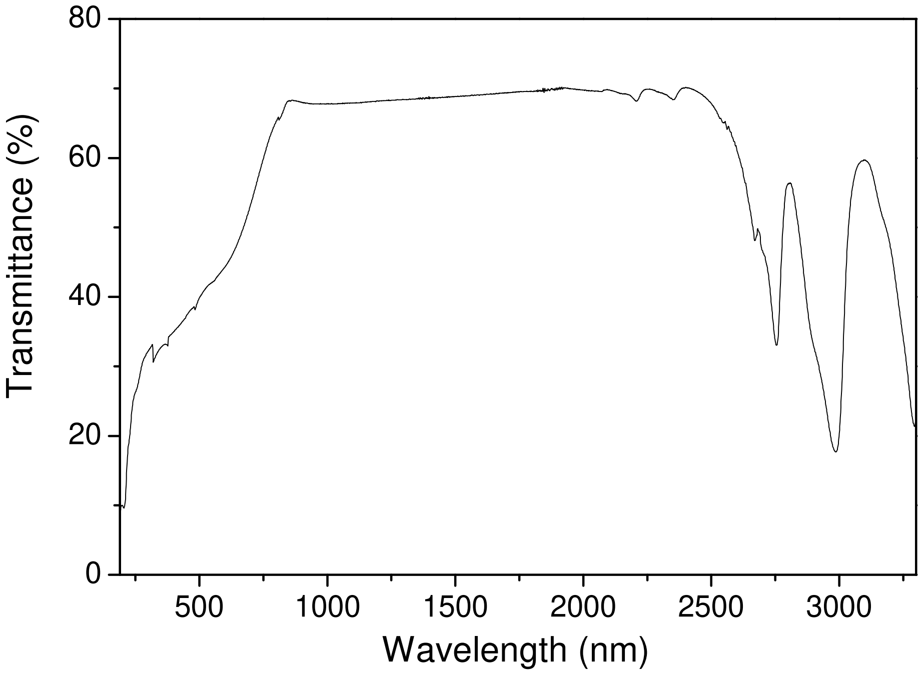

Fig. 2.5. The transmission spectrum of CBO crystal

introduction of Na^+ as charge compensator results in the disorder in the local crystal fields acting on the optically active ions.[16] Therefore, the absorption and emission peaks can become broadening.[17] The full width at half maximum (FWHM) of the absorption peak at 808 nm is about 19 nm, which is larger than that of Nd^{3+}:$GdVO_4$ (FWHM is 4 nm)[18]. The absorption coefficient and absorption cross section of Nd^{3+}:CBO crystal at 808 nm are 0.93 cm^{-1} and 2.12×10^{-20} cm^2, respectively, which are compared with those of Nd^{3+}:$GdVO_4$ (2.0×10^{-20} cm^2 for π spectrum) [20] and Nd^{3+}:YVO_4(2.0×10^{-20} cm^2 for π spectrum) [19]. Therefore, Nd^{3+}:CBO crystal is suitable for GaAlAs laser diode pumping.

Fig.2.7 presents the emission spectrum of Nd^{3+}:CBO crystal, in which there are three main emission peaks in the spectrum centered at 1346, 1060 and 883 nm, respectively, corresponding to the transitions of $^4F_{3/2}\rightarrow{}^4I_J$ (J=13/2, 11/2, 9/2). Table 2-1 lists the line strengths and optical parameters of Nd^{3+} in CBO crystal. Table 2-2 lists the values of intensity parameters of Nd^{3+} in CBO crystal and those of some other well-known Nd-doped laser crystals. Table 2-3 presents the luminescence parameters of Nd^{3+} in CBO crystal for the transitions $^4F_{3/2}\rightarrow{}^4I_J$. The stimulated emission cross-section at 1060 nm is about 8.04×10^{-20} cm^2, which is smaller than those of $NdAl_3(BO_3)_4$ (1.43×10^{-19} cm^2) [26] and Nd^{3+}:$La_2(WO_4)_3$ (11.2×10^{-20} cm^2) crystals [27], but larger than that of Nd^{3+}:LaB_3O_6 (3.46×10^{-20} cm^2) crystal [21]. Fig.2.8 presents the luminescence decay curve excited at 808 nm at room temperature corresponding to the emission line $^4F_{3/2}\rightarrow{}^4I_{11/2}$ at 1060 nm. The fluorescence lifetime of $^4F_{3/2}$ is 43.8μs, and the radiative lifetime is 135.03μs. So the luminescent quantum efficiency of the $^4F_{3/2}$ level is about 32.4%.

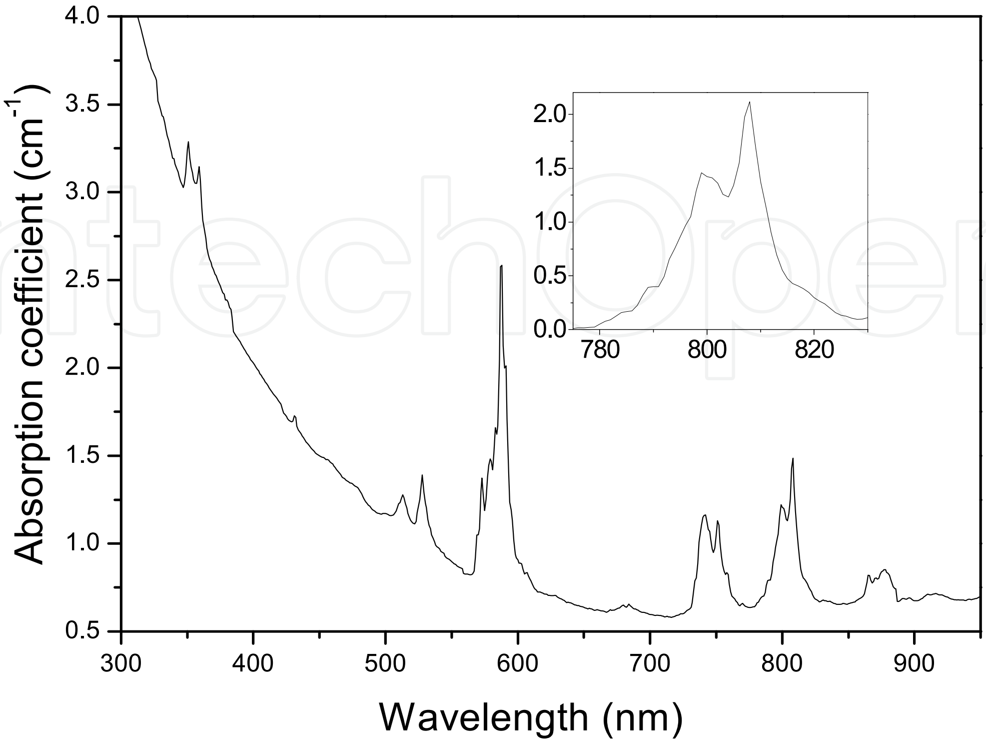

Fig. 2.6. The absorption spectrum of Nd^{3+}:CBO crystal measured at room temperature

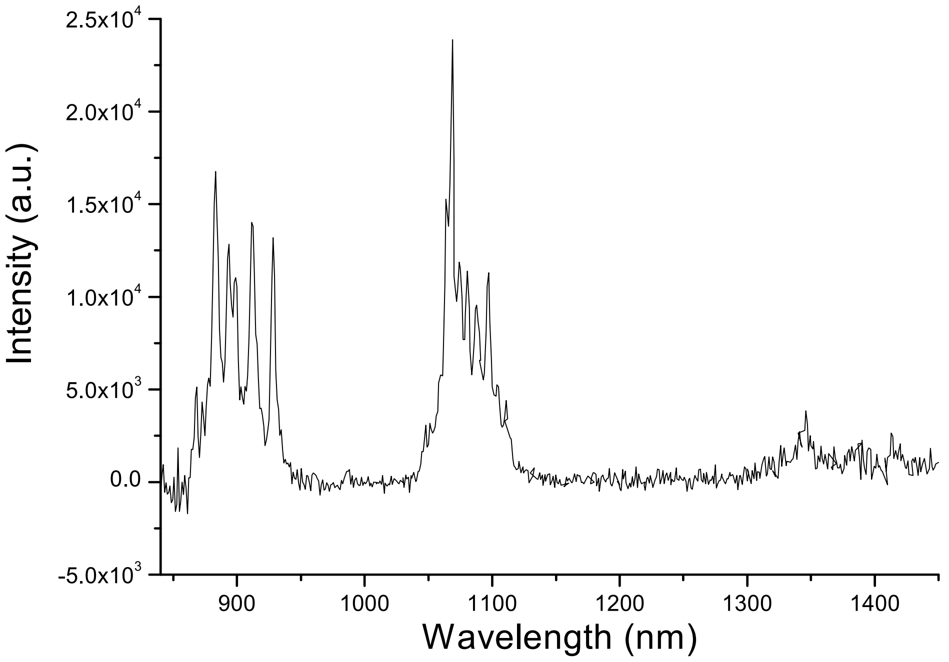

Fig. 2.7. The emission spectrum of Nd^{3+}:CBO crystal

Transition final state	Central wavelength $\overline{\lambda}(nm)$	$S_{mea}(J \rightarrow J')$ (10^{-20} cm^2)	$S_{cal}(J \rightarrow J')$ (10^{-20} cm^2)	$\sigma_{abs}(\lambda)$ (10^{-20} cm^2)
$^4I_{9/2}\rightarrow{}^4D_{1/2}$	359	0.837	0.772	5.342
$^4G_{9/2}$	528	0.920	0.949	2.020
$^4G_{5/2}$	588	5.529	5.529	4.419
$^4S_{3/2}$	751	4.564	4.620	1.373
$^2H_{9/2}$	808	2.475	2.377	2.303

Table 2.1. Line strengths and optical parameters of Nd^{3+} in CBO crystal

Crystal	Ω_2 (10^{-20} cm^2)	Ω_4 (10^{-20} cm^2)	Ω_6 (10^{-20} cm^2)	$\beta_{J'}$ $^4F_{3/2} \rightarrow {}^4I_{11/2}$	Ref.
CBO	4.63	2.40	10.4	0.476	15
NAB	6.07	9.14	14.58	0.518	21
$LaSc_3(BO_3)_4$	5.349	4.124	3.852	0.470	22
LaB_3O_6	0.54	2.31	4.51	0.538	23
YVO_4	4.667	2.641	4.047	0.509	24
$GdVO_4$	12.629	4.828	8.425	0.519	25
$Ca_3Sc_2Ge_3O_{12}$	0.99	4.24	7.14	0.524	26

Table 2.2. The intensity parameters of Nd^{3+} in CBO crystal and those of some other well-known Nd-doped laser crystals

Radiation transition	Radiation wavelength (nm)	$A(J \rightarrow J')$ (s^{-1})	$\beta_{J'}$
$^4F_{3/2}\rightarrow{}^4I_{9/2}$	883	3157	0.426
$^4I_{11/2}$	1060	3529	0.476
$^4I_{13/2}$	1346	720	0.097
$^4I_{15/2}$	1852	37.8	0.001

Table 2.3. The luminescence parameters of Nd^{3+} in CBO crystal for the transitions $^4F_{3/2}\rightarrow{}^4I_J$.

2.3.2 The spectrum characteristics of Er^{3+}:$Ca_3(BO_3)_2$ crystal

Figure.2.9 shows the room temperature (RT) polarized absorption spectra in the **200–1600 nm** spectra region of **Er3**$^{+}$ in the CBO crystal[28]. It consists of a number of groups of lines corresponding to transitions between the ground state $^4I_{15/2}$ and higher energy states inside the **4f** $^{\mathbf{11}}$ electronic configuration of the **Er**$^{\mathbf{3}}$**+** ion. Due to the high $\mathbf{Er^{3+}}$ concentration of the CBO sample, the spectra are well defined. In this sample, eleven absorption bands clearly are located at 1517, 978, 793, 652, 523, 486, 450, 403, 380, 365, and **257 nm**, which correspond to the transitions from $^4I_{15/2}$ to $^4I_{13/2}$, $^4I_{11/2}$, $^4I_{9/2}$, $^4F_{9/2}$, $^2H_{11/2}$, $^4F_{7/2}$, $^4F_{5/2}$, $^2H_{9/2}$, $^4G_{11/2}$, $^4G_{9/2}$ and $^4D_{5/2}$, respectively.

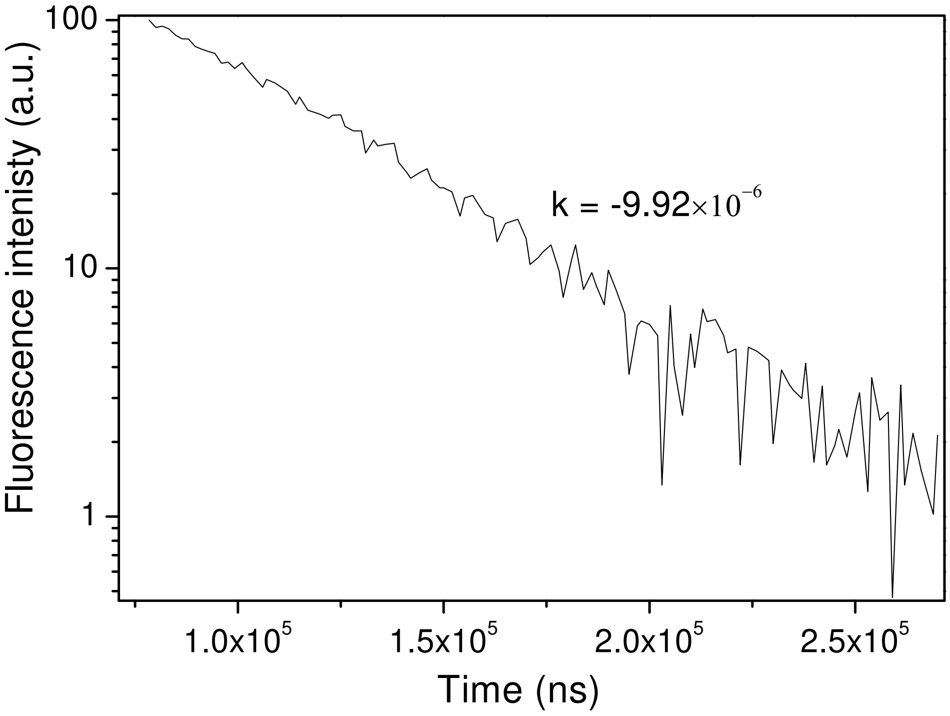

Fig. 2.8. The luminescence decay curve excited at 808 nm at room temperature corresponding to the emission line $^4F_{3/2}\rightarrow{}^4I_{11/2}$ at 1060 nm

Fig.2.10 displays the RT polarized emission spectra (in the **1400–1700 nm** spectral range). The emission spectra obtained under $^4I_{13/2}$ multiplet excitation at **980 nm**. And the fluorescence decay curve of the $^4I_{13/2}\rightarrow{}^4I_{15/2}$ transition is also shown in Fig.2.11. From the curve, the fluorescence lifetime was **2.54ms**.

Fig.2.12 shows the cross sections of the Er^{3+} ions in the CBO crystal. (a) The absorption cross-section, (b) the emission cross-section derived by the reciprocity method (RM), (c) the emission cross-section derived by the Füchtbauer-Ladenburg (FL) formula, and (d) the emission cross-section derived by the modified method. The maximum values of the emission cross section centered at about 1530 nm are 9.67×10^{-21}cm^2 for the π spectrum and 7.43×10^{-21} cm^2 for the σ spectrum, which can be compared with those reported for other Er^{3+} doped laser crystals [9.3×10^{-21} cm^2 for Er^{3+}:LaGaO$_3$,[29] 4.5×10^{-21} cm^2 for Er^{3+}:YAG (yttrium aluminum garnet),[30] and 3.1×10^{-21} cm^2 for Er^{3+}:YAlO$_3$ [30]]. The wavelength dependence of the gain cross-section for several values of population inversion P (P = 0,0.1,0.2,…,1) is shown in Fig.2.13. A wide tunable wavelength range from 1530 to 1650 nm is expected when the population inversion P is larger than 0.5, which is encountered in a free-running laser operation. Table 2-4 displays the experimental, theoretical oscillator strengths for Er^{3+} ions in CBO crystal. Table 2-5 presents the comparison of the Judd-Ofelt parameters of Er^{3+}:CBO and other Er^{3+} doped crystals. Generally, the Ω_2 parameter is sensitive to the symmetry of the rare earth site and is strongly affected by covalency between rare earth ions

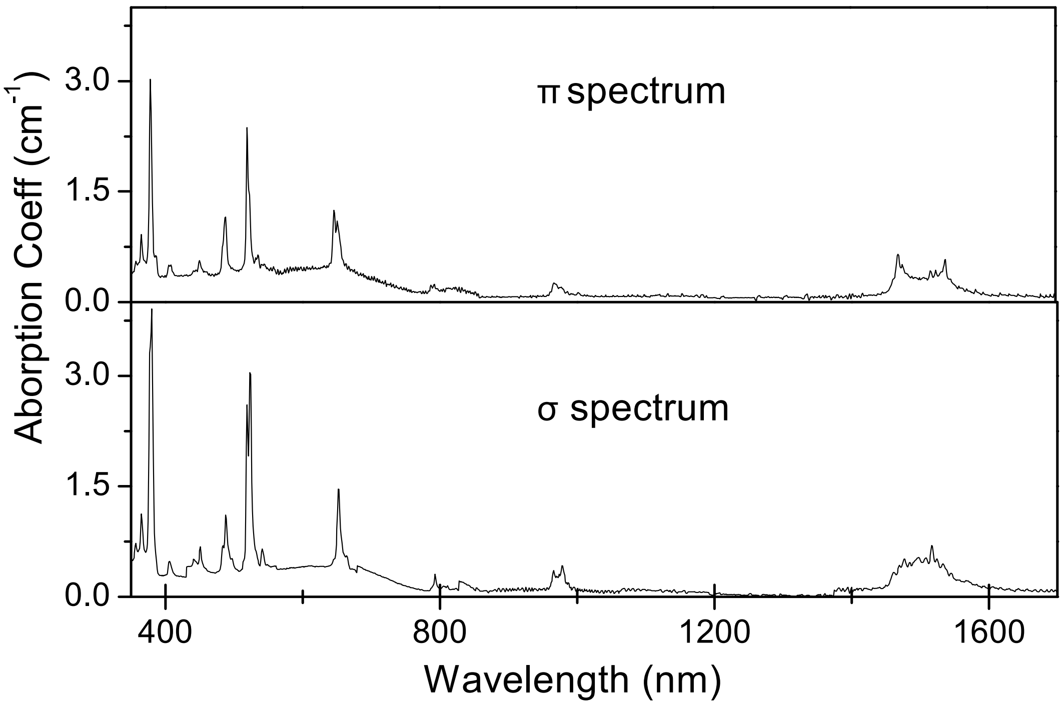

Fig. 2.9. Room temperature (RT) polarized absorption spectra of **Er**$^{3+}$ in the CBO crystal

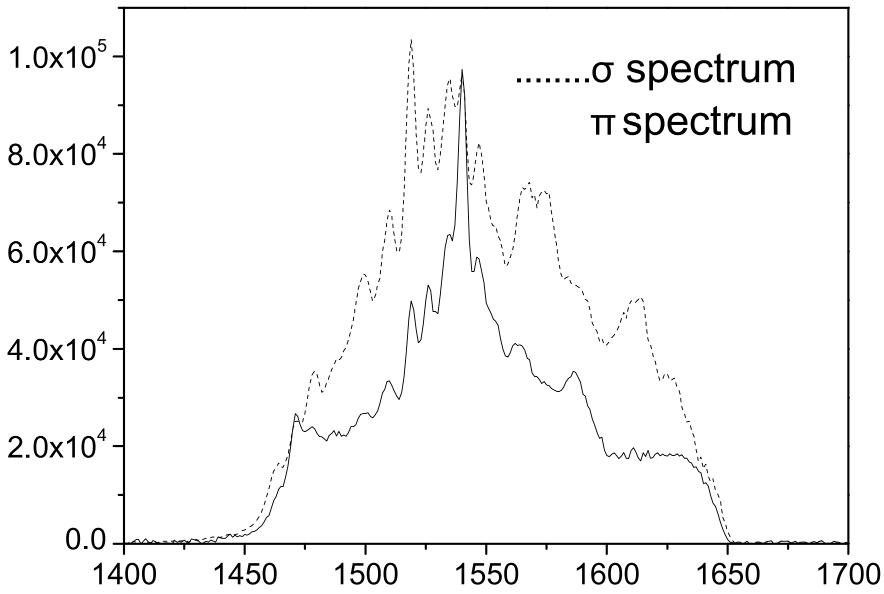

Fig. 2.10. Room temperature polarized emission spectra of the Er^{3+}:CBO single crystal.

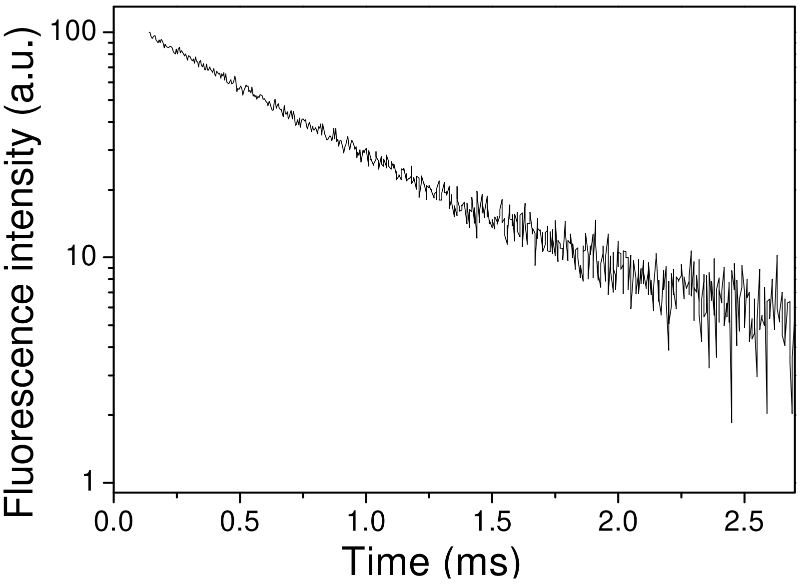

Fig. 2.11. Fluorescence decay curve of the ${}^4I_{13/2} \rightarrow {}^4I_{15/2}$ transition

and ligand anions. In the present work, the parameter Ω_2 is high, but it is lower than those for YVO_4 and $NaBi(WO_4)_2$. This possibly indicated that the Er^{3+} doped CBO crystals are more covalent in character. Table 2-6 displays the radiative transition probabilities $A_{JJ'}$, fluorescence branching ratios $\beta_{JJ'}$, and radiative decay time τ_r for Er^{3+} ions in CBO crystal. From the measured and calculated radiative lifetimes, the luminescent quantum efficiency $\eta=\tau_f/\tau_r$ for the ${}^4I_{13/2}\rightarrow{}^4I_{15/2}$ transition of the Er^{3+} :CBO crystal is found to be approximately 84.4%.

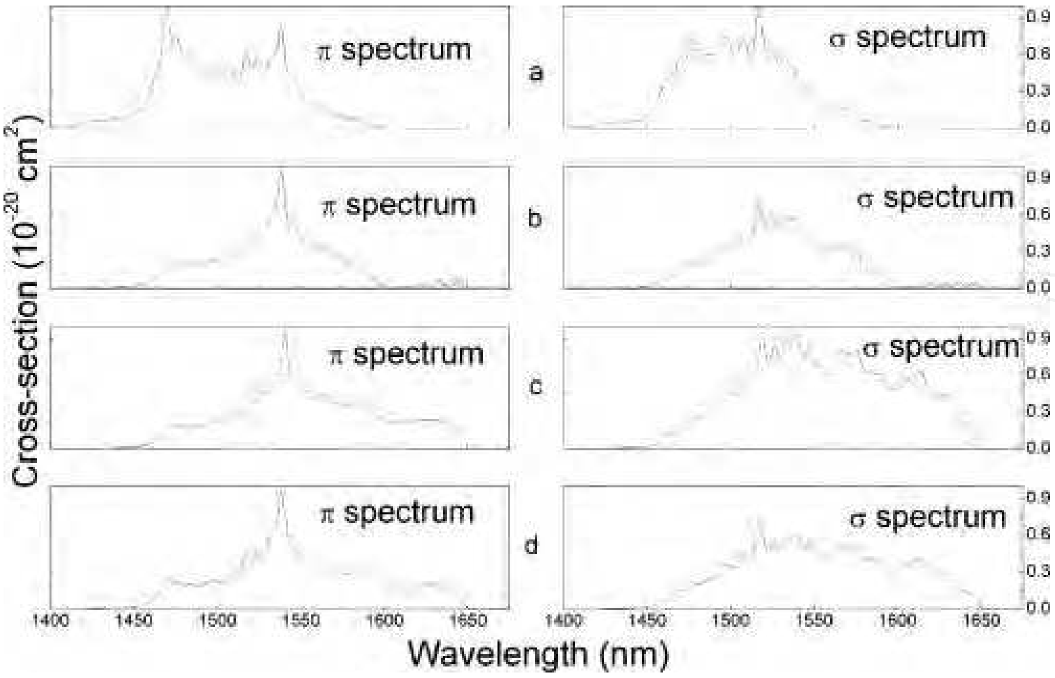

Fig. 2.12. The cross sections of the **Er^{3+}** ions in the **CBO** crystal. (a) The absorption cross-section, (b) the emission cross-section derived by the RM, (c) the emission cross-section derived by the FL, and (d) the emission cross-section derived by the modified method.

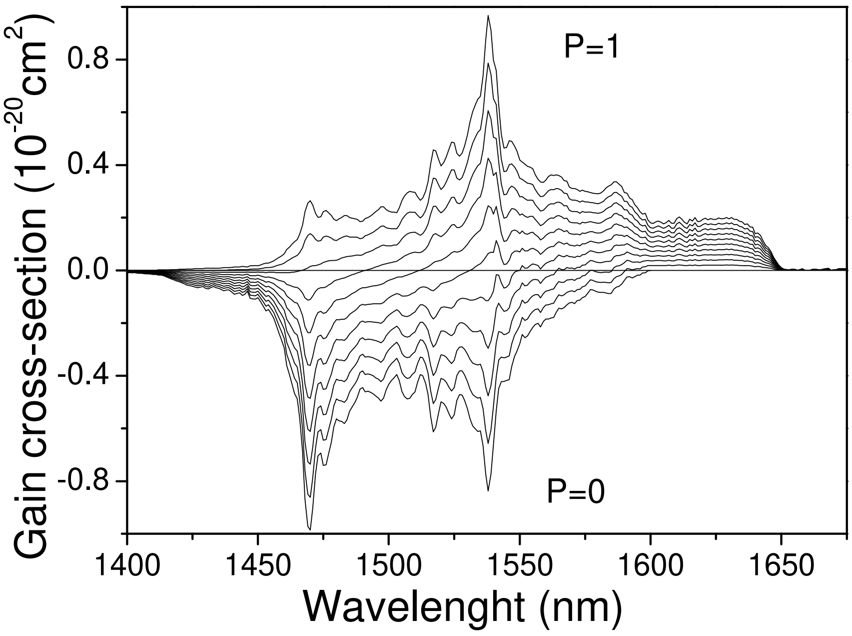

(a)

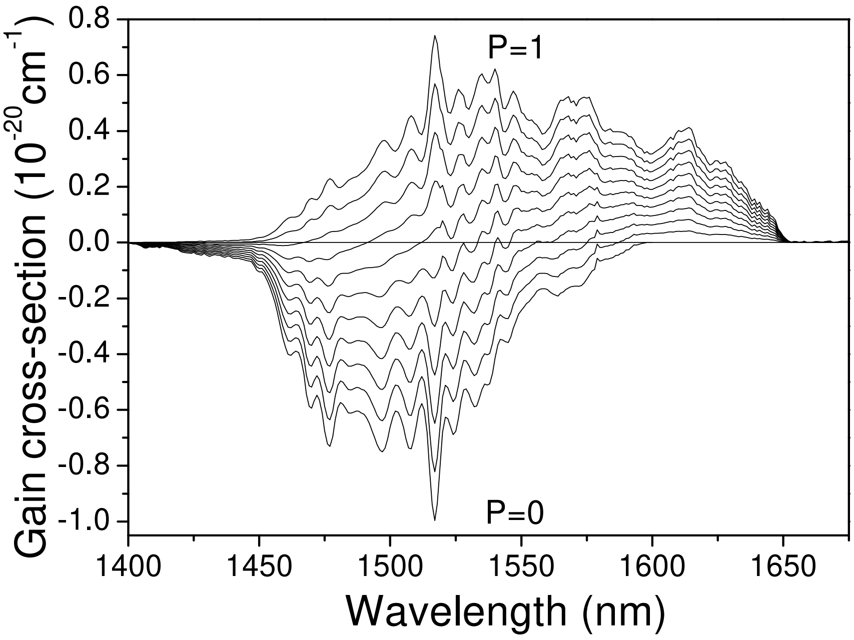

(b)

Fig. 2.13. The wavelength dependence of the gain cross-section for several values of population inversion P (P = 0,0.1,0.2,…,1) (a) for π spectrum (b) for σ spectrum

Transition (from $^4I_{15/2}$)	λ(nm)	the π -polarized f ×10⁶		the σ -polarized f ×10⁶	
		$f_{\exp}$	$f_{ed,th}$	$f_{\exp}$	$f_{ed,th}$
$^4I_{13/2}$	1517	2.73	2.46	3.33	2.98
$^4I_{11/2}$	978	0.72	0.97	1.39	1.26
$^4I_{9/2}$	793	0.56	0.70	0.75	0.82
$^4F_{9/2}$	652	3.82	4.32	5.45	5.74
$^2H_{11/2}$	523	8.73	8.95	12.92	13.07
$^4F_{7/2}$	486	4.17	4.38	5.74	5.62
$^4F_{5/2}$	450	0.91	1.09	1.35	1.33
$^2H_{9/2}$	403	1.48	1.49	1.48	1.57
$^4G_{11/2}$	380	16.36	16.12	26.50	26.12
$^4G_{9/2}$	365	3.85	4.11	3.94	4.08
$^4D_{5/2}$	257	20.37	19.93	26.71	26.45

Table 2.4. Experimental, theoretical oscillator strengths for Er^{3+} ions in CBO Crystal

Hosts	Ω_2 (10^{-20} cm²)	Ω_2 (10^{-20} cm²)	Ω_2 (10^{-20} cm²)	Ref.
$Ca3(BO_3)_2$ Ω_t^{eff}	5.35	4.95	2.29	28
YAG	0.66	0.81	0.71	31
YVO_4	13.45	2.23	1.67	32
$LiYF_4$	1.92	0.26	1.96	33
$NaBi(WO_4)_2$	5.50	1.00	0.71	34
Y_2O_3	4.59	1.21	0.48	35

Table 2.5. Comparison of Judd-Ofelt parameter Ω_2 of Er^{3+}: CBO and other Er^{3+} doped crystals

Transition	$\bar{\lambda}$ (nm)	A_{ed}	A_{md}	$\beta_{JJ'}$ (%)	τ_r (ms)
$^4I_{13/2}\rightarrow{}^4I_{15/2}$	1540	292.11	41.51	100	3.01
$^4I_{11/2}\rightarrow{}^4I_{13/2}$	2822	43.50	8.61	14.6	2.79
$^4I_{15/2}$	982	305.91		85.4	
$^4I_{9/2}\rightarrow{}^4I_{11/2}$	4490	2.37	1.35	0.5	1.46
$^4I_{13/2}$	1704	115.09		16.8	
$^4I_{15/2}$	809	556.95		82.7	
$^4F_{9/2}\rightarrow{}^4I_{9/2}$	3466	6.25	2.96	0.2	0.20
$^4I_{11/2}$	1956	151.25	6.76	3.2	
$^4I_{13/2}$	1142	221.42		4.5	
$^4I_{15/2}$	656	4529		92.1	
$^4S_{3/2}\rightarrow{}^4I_{9/2}$	1666	176.60		4.3	0.24
$^4I_{11/2}$	1215	89.39		2.2	
$^4I_{13/2}$	842	1132		27.4	
$^4I_{15/2}$	545	2736		66.2	

Table 2.6. Radiative transition probabilities $A_{JJ'}$, fluorescence branching ratios $\beta_{JJ'}$, and radiative decay time τ_r for Er^{3+} ions in CBO crystal.

2.3.3 The spectrum characteristics of Dy^{3+}:$Ca_3(BO_3)_2$ crystal

Fig.2.14 shows the room temperature absorption spectrum of Dy^{3+}:$Ca_3(BO_3)_2$ crystal, which consists of nine groups of bands.[36] They are associated with the observed transitions from the $^6H_{15/2}$ ground state. The wavelengths corresponding to the transitions are listed in Table 2-7, which also displays the integrated absorbance, the measured and calculated line strengths of Dy^{3+}: CBO crystal. The room temperature emission spectrum is presented in Fig.2.15, in which there are several bands centered at 479, 575, 663, and 750 nm corresponding to $^4F_{9/2}\rightarrow{}^6H_{15/2}$, $^6H_{13/2}$, $^6H_{11/2}$, and $^6H_{9/2}+{}^6F_{11/2}$ transitions, respectively. Fig.2.16 displays the fluorescence decay curves of $^4F_{9/2}\rightarrow{}^6H_{13/2}$ and $^4F_{9/2}\rightarrow{}^6H_{15/2}$ transitions of Dy^{3+}: CBO crystal excited at 397 nm, from which the fluorescence lifetime of the $^4F_{9/2}$ of Dy^{3+} in CBO is calculated to be about 1.275 ms. Table 2-8 presents the intensity parameters of Dy^{3+}: CBO crystal and the comparison between the intensity parameters of Dy^{3+} doped in some other laser crystals and in CBO. The spectroscopic quality factor $X=\Omega_4/\Omega_6$ for the Dy^{3+} in CBO is determined to be 2.982. This value for X suggests that Dy^{3+}: CBO is a promising material for efficient laser action when compared with Dy^{3+}: YVO_4 for which X=2.132. Table2-9 displays the experimental and calculated oscillator strengths for absorption $^6H_{15/2}$ ground state of Dy^{3+} ion in CBO crystal. Table 2-10 demonstrates the calculated radiative transition rate, the branching ratios, and the radiative lifetime for the emission from the $^4F_{9/2}$ level of Dy^{3+}: CBO. The fluorescence branching ratio is a critical laser parameter because it also characterizes the possibility of attaining stimulated emission from a specific transition. The $^4F_{9/2}\rightarrow{}^6H_{13/2}$ transition has large value of the branching ratios, thereby suggesting that this transition may result in the strongest laser action. This work gives a consistent optical characterization of Dy^{3+}: CBO crystal, which may realize a yellow solid state laser device.

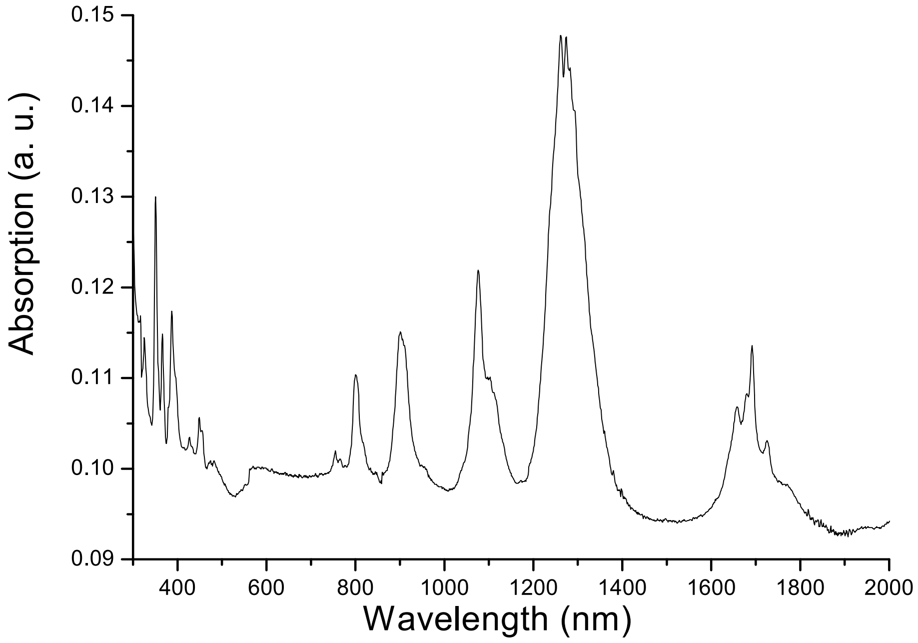

Fig. 2.14. The room temperature absorption spectrum of CBO: Dy^{3+} (sample thickness=0.306 cm).

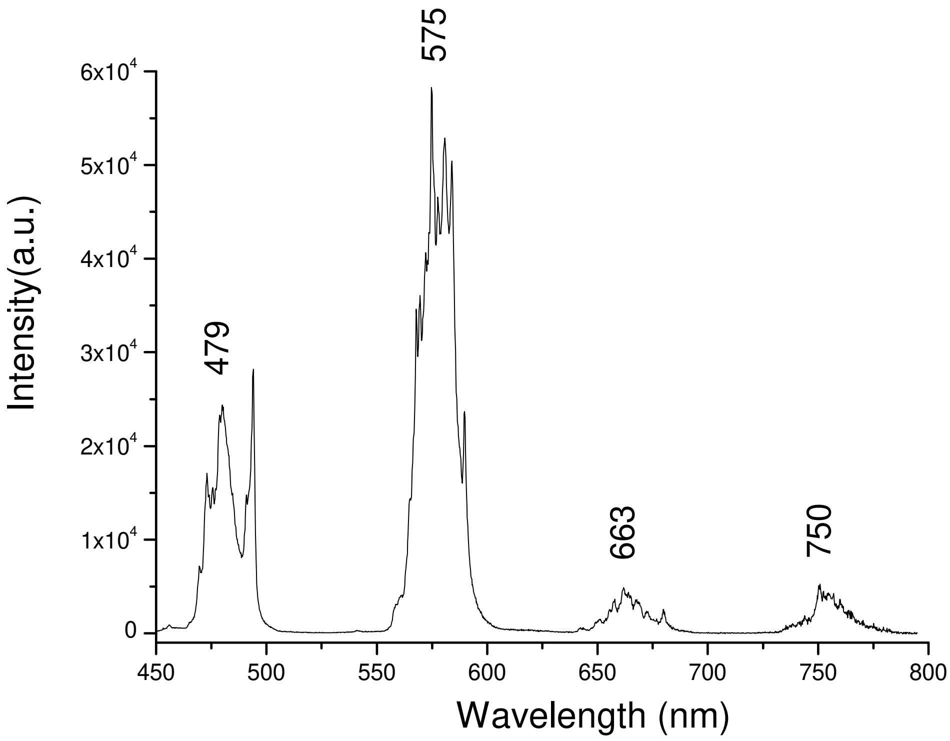

Fig. 2.15. The room temperature emission spectrum of Dy^{3+}: CBO (excited by 397 nm).

Excited state	Wavelength (nm)	Γ (nm/cm)	S_{mea} ($10^{-20}cm^2$)	S_{cal} ($10^{-20}cm^2$)
$^6H_{11/2}$	1692	2.755	0.384	0.949
$^6F_{11/2}$, $^6H_{9/2}$	1262	35.411	6.619	6.564
$^6H_{7/2}$, $^6F_{9/2}$	1076	1.823	0.399	0.026
$^6F_{7/2}$	901	3.841	1.001	0.698
$^6F_{5/2}$	800	1.244	0.364	0.218
$^4G_{11/2}$	449	0.327	0.167	0.029
$^4M_{21/2}$, $^4K_{17/2}$	386	1.511	0.891	0.070
$^4I_{11/2}$	366	0.440	0.272	0.512
$^6P_{7/2}$	351	1.291	0.830	0.978

Table 2.7. The integrated absorbance, the measured and calculated line strengths of Dy^{3+}: CBO crystal

Crystals	Ω_2	Ω_4	Ω_6	Reference
CBO	5.216	1.858	0.623	This work
$Y_3Sc_2Ga_3O_{12}$	0.134	0.7261	0.61	36
$LiYF_4$	2.01	1.34	2.39	11
YVO_4	6.59	3.71	1.74	37
$YAl_3(BO_3)_4$	10.04	2.04	2.31	38
$KY(WO_4)_2$	23.24	3.329	2.359	1

Table 2.8. Comparison between the intensity parameters of Dy^{3+} doped in some laser crystals and in CBO (Ω_t are in units of 10^{-20} cm^2)

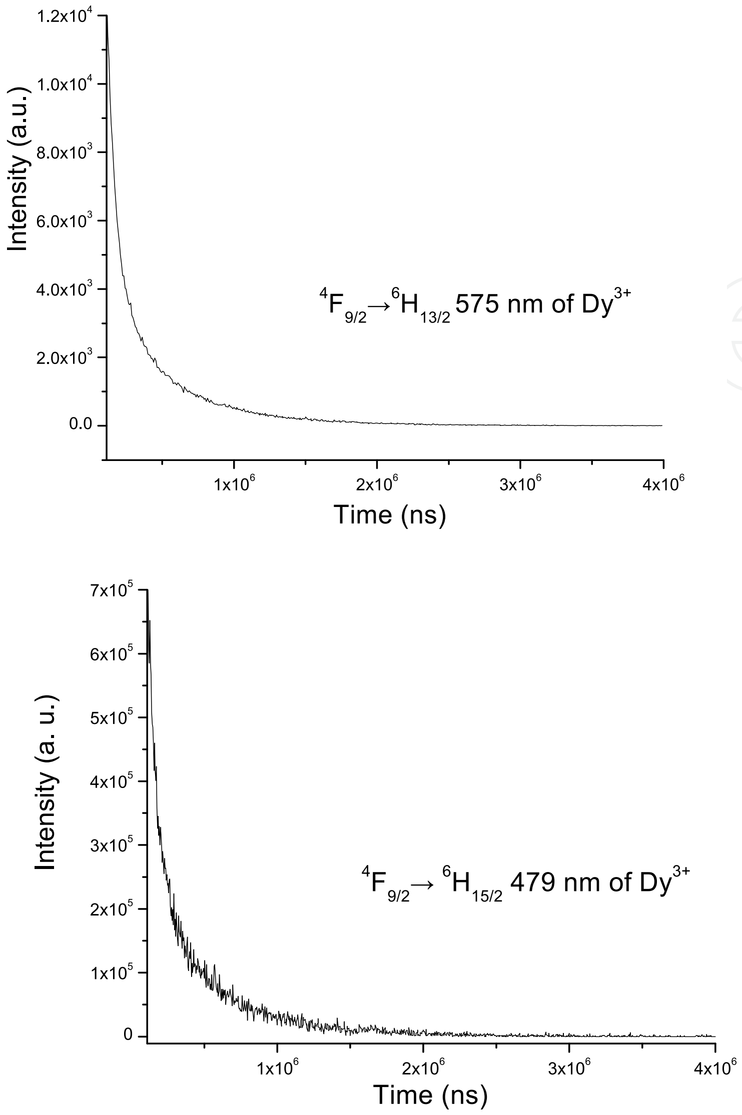

Fig. 2.16. The fluorescence decay curves of ${}^4F_{9/2}\rightarrow{}^6H_{13/2}$ and ${}^4F_{9/2}\rightarrow{}^6H_{15/2}$ transitions of Dy^{3+}: CBO crystal (by 397 nm excited)

Upper state	f_{exp}	f_{cal}	Δf
${}^6H_{11/2}$	0.243	0.601	0.358
${}^6F_{11/2}$, ${}^6H_{9/2}$	5.633	5.586	−0.047
${}^6H_{7/2}$, ${}^6F_{9/2}$	0.398	0.026	−0.372
${}^6F_{7/2}$	1.096	0.834	−0.262
${}^6F_{5/2}$	0.491	0.290	−0.201
${}^4G_{11/2}$	0.410	0.072	−0.338
${}^4M_{21/2}$, ${}^4K_{17/2}$	2.563	0.202	−2.361
${}^4I_{11/2}$	0.830	0.016	−0.814
${}^6P_{7/2}$	2.648	3.120	0.472

Table 2.9. The experimental and calculated oscillator strength f (×10^6) for absorption ${}^6H_{15/2}$ ground state of Dy^{3+} ion in CBO crystal. Also the Δf (×10^6) between the calculated and experimental oscillator (note: rms f=0.883×10^{-6})

Start levels	Wavelength (nm)	A (s^{-1})	β (A)	τ (μs)
$^6H_{15/2}$	479	90.209	0.115	1275
$^6H_{13/2}$	575	612.77	0.781	
$^6H_{11/2}$	663	66.561	0.085	
$^6H_{9/2}+^6F_{11/2}$	750	15.066	0.019	

Table 2.10. The calculated radiative transition rate, the branching ratios, and the radiative lifetime for the emission from the $^4F_{9/2}$ level of Dy^{3+}: CBO

3. Rare earth-doped $Ca_3Re_2(BO_3)_4$ [Re=Y,Gd] crystals

3.1 The crystal structure

An ORTEP drawing of the structure fragment of crystal Yb:$Ca_3Y_2(BO_3)_4$ is shown in Fig.3.1a. Fig.3.1b shows the packing diagram of cell units of Yb:$Ca_3Y_2(BO_3)_4$ crystal.[6] In Yb^{3+}:$Ca_3Y_2(BO_3)_4$ crystal structure, cations occupy three independent sites statistically, which is similar to $Ca_3La_2(BO_3)_4$[39] and $Ba_3La_2(BO_3)_4$[40]. The basic structure of Yb:$Ca_3Y_2(BO_3)_4$ is composed of three sets of M-oxygen distorted polyhedrons, and three sets of BO_3 planar triangles. Ca^{2+} and Y^{3+} ions occupy three independent sites statistically. M1、M2 and M3 were suggested to stand for these three independent sites respectively. They are coordinated by eight oxygen ions to form the distorted polyhedron. From the value of the electronic density of each independent site, and the ion charges of Ca^{2+} and Y^{3+} ions as well as the ratio of their atomic number in the formula, we can calculate their ratio in each site. Concretely, the method for calculating the ratio of Yb/Ca is as follows: we suggest the average atomic number of M_n atom:

$$\overline{Z}_n = Z_Y X_n + Z_{Ca} Y_n \tag{3.1}$$

Here the atomic number of Y and Ca are: $Z_Y = 39, Z_{Ca} = 20$, and X_n is the occupancies of Y^{3+} ion in M_n, Y_n is the occupancies of Ca^{2+} ion M_n,

$$X_n + Y_n = 1 \tag{3.2}$$

As we know:

$$\frac{\overline{Z_n}}{\overline{Z_{n+1}}} = \frac{\rho_n}{\rho_{n+1}} \tag{3.3}$$

in which ρ is the electronic density of M_n. According the formula $Ca_3Y_2(BO_3)_4$, we can get:

$$X_1 + X_2 + X_3 = 2 \tag{3.4}$$

$$Y_1 + Y_2 + Y_3 = 3 \tag{3.5}$$

Combing all the above equations, we can calculate the ratio of Y/Ca in the three sites M1, M2 and M3,the results are as follows: M1=0.61Y+0.39Ca, M2=0.445Y+0.555Ca and M3=0.25Y+0.75Ca.Yb^{3+} ions substitute Y^{3+} ions entering these three lattices. The fact that the statistical distribution of Ca^{2+}, $Y^{3+}$and Yb^{3+} ions might lead to the increase of width of spectra of this crystal. As a matter of fact, this was confirmed by the next part of this report. Table 3-1 presents the atomic coordinates and thermal parameters.

	x	y	z	Wyckoff	U(eq)
M(1)	1750(3)	2500	9687(2)	4c	20(1)
M(2)	-193(2)	4164(1)	6788(2)	8d	30(1)
M(3)	-1999(3)	3738(1)	11589(2)	8d	32(1)
O(1)	4458(11)	3275(5)	10709(10)	8d	40(20)
O(2)	1200(20)	2500	12380(17)	4c	40(30)
O(3)	-1536(18)	2500	9990(14)	4c	40(30)
O(4)	1971(15)	4849(7)	5098(18)	8d	40(40)
O(5)	-970(20)	5456(9)	8143(15)	8d	40(50)
O(6)	-2537(18)	3256(8)	7768(15)	8d	40(30)
O(7)	1120(30)	3993(9)	9410(20)	8d	40(80)
B(1)	5110(30)	2500	11350(20)	4c	18(4)
B(2)	2790(20)	2500	6470(20)	4c	13(3)
B(3)	3267(19)	5404(9)	5432(15)	8d	21(3)

U(eq) is defined as one third of the trace of the orthogonalized Uij tensor. The Ca^{2+} and Y^{3+} ions coexist in M1, M2 and M3 positions statistically.

Table 3.1. Atomic coordinates (× 10^4) and thermal parameters ($Å^2 \times 10^3$)

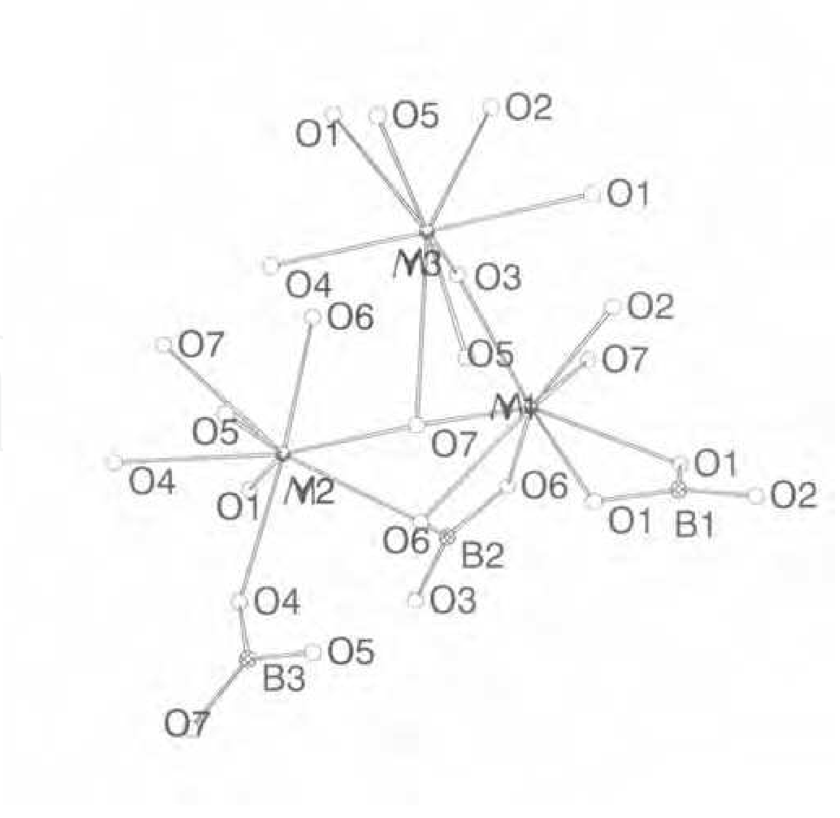

Fig. 3.1a. A structure fragment of crystal Yb:$Ca_3Y_2(BO_3)_4$

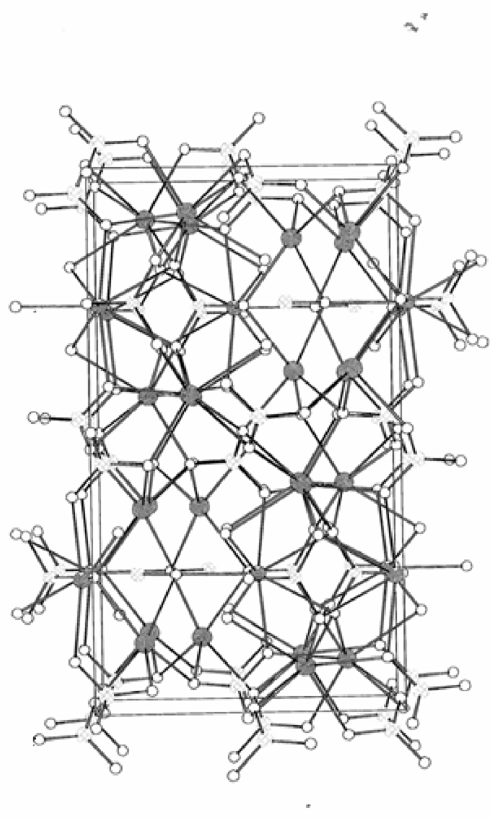

Fig. 3.1b. Packing diagram of cell units of Yb:$Ca_3Y_2(BO_3)_4$

3.2 The crystal growth

The crystal was grown by Czochralski method. The crystal growth was carried out in a DGL-400 furnace with KGPF25-0.3-2.5 power supply of intermediate frequency. An Ir-crucible of 60mm diameter by 35 mm high was used.

The initial compounds for the synthesis were AR grade $CaCO_3$, H_3BO_3 and 4N Y_2O_3,Yb_2O_3. A $Ca_3Y_2(BO_3)_4$ compound with 5mol%Yb_2O_3-doped was synthesized according to the following reactions:

$$6CaCO_3+0.05Yb_2O_3+1.95Y_2O_3+8H_3BO_3\rightarrow 2Ca_3Yb_{0.05}Y_{1.95}(BO_3)_4+6CO_2\uparrow+12H_2O\uparrow$$

Thoroughly mixed and pressed mixtures of the stoichiometric composition were slowly heated to 500^0C at a rate of 50^0C/h and further to the synthesis temperature at the rate of 150^0C/h in a Pt-crucible. Then the sintered compound was melt in the Ir-crucible under N_2 atmosphere, at a temperature which was 50^0C higher than the crystallization temperature, and was kept at this temperature for one hour. Seeding was performed on the Ir-wire. The nitrogen gas pressure is 0.04MPa. Pulling rate and the rotation rate was 1.3~1.5mm/h and 12-20 r.p.m, respectively. When the growth process was ended, the crystal was drawn out of the melt surface and cooled down to room temperature at a rate of $10\sim30^0$C/h. The transparent single crystals with a size up to φ20 mm×55 mm was obtained (as shown in Fig.3.2). Fig.3.3 shows the interference fringe of the grown Yb^{3+}:$Ca_3Y_2(BO_3)_4$ crystal, the optical homogeneity is 4×10^{-5}, it means the crystal has excellent quality. Table 3-2 presents the parameters of crystal growth. In order to estimate the solubility of the doping ion in the crystal, it is customary to use an "effective segregation coefficient" defined as [41]: $k_e=C_s/C_l$, C_s is the doped-ion concentration in the crystal and C_l is the doped-ion concentration in the melt, since the concentration of Yb^{3+} ion in Yb^{3+}:CYB was measured to be 1.56wt% by electron probe microanalysis method ,the effective segregation coefficient of Yb^{3+} ion in CYB crystal was calculated to be 0.97.

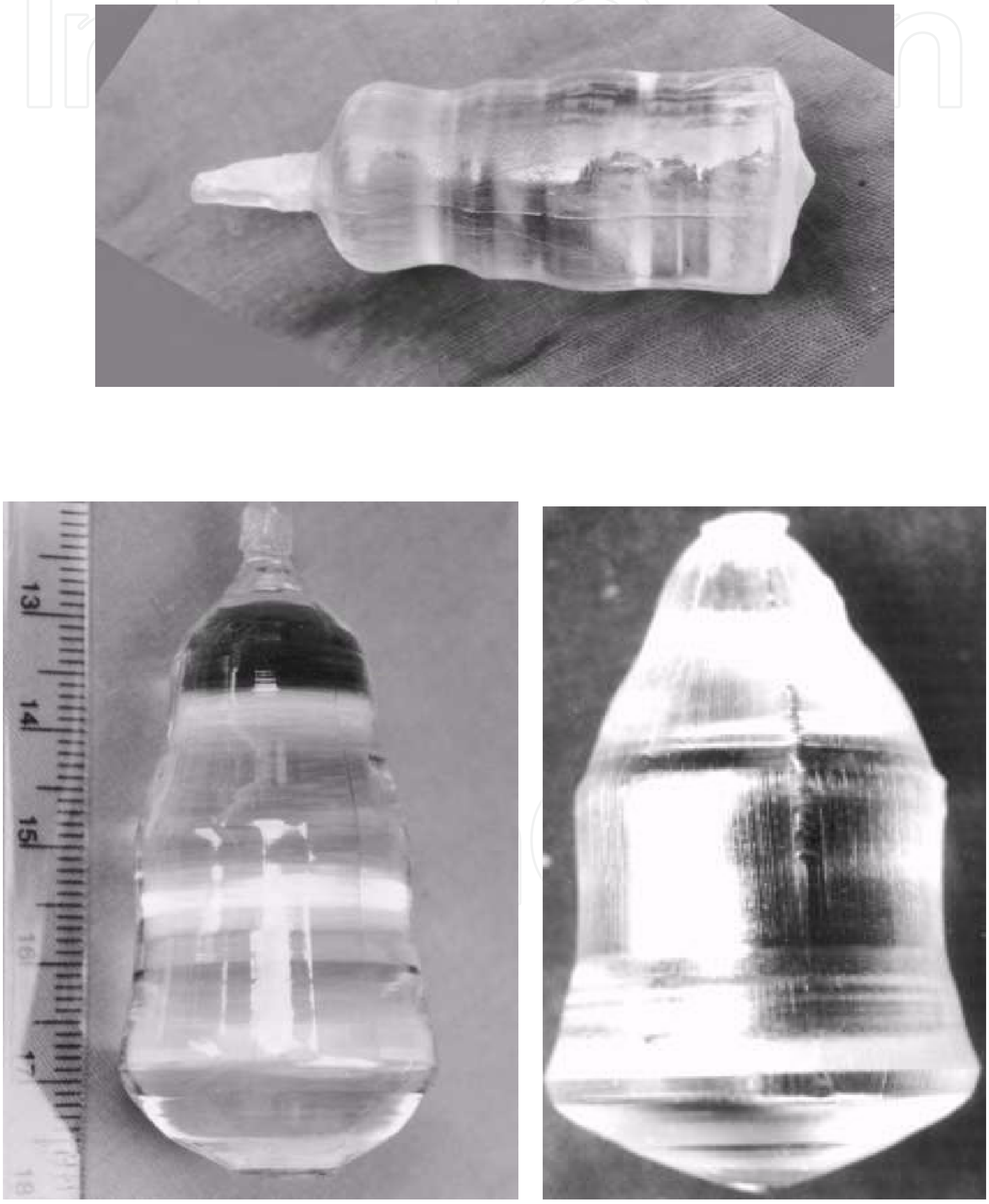

Fig. 3.2. The grown $Yb^{3+}:Ca_3Y_2(BO_3)_4$ crystal

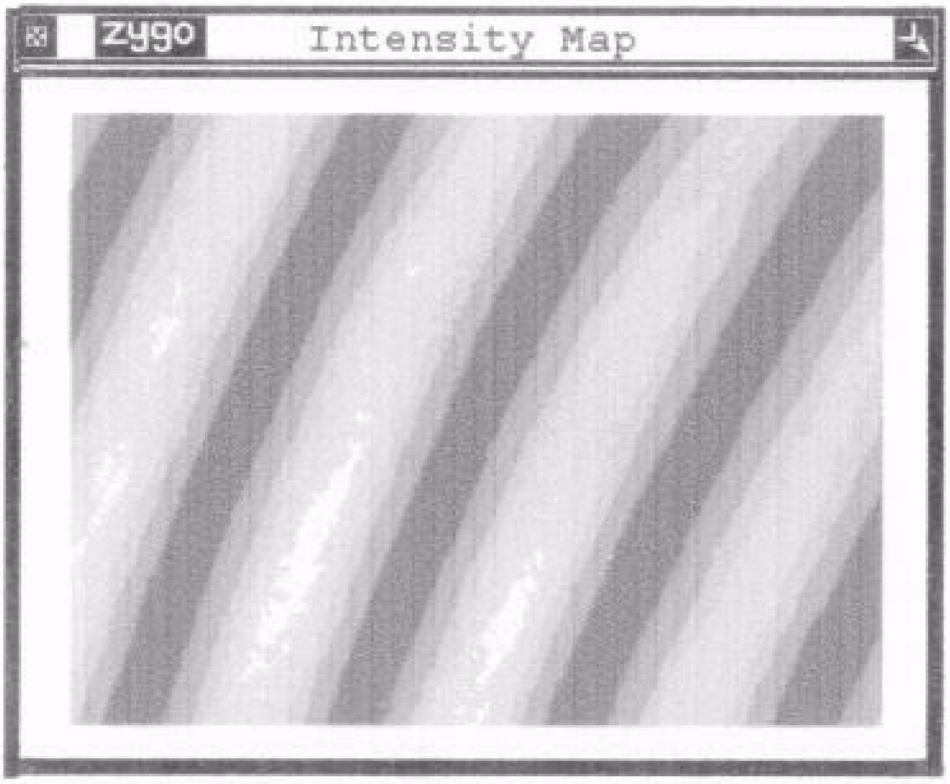

Fig. 3.3. Interference fringe of Yb^{3+}:$Ca_3Y_2(BO_3)_4$ crystal.

Nitrogen gas (MPa)	0.04	Rotate rate(rpm)	12-20
Soaping temp. (^{0}C)	1460	Decreasing rate of temp.(^{0}C/day)	2~10
Soaping time (h)	0.5	Pulling rate(mm/h)	1.3~1.5
Crucible size(mm)	φ60mm×35mm	Annealing rate(^{0}C/h)	10~50
Seeding temp. (^{0}C)	1410	Crystal size(mm)	φ20 mm×55 mm

Table 3.2. The parameters of crystal growth.

3.3 The spectrum characteristics

3.3.1 The spectrum characteristics of Tm^{3+}:$Ca_3Y_2(BO_3)_4$ crystal

Fig.3.4 presents the absorption spectrum of $Ca_3Y_2(BO_3)_4$:Tm^{3+}crystal, in which there are seven peaks centered at 1684nm, 1215 nm, 792.4 nm, 687.9nm, 475.6 nm, 359.9 nm, 262.9nm, corresponding to the transitions from $^3H_6$ to$^3F_4$, $^3H_5$, $^3H_4$, $^3F_3$, $^1G_4$, $^1D_2$, $^1I_6$, respectively[42]. The FWHM at 792.4 nm is about 33.9 nm and the cross-section is about 1.5×10^{-21} cm^2, which is benefit to the pumping of commercial laser diode. The room temperature emission spectrum of $Ca_3Y_2(BO_3)_4$:Tm^{3+} crystal excited at 792.4 nm is presented in Fig.3.5, in which there is a broad emission band ranged from 1332.6 nm to 1429.1 nm. The FWHM of this emission band is 63.6 nm, which is resulted from the statistical distribution of Ca^{2+}, $Y^{3+}$and Tm^{3+} ions.

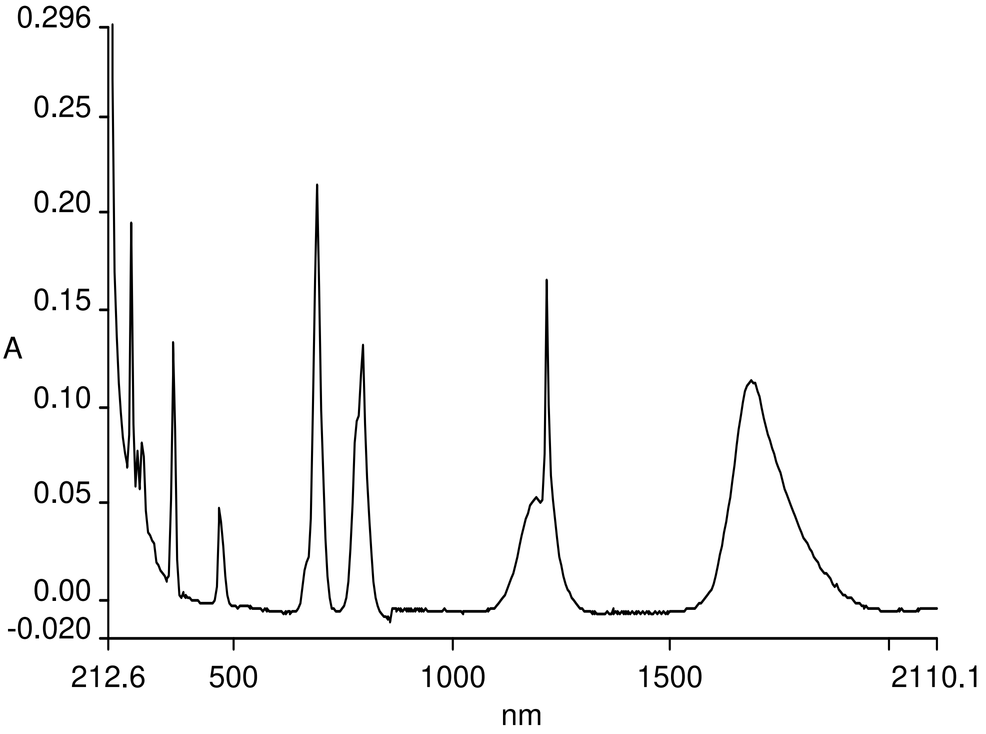

Fig. 3.4. The absorption spectrum of $Ca_3Y_2(BO_3)_4$:Tm^{3+}crystal

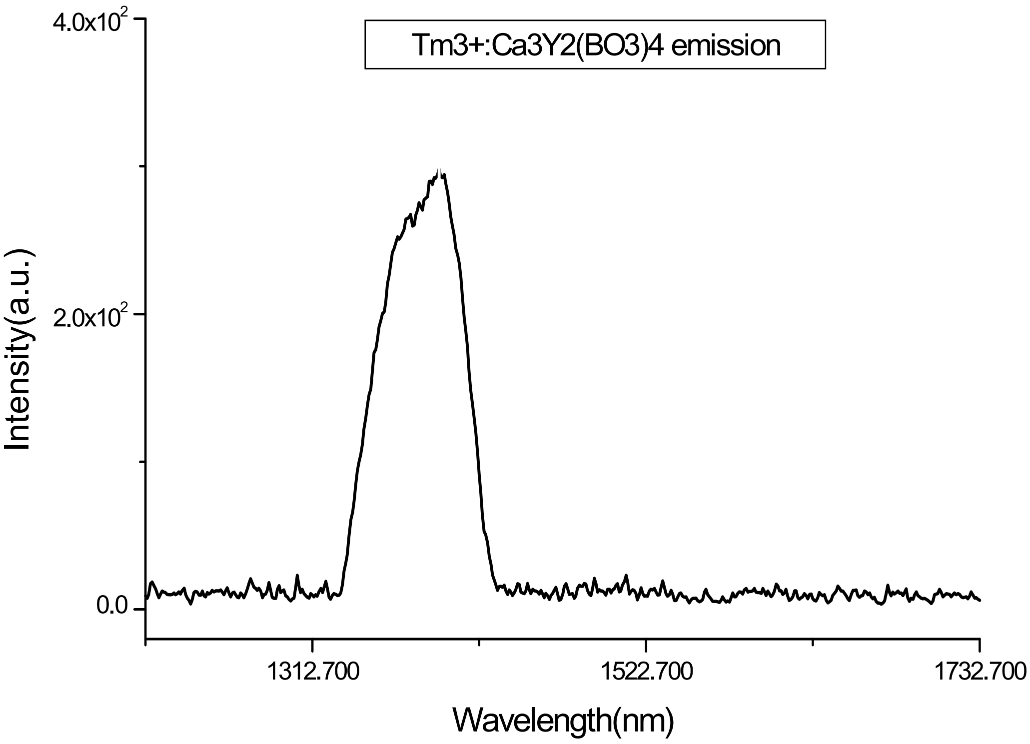

Fig. 3.5. The room temperature emission spectrum of $Ca_3Y_2(BO_3)_4$:Tm^{3+} crystal excited at 792nm

3.3.2 The spectrum characteristic of Er^{3+}:$Ca_3Y_2(BO_3)_4$ crystal

Fig.3.6 presents the absorption spectrum of $Ca_3Y_2(BO_3)_4$:Er^{3+}crystal, in which there are twelve peaks centered at 244.6 nm, 257.3 nm, 366.4 nm, 379.9 nm, 408.1 nm, 452 nm, 522.7 nm, 544.2 nm, 654.3 nm,799.3 nm,976.6 nm,1518.4nm, corresponding to the transitions from $^4I_{15/2}$ *to* $^2I_{11/2}$, $^4D_{5/2}$+$^4D_{7/2}$, $^4G_{9/2}$, $^2G_{9/2}$+$^4F_{9/2}$+$^2H_{9/2}$, $^4F_{5/2}$, $^2H_{11/2}$, $^4S_{3/2}$, $^4F_{9/2}$, $^4I_{9/2}$, $^4I_{13/2}$, respectively[43]. The room temperature emission spectrum of $Ca_3Y_2(BO_3)_4$:Er^{3+} crystal excited at 530 nm is presented in Fig.3.7, in which there is a broad emission band ranged from 1429.4 nm to 1662.8 nm. The FWHM of this emission band is 126 nm. The factor contributing to this broad emission is the disordered structure of the crystal, namely, Ca^{2+} and Y^{3+} ions are statistically situated in three different lattices in the crystal structure determined by us. This broad emission will benefit the energy storage. Therefore, this crystal should be useful as a tunable infrared (in the eye-safe region at 1.54 μm) laser crystal.

Based on the measured absorption spectra of three commutative perpendicularity directions and J-O theory, the J-O parameters are calculated to be Ω_2=1.214×10^{-20} cm^2, Ω_4=1.585×10^{-20} cm^2, Ω_6=1.837×10^{-20} cm^2. The oscillator strength, radiative transition probability A, radiative lifetime τ_{rad} and the fluorescent branching ratio β are also calculated, which are shown in Table 3-3~4. The stimulated emission cross-section at *1535nm* is 6.4×10^{-21} cm^2 and the integral cross-section at 1535 nm is 2.7×10^{-18} cm^2. The lifetime measured is about *792μs* with the luminescent quantum efficiency of *20.8%*.

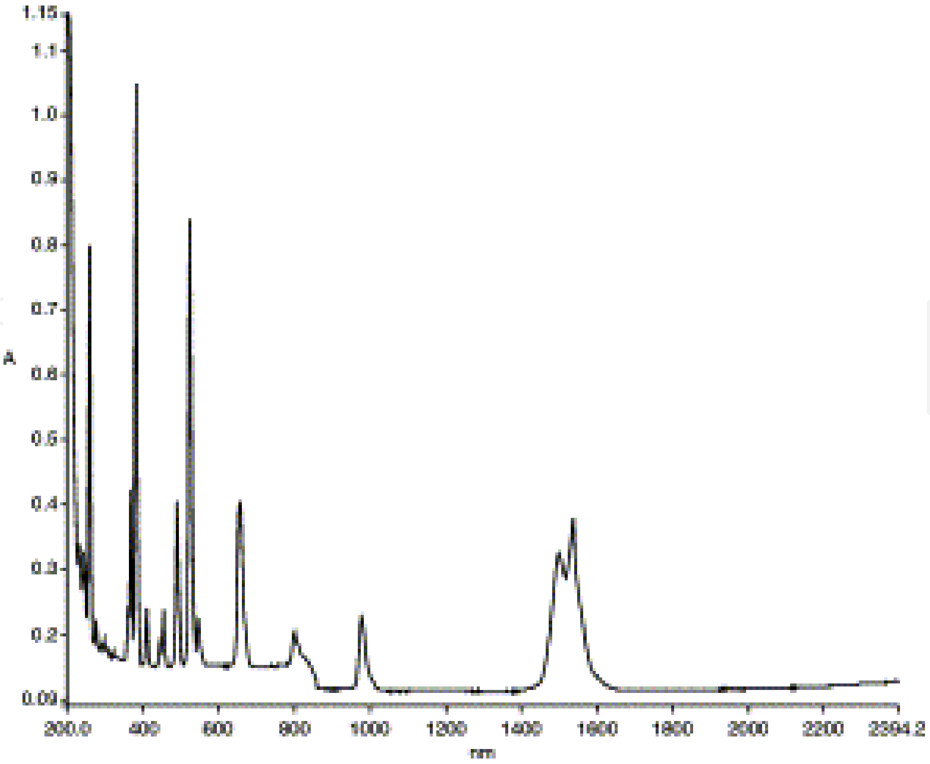

Fig. 3.6. The absorption spectrum of $Ca_3Y_2(BO_3)_4$:Er^{3+}crystal

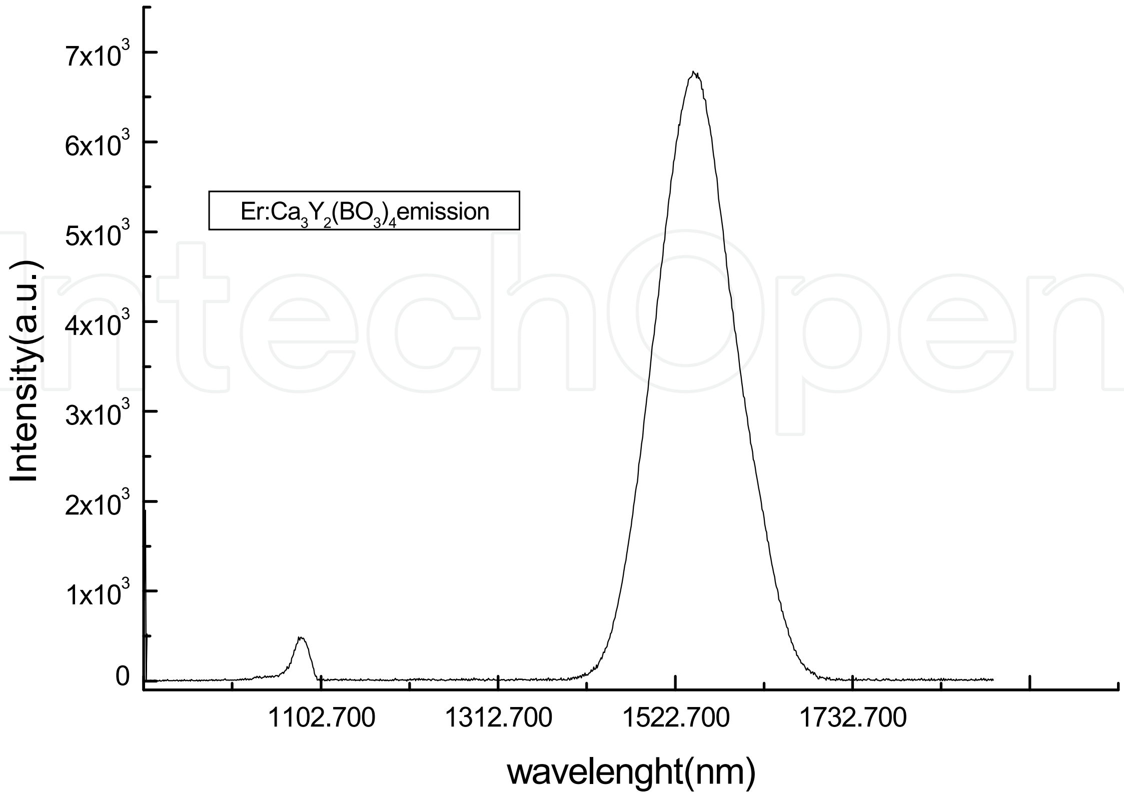

Fig. 3.7. The room temperature emission spectrum of $Ca_3Y_2(BO_3)_4$:Er^{3+} crystal excited at 530 nm

Wavelength λ(nm)	$f_{exp}\times10^6$	$f_{cal}\times10^6$
258	14.380	0.213
368	3.276	6.595
381	11.034	0.018
453	1.261	1.015
491	1.895	3.161
524	6.618	3.614
654	2.926	2.910
800	0.681	0.411
974	0.728	0.876
1534	2.219	2.076
$rms\Delta f=5.864\times10^{-6}$		

Table 3.3. Oscillator strengths of 7 at% Er^{3+} in $Ca_3Y_2(BO_3)_4$ crystal

Transtion $J \rightarrow J'$	λ(nm)	$A^{ed}(s^{-1})$	$A^{md}(s^{-1})$	$A^{total}(s^{-1})$	β	τ_{rad}(ms)
$^4I_{13/2} \rightarrow {}^4I_{15/2}$	1535	216.5	46.2	262.7	1	3.807
$^4I_{11/2} \rightarrow {}^4I_{13/2}$	2822	27.489	9.507	362.52	0.102	2.758
$^4I_{15/2}$	976	325.526			0.898	
$^4I_{9/2} \rightarrow {}^4I_{13/2}$	1694	85.45		401.96	0.213	2.488
$^4I_{15/2}$	800	316.512			0.787	
$^4F_{9/2} \rightarrow {}^4I_{9/2}$	3554	3.436	3.03	2519.73	0.003	0.397
$^4I_{11/2}$	1933	126.801	7.718		0.053	
$^4I_{13/2}$	1147	84.96			0.034	
$^4I_{15/2}$	653	2293			0.91	
$^4S_{3/2} \rightarrow {}^4I_{9/2}$	1693	98.665		3366	0.029	0.297
$^4I_{11/2}$	1210	73.585			0.022	
$^4I_{13/2}$	847	921.885			0.274	
$^4I_{15/2}$	545	2272			0.675	
$^2H_{9/2} \rightarrow {}^4F_{9/2}$	1063	53.286	51.595	5412	0.019	0.185
$^4I_{9/2}$	818	27.509	1.162		0.005	
$^4I_{11/2}$	686	674.786	42.768		0.133	
$^4I_{13/2}$	552	2483			0.459	
$^4I_{15/2}$	405	2078			0.384	
$^4G_{11/2} \rightarrow {}^2H_{11/2}$	1369	42.342	14.366	24416.8	0.002	0.041
$^4F_{9/2}$	894	801.92	3.505		0.022	
$^4I_{9/2}$	714	300.563	0.851		0.009	
$^4I_{11/2}$	611	695.246	0.106		0.019	
$^4I_{13/2}$	502	2720	49.515		0.077	
$^4I_{15/2}$	380	19786			0.81	

Table 3.4. Radiative transition probability A, radiative lifetime τ_{rad} and fluorescent branching ratio β of Er^{3+} in 7 at%Er^{3+}:$Ca_3Y_2(BO_3)_4$ crystal at room temperature.

3.3.3 The spectrum characteristic of Yb^{3+}:$Ca_3Y_2(BO_3)_4$ crystal

Fig.3.8 presents the absorption spectrum of $Ca_3Y_2(BO_3)_4$:Yb^{3+}crystal, in which there is a broad absorption band ranged from 850 nm to 1000 nm, corresponding to the transition from $^2F_{7/2} \rightarrow {}^2F_{5/2}$. [6] The FWHM at 977 nm is about 12 nm and the cross-section is about $1.9\times10^{-20}cm^2$, which is benefit to the pumping of commercial laser diode. Table.3-5 shows the absorption properties of some ytterbium-doped compounds. The room temperature emission spectrum of $Ca_3Y_2(BO_3)_4$:Yb^{3+} crystal excited at 977 nm is presented in Fig.3.9, in which there is a broad emission band ranged from 927.95 nm to 1102.7 nm. The FWHM of this emission band is 98 nm and its peak value is located at 1025 nm, which is resulted from the statistical distribution of Ca^{2+}, $Y^{3+}$and Yb^{3+} ions.

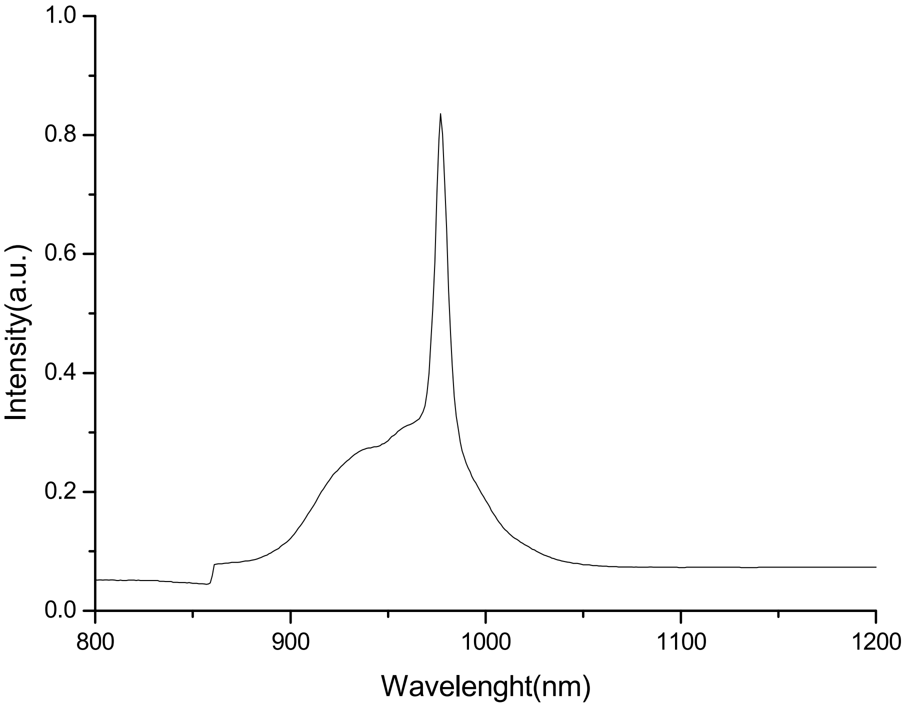

Fig. 3.8. The Absorption spectrum of Yb^{3+} $Ca_3Y_2(BO_3)_4$ crystal at room temperature

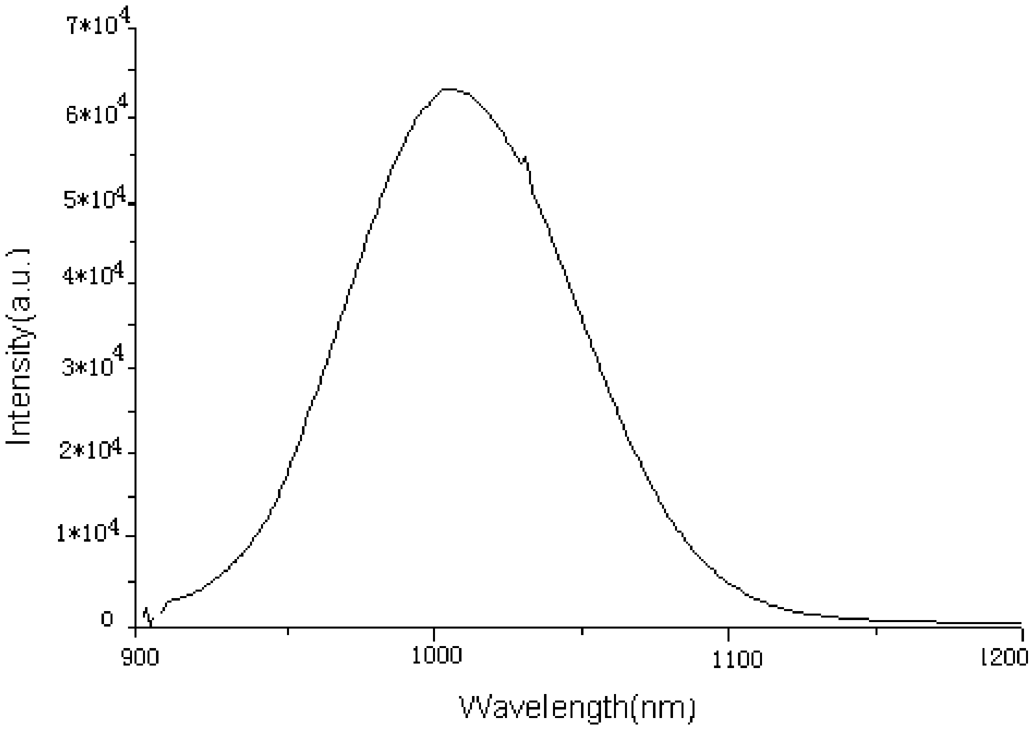

Fig. 3.9. The room temperature emission spectrum of $Ca_3Y_2(BO_3)_4:Yb^{3+}$ crystal excited at 977 nm

Compound	λ_p(nm)	σ_a ($\times 10^{-20}$ cm^2)	FWHM(nm)	References
5at%Yb:CYB	977	1.9	12	[6]
2at%Yb:YCOB	976.1	0.94	3	[44]
1at%Yb:Y_2SiO_5	977.4	2.1	7	[45]
1at%Yb:Sc_2SiO_5	979.5	1.9	4	[45]
Yb:GdCOB	976	0.87	2.6	[46]
15%Yb:YAG	968	0.94	2.6	[47]
15%Yb:BLuB	966	0.29	6.4	[47]
Yb:YAB	975	3.4	3	[48]

Table 3.5. Absorption properties of the ytterbium-doped compounds

3.3.4 The spectrum characteristic of $Nd^{3+}:Ca_3Gd_2(BO_3)_4$ crystal

Based on the absorption spectra of $Nd^{3+}:Ca_3Gd_2(BO_3)_4$ crystal and the measured absorption spectra in three commutative perpendicularity directions and J-O theory, the J-O parameters are calculated to be $\Omega_2= 2.076\times10^{-20}$ cm^2, $\Omega_4=4.252\times10^{-20}$ cm^2, $\Omega_6=5.342\times10^{-20}$ cm^2 [55]. The emission spectra of $Nd^{3+}:Ca_3Gd_2(BO_3)_4$ crystal demonstrates that there are three main emission peaks under excited of 808nm, centered at 912nm, 1064nm and 1337nm, respectively. The stimulated emission cross-section at 1064 nm corresponding to $^4F_{3/2} \rightarrow {}^4I_{11/2}$ transition is 2.28×10^{-20} cm^2. The fluorescence decay curve displays that the measured lifetime of $^4F_{3/2}$ level is 175 μs, and the quantum efficiency is estimated to be 72%.

3.3.5 The spectrum characteristic of $Er^{3+}:Ca_3Gd_2(BO_3)_4$ crystal

Fig.3.10 presents the absorption spectrum of $Ca_3Gd_2(BO_3)_4:Er^{3+}$crystal, in which there are twelve peaks centered at 244.6nm, 257.3 nm, 366.4 nm, 379.9nm, 408.1 nm, 452 nm, 522.7nm, 544.2 nm, 654.3 nm, 799.3 nm, 976.6 nm, 1518.4nm, corresponding to the transitions from $^4I_{15/2}$ to $^2I_{11/2}$, $^4D_{5/2}+{}^4D_{7/2}$, $^4G_{9/2}$, $^2G_{9/2}+{}^4F_{9/2}+{}^2H_{9/2}$, $^4F_{5/2}$, $^2H_{11/2}$, $^4S_{3/2}$, $^4F_{9/2}$, $^4I_{9/2}$, $^4I_{13/2}$, respectively[56]. The room temperature emission spectrum of $Ca_3Gd_2(BO_3)_4:Er^{3+}$ crystal excited at 530nm is presented in Fig.3.11, in which there is a broad emission band ranged from 1460 nm to 1600 nm. The FWHM of this emission band is 126 nm, which is resulted from the statistical distribution of Ca^{2+}, $Gd^{3+}$and Er^{3+} ions. Based on the measured absorption spectra of three commutative perpendicularity directions and J-O theory, the J-O parameters are calculated to be $\Omega_2= 4.01\times10^{-20}cm^2$, $\Omega_4=0.98\times10^{-20}cm^2$, $\Omega_6=1.72\times10^{-19}cm^2$. Comparing the parameters with those of the other Er^{3+} doped crystal, we found that the parameters are larger. The oscillator strength, radiative transition probability A, radiative lifetime τ_{rad} and the fluorescent branching ratio β are also calculated, which are shown in Tables 3-6~3-8. The stimulated emission cross-section at 1535nm is calculated to be 6.0×10^{-21}cm^2. Fig.3.12 shows the fluorescence lifetime of Er:CGB crystal under the excitation of 530 nm. The lifetime measured is about 792μs, so the luminescent quantum efficiency of the $^4I_{13/2}$ manifold is estimated to be 20%.

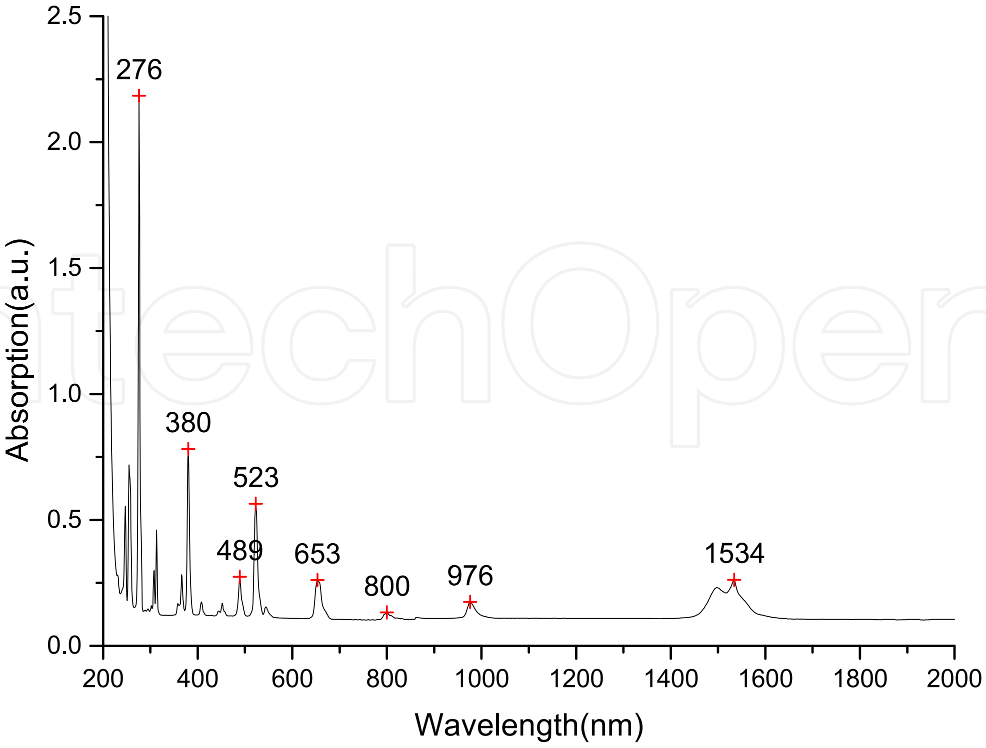

Fig. 3.10. Absorption spectrum of Er:CGB crystal in random direction at RT

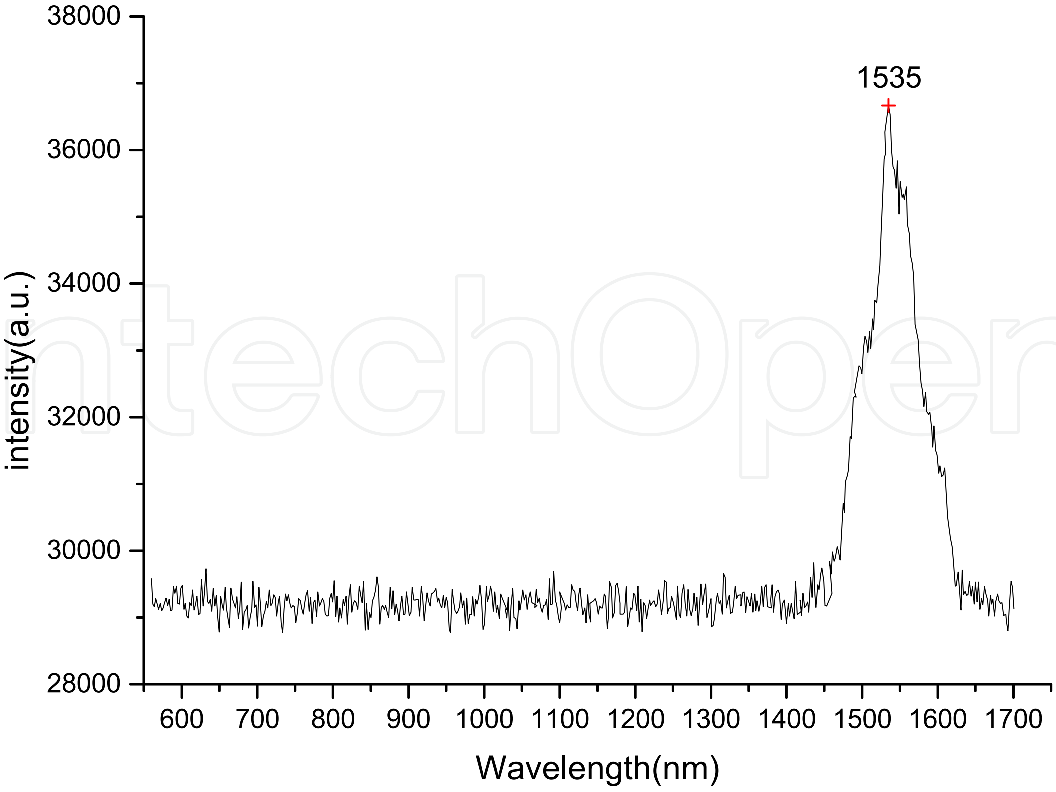

Fig. 3.11. The fluorescence spectrum of Er^{3+}:CGB under the excitation of 530nm

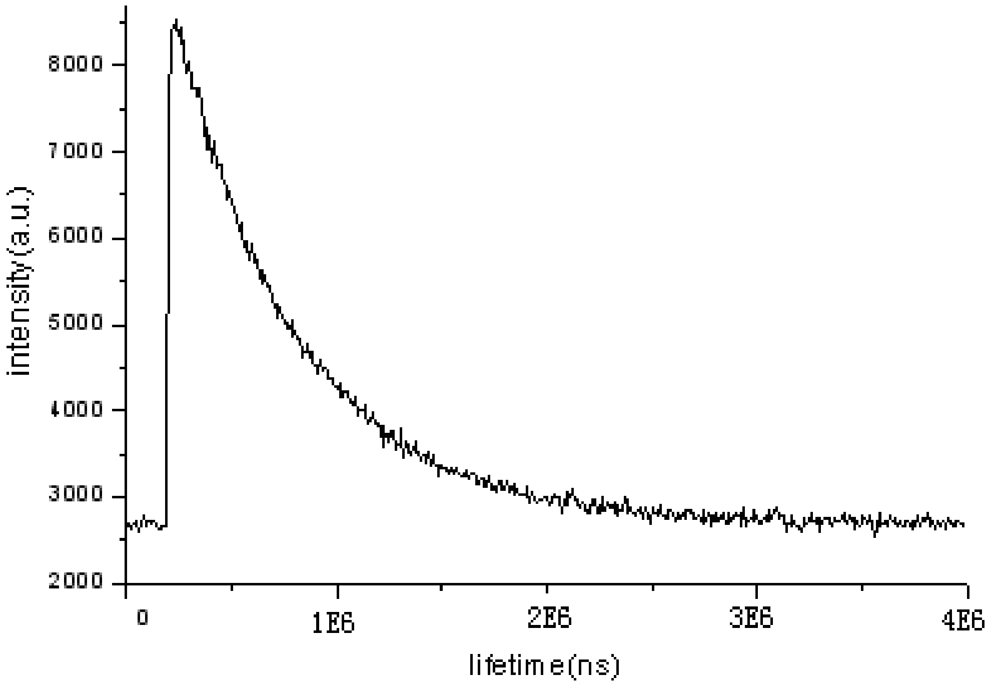

Fig. 3.12. The fluorescence lifetime of Er:CGB crystal under the excitation of 530nm

Wavelength (nm)	$f_{\text{exp}}\times10^6$	$f_{\text{cal}}\times10^6$
380	13.969	12.976
489	2.343	2.797
523	6.415	7.33
653	2.3	2.261
800	0.241	0.261
976	0.587	0.91
1534	2.053	1.938 ed(a) 0.54 md(a)
	rmsΔf =5.54×10^{-7}	

(a): ed and md denote electric-dipole and magnetic-dipole transitions respectively.

Table 3.6. Oscillator strengths of Er^{3+} in $Ca_3Gd_2(BO_3)_4$ crystal

Crystals	$\Omega_2\times10^{20}$ cm^2	$\Omega_4\times10^{20}$ cm^2	$\Omega_6\times10^{20}$ cm^2	References
Er^{3+}:$Ca_3Gd_2(BO_3)_4$	4.01	0.98	1.72	[55]
Er^{3+}:YAG	0.19	1.68	0.62	[57]
Er^{3+}:$YAlO_3$	1.06	2.63	0.78	[58]
Er^{3+}:YVO_4	1.25	1.69	0.61	[59]
Er^{3+}:$YLiF_4$	0.97	1.21	1.37	[60]

Table 3.7. The Judd-Ofelt parameters for $Ca_3Gd_2(BO_3)_4$: Er^{3+} compared with other Er-doped crystals

Transition J→J'	λ(nm)	$A^{ed}(s^{-1})$	$A^{md}(s^{-1})$	$A^{total}(s^{-1})$	β	τ_{rad}(ms)
$^4I_{13/2}\rightarrow{}^4I_{15/2}$	1534	200.303	46.234	246.537	1	4.056
$^4I_{11/2}\rightarrow{}^4I_{13/2}$	2822	27.489	9.507	299.474	0.124	3.339
$^4I_{15/2}$	976	262.478			0.876	
$^4I_{9/2}\rightarrow{}^4I_{13/2}$	1694	85.45		197.461	0.433	5.064
$^4I_{15/2}$	800	112.011			0.567	
$^4F_{9/2}\rightarrow{}^4I_{9/2}$	3554	3.436	3.03	2029	0.003	0.493
$^4I_{11/2}$	1933	126.801	7.718		0.066	
$^4I_{13/2}$	1147	84.96			0.042	
$^4I_{15/2}$	653	1803			0.889	
$^4S_{3/2}\rightarrow{}^4I_{9/2}$	1693	98.665		3366	0.029	0.297
$^4I_{11/2}$	1210	73.585			0.022	
$^4I_{13/2}$	847	921.885			0.274	
$^4I_{15/2}$	545	2272			0.675	
$^2H_{9/2}\rightarrow{}^4F_{9/2}$	1063	53.286	51.595	5412	0.019	0.185
$^4I_{9/2}$	818	27.509	1.162		0.005	
$^4I_{11/2}$	686	674.786	42.768		0.133	
$^4I_{13/2}$	552	2483			0.459	
$^4I_{15/2}$	405	2078			0.384	
$^4G_{11}\rightarrow{}^2H_{11/2}$	1369	42.342	14.366	29680	0.002	0.034
$^4F_{9/2}$	894	801.92	3.505		0.027	
$^4I_{9/2}$	714	300.563	0.851		0.011	
$^4I_{11/2}$	611	695.246	0.106		0.023	
$^4I_{13/2}$	502	2720	49.515		0.093	
$^4I_{15/2}$	380	25050			0.844	

Table 3.8. Radiative transition probability A, radiative lifetime τ_{rad} andfluorescent branching ratio β of Er^{3+} in $Ca_3Gd_2(BO_3)_4$ crystal at room temperature.

3.3.6 The spectrum characteristic of Yb^{3+}:$Ca_3Gd_2(BO_3)_4$ crystal

Fig.3.13 presents the absorption spectrum of $Ca_3Gd_2(BO_3)_4$:Yb^{3+}crystal, in which there is a broad absorption band ranged from 850 to 1000nm, corresponding to the transition from $^2F_{7/2}$ to $^2F_{5/2}$. The FWHM at 980 nm is about 12 nm and the cross-section is about 5.9×10^{-20} cm^2, which is benefit to the pumping of commercial laser diode. Table 3-9 shows the absorption properties of some ytterbium-doped compounds. The room temperature emission spectrum of $Ca_3Gd_2(BO_3)_4$:Yb^{3+} crystal excited at 895 nm is presented in Fig.3.14, in which there is a broad emission band ranged from 930 nm to 1100.7 nm. The FWHM of this emission band is 72.6 nm and its peak is located at 1020nm, which is resulted from the statistical distribution of Ca^{2+}, $Gd^{3+}$and Yb^{3+} ions.

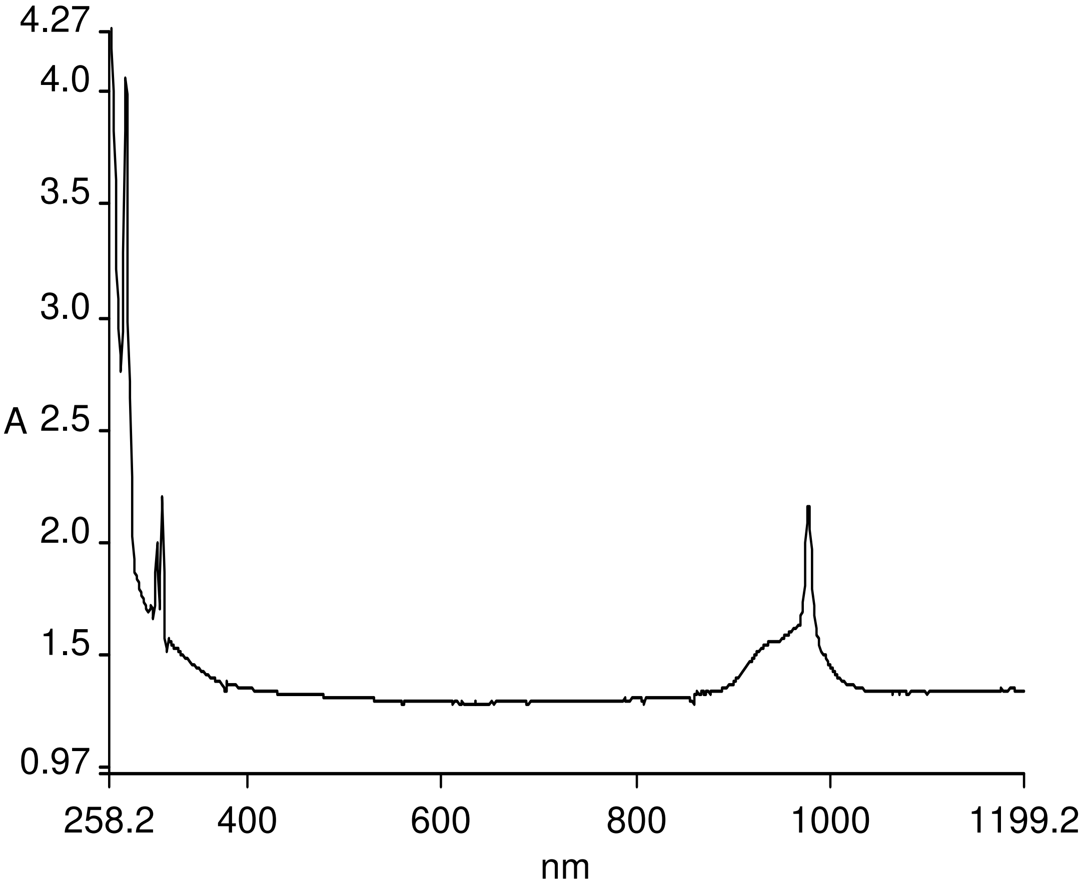

Fig. 3.13. The absorption spectrum of $Ca_3Gd_2(BO_3)_4$:Yb^{3+}crystal

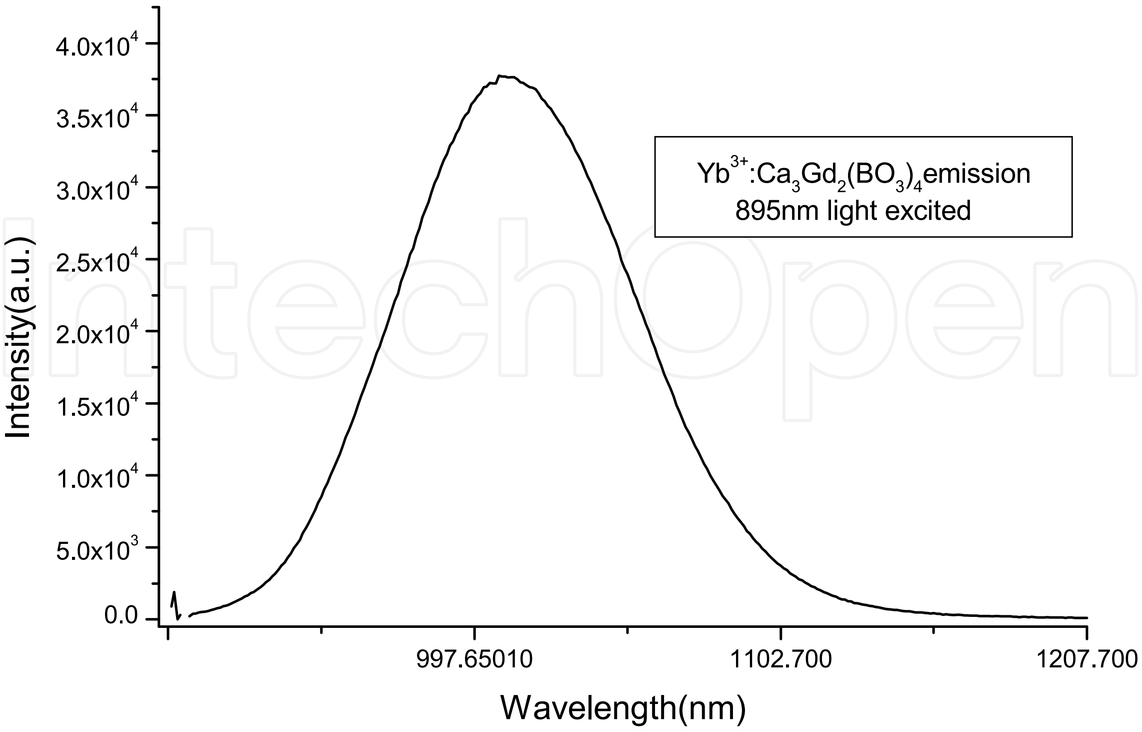

Fig. 3.14. Room temperature emission spectra of $Ca_3Gd_2(BO_3)_4$:Yb^{3+} crystal excited at 895 nm

Compound	λ_p(nm)	σ_a (×10^{-20} cm^2)	FWHM(nm)	References
5at%Yb:CGB	980	5.95	12	[5]
2at%Yb:YCOB	976.1	0.94	3	[61]
1at%Yb:Y_2SiO_5	977.4	2.1	7	[62]
1at%Yb:Sc_2SiO_5	979.5	1.9	4	[62]
Yb:GdCOB	976	0.87	2.6	[63]
15%Yb:YAG	968	0.94	2.6	[64]
15%Yb:BLuB	966	0.29	6.4	[64]
Yb:YAB	975	3.4	3	[65]

Table 3.9. Absorption properties of the ytterbium-doped compounds

3.4 The Laser characteristics of Yb^{3+}:$Ca_3Re_2(BO_3)_4$[Re=Y,Gd] crystals

3.4.1 The Laser characteristics of Yb^{3+}:$Ca_3Y_2(BO_3)_4$ crystal[66~69]

An passively mode-locked Yb:$Y_2Ca_3(BO_3)_4$ (Yb:CYB) laser with a partially reflective semiconductor saturable-absorber mirror was achieved. The 244 fs pulses with a repetition rate of ~55 MHz were obtained at the central wavelength of 1044.7 nm. The measured average output power amounted to 261 mW. This was the first demonstration of femtosecond laser in Yb:CYB crystal. Fig.3.15 shows the experimental setup of the laser oscillator. The input mirror M1 was a flat mirror coated with high reflection (HR) in a broad band from 1010 to 1060 nm and high transmission (HT) at 976 nm. The two folding mirrors, M2 and M3, were concave and had the radii of curvature of 1000 and 500 mm, respectively. Both of which were HR-coated placed near normal incidence (~3°). A SESAM with a reflection of 96% at 1040 nm was employed, which had a modulation depth of 1.6% and saturation fluence of 70 μJ/cm^2. Fig.3.16 presents the continuous wave and mode locking average output power versus the absorbed pump power. We can see that the threshold absorbed pump power was 1.9 W and a maximum output power of 783 mW was obtained under the absorbed pump power of 7.0W. The laser oscillation was achieved with the threshold absorbed pump power of 2.8 W when the output coupler was replaced by the SESAM. Within the range of absorbed pump power from threshold to 4.6W, a metastable regime rapidly alter-nating between Q-switched mode locking and continuous wave (CW) mode locking was observed.

Fig.3.17 presents the central wavelength and FWHM of the emission spectrum for mode locking operation. The spectrum was red-shifted obviously at a range from 1041.5 to 1044.7 nm with the absorbed pump power increased from threshold to 7.0 W, which was possibly attributed to the reabsorption effect for quasi-three-level system as the short wavelength part of the absorption spectrum overlaps the emission spectrum. Fig.3.18 shows the pulse train of the cw mode-locked laser with the repetition rate of ~55MHz. Fig.3.19 presents the autocorrelation trace of the 244 fs pulse with the average output power of 261 mW at the central wavelength of 1044.7 nm. The corresponding spectrum had a FWHM of 8.1 nm centered at 1044.7 nm, with a time bandwidth product of 0.54. In this job, a partially reflective SESAM was used as the output coupler that would lower the positive dispersion. When the absorbed pump power was fixed at 7.0 W, the adjustment of the Yb:CYB crystal and SESAM in such a resonator (by either moving or rotating that could vary the amount of material that the light went through) is critical for the stability of mode-locking operation and pulse duration: an average output power of 375 mW could be obtained but the mode locking was unstable; the duration also fluctuated in a wide range from ~1000 to 244 fs.

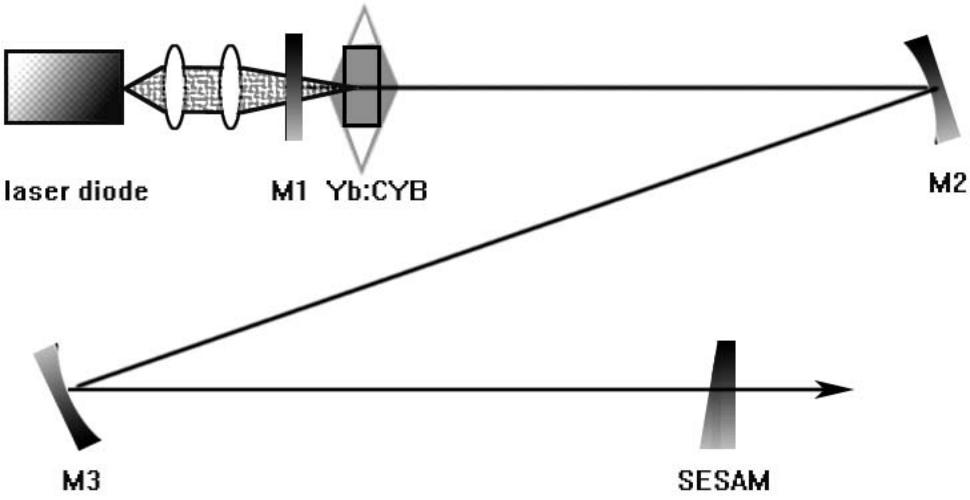

Fig. 3.15. Experimental setup of the laser oscillator. The shaded part in the position of the gain medium refers to the change in shape resulting from the thermal expansion

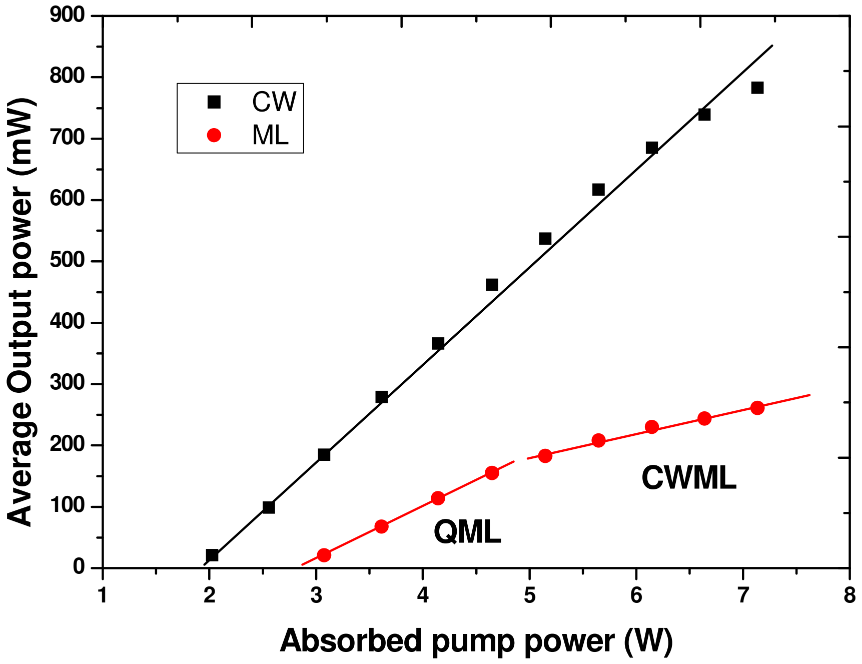

Fig. 3.16. The continuous wave and mode locking average output power versus the absorbed pump power

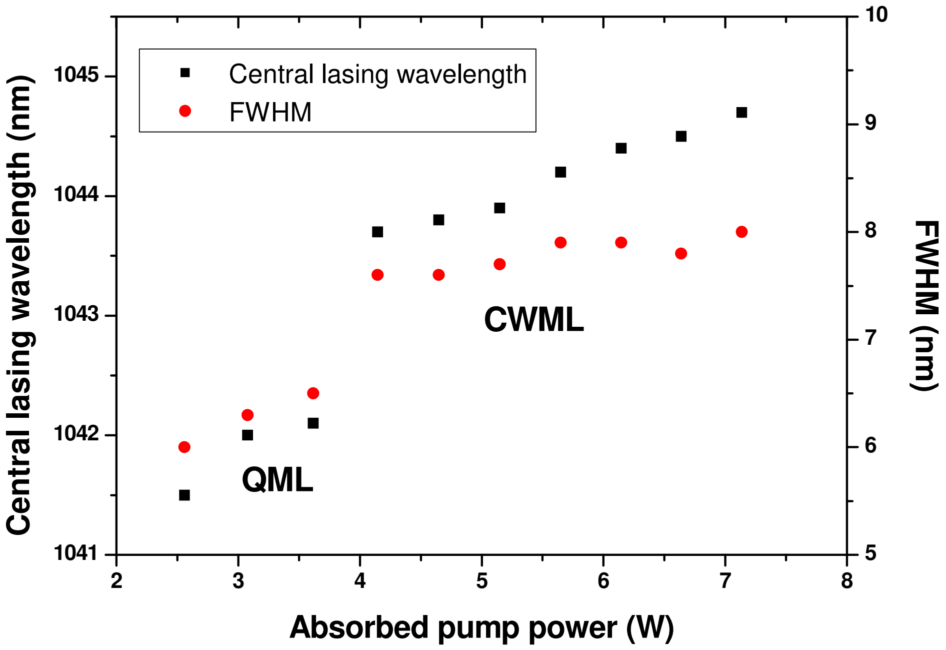

Fig. 3.17. The central wavelength and FWHM of the emission spectrum for mode locking operation

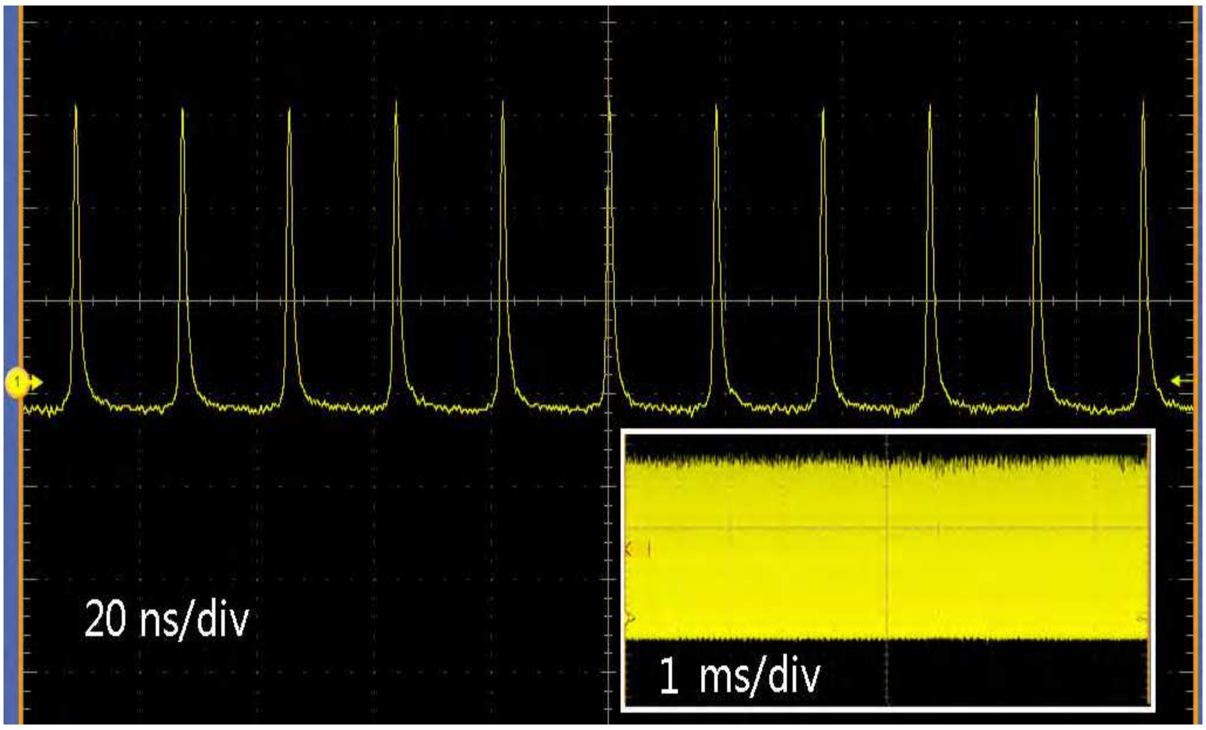

Fig. 3.18. The pulse train of the cw mode-locked laser with the repetition rate of ~55MHz

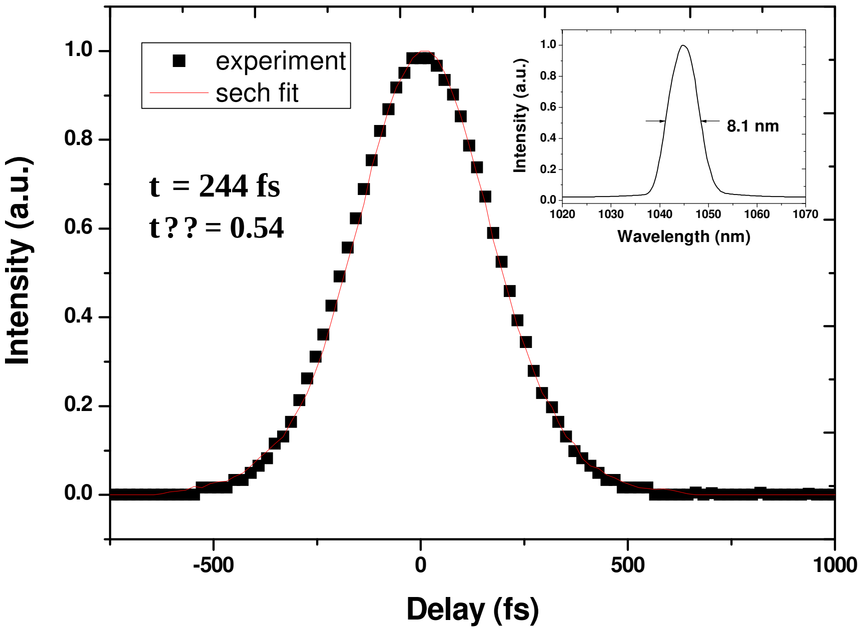

Fig. 3.19. The autocorrelation trace of the 244 fs pulse with the average output power of 261 mW at the central wavelength of 1044.7 nm. And the inset corresponding to the spectrum.

Q-switching and Q-switched mode-locked Yb:$Y_2Ca_3B_4O_{12}$ lasers with an acousto-optic switch are demonstrated. In the Q-switching case, an average output power of 530 mW is obtained at the pulse repetition rate of 10.0 kHz under the absorbed pump power of 6.1 W. The minimum pulse width is 79 ns at the repetition rate of 1.7 kHz. The pulse energy and peak energy are calculated to be 231 μJ and 2.03 kW, respectively. In Q-switched mode-locking case, the average output power of 64 mW with a mode-locked pulse repetition rate of 118 MHz and Q-switched pulse energy of 48 μJ is generated under the absorbed pump power of 6.1W. Fig.3.20 presents the CW and Q-switched average output power versus absorbed pump power. The CW lasers were operated with the absorbed pump power of up to 0.8 W and 1.3 W, respectively, for T = 1% and T = 5% output coupler. When the absorbed pump power reaches 6.1W, the T = 5% output coupler provides the best performance with an output power of 992 mW, which is much higher than 760 mW by using T = 1% output coupler. Fig.3.21 gives the emission spectra of the Yb:CYB laser with plano-concave cavity configuration. (a) is in the CW situation with T = 5% output coupler. (b)–(d) are in the Q-switching situation with T = 5% output coupler, (e) is in the Q-switching situation with T = 1% output coupler the emission spectra of the Yb:CYB laser. Fig.3.22 shows the pulse width versus absorbed pump power. At the pulse repetition rate of 1.7 kHz and the absorbed pump power 6.1 W, the pulse widths of 79 ns and 114 ns are detected by used of T = 1% and 5% coupler, respectively. Fig.3.23 presents the pulse energy and pulse peak power versus the absorbed pump power at the pulse repetition rate of 1.7kHz. The pulse energy of 231 μJ and peak energy of 2.03 kW can be obtained with the T = 5% output coupler. Fig.3.24 gives the single pulse profile of the A-O Q-switched Yb:CYB lasers with the pulse width of 76 ns at the absorbed pump power of 6.1 W, and the inset corresponding to the temporal pulse trains with the repetition rate of 1.7 kHz. The beam quality M2 is measured to be about 1.4 by using the knife-edge scanning method.

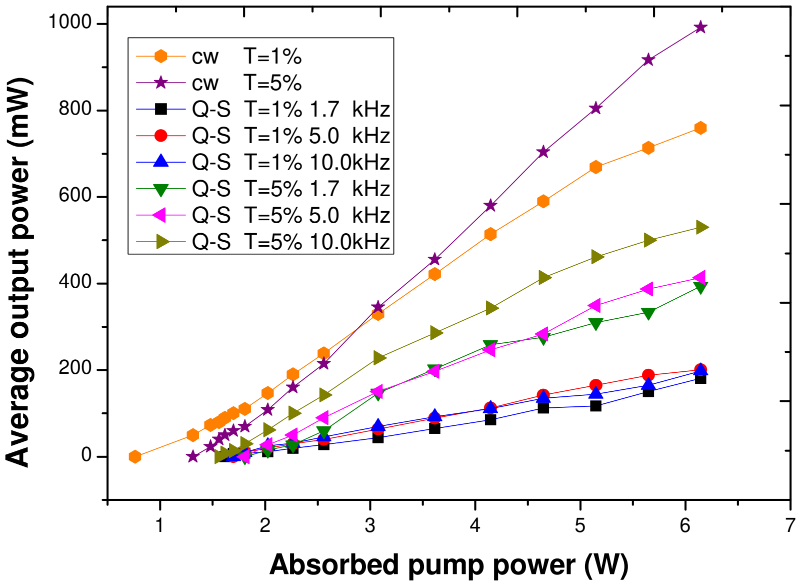

Fig. 3.20. The CW and Q-switched average output power versus absorbed pump power for *T* = 1% and 5%

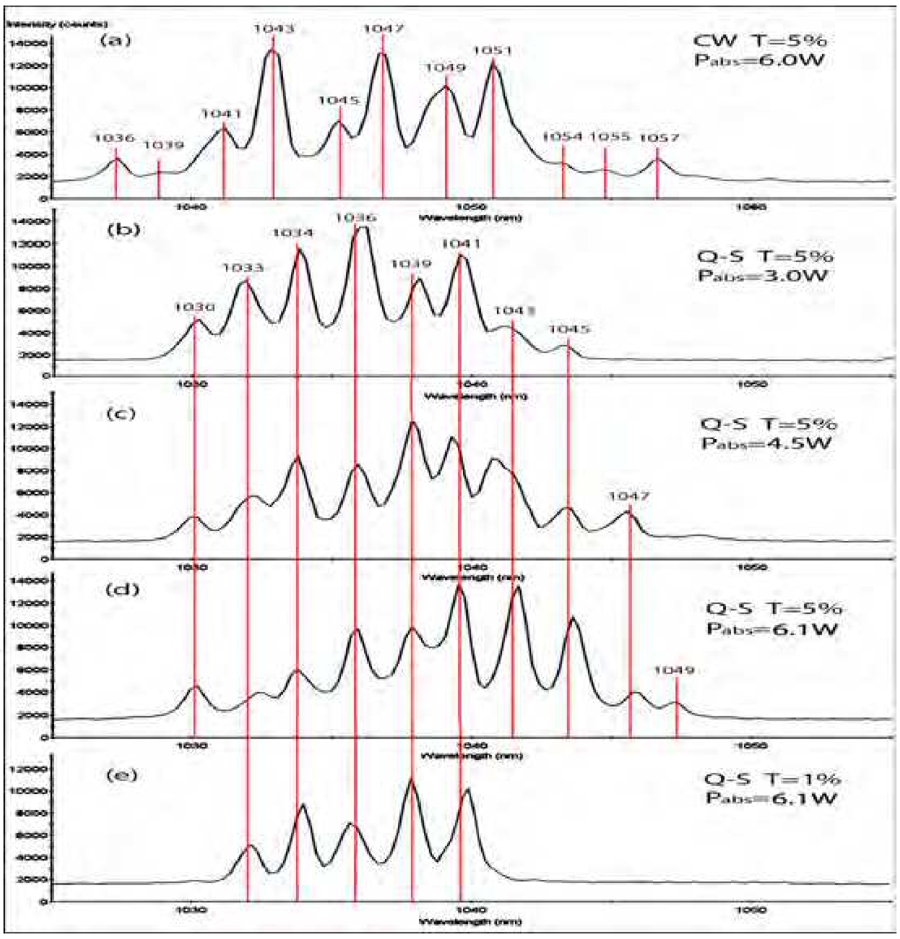

Fig. 3.21. Emission spectra of the Yb:CYB laser.(a) is in CW situation with *T* = 5%. (b)-(d) are in Q-switching situation with *T* = 5%, showing the absorbed pump power dependence. (e) is in Q-switching situation with *T* = 1%.

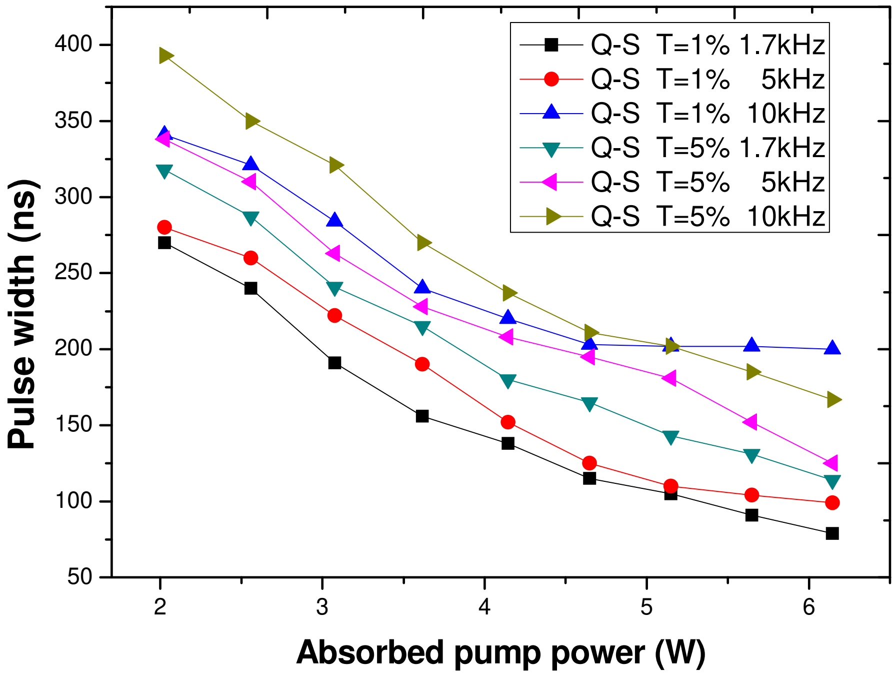

Fig. 3.22. Pulse width versus absorbed pump power

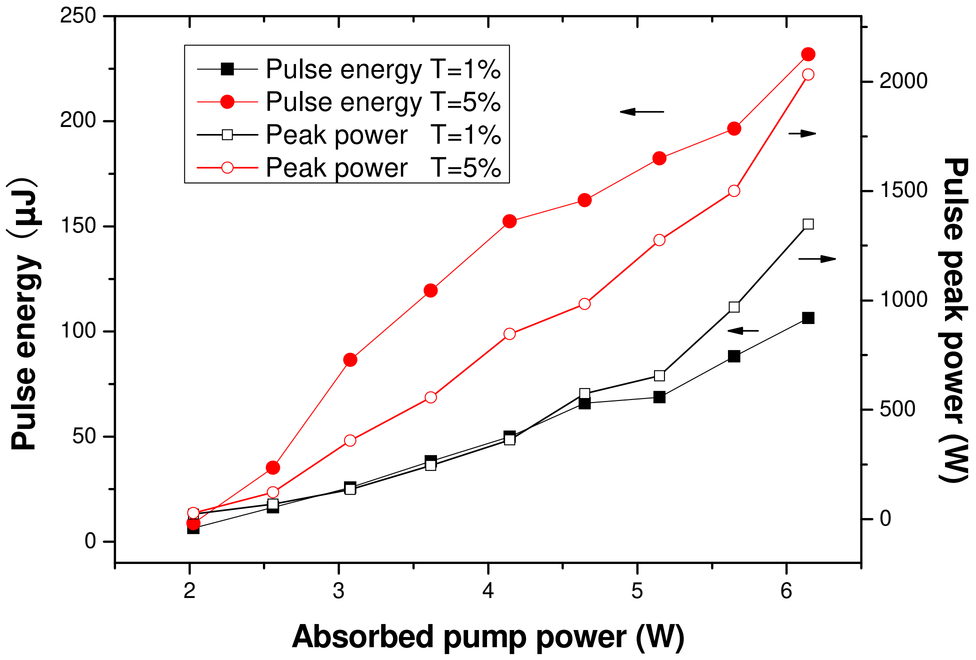

Fig. 3.23. Pulse energy and pulse peak power versus the absorbed pump power at the pulse repetition rate of 1.7kHz

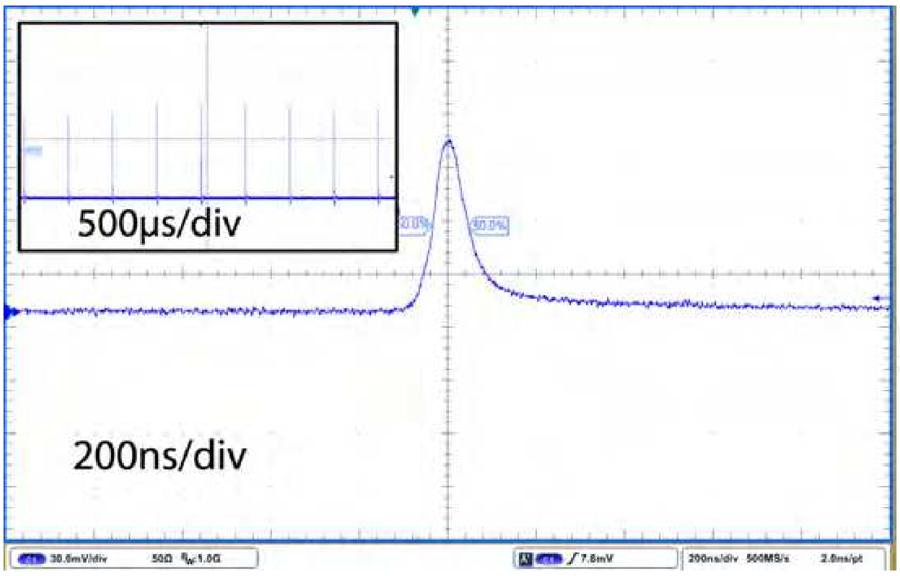

Fig. 3.24. The single pulse profile of the A-O Q-switched Yb:CYB lasers with the pulse width of 76 ns at the absorbed pump power of 6.1 W

Fig.3.25 depicts the schematic arrangement of the four-mirror resonate cavity for Q-switched mode-locking operation. M1 is the same plane mirror as that in Q-switching case described above. M2 and M3 are two spherical concave mirrors with curvature of 500 mm and 100 mm, respectively, and HR coated from 1010 nm to 1060 nm. The two different concave couplers (r = 75 mm) with transmissions of 1% and 5% are also used as the output coupler M4. The distances L1 from M1 to M2, L2 from M2 to M3, L3 from M3 to M4 are set as 440 mm, 770 mm and 60 mm, respectively. Fig.3.26 shows the emission spectra of the Yb:CYB laser. (a)-(c) is in CW situation with T = 5% showing the absorbed pump power dependence. (d) is in Q-switched mode-locking situation with T = 5%, (e) is in Q-switched mode-locking situation with T = 1%. Compared with the spectra of the above plano-concave resonator, there are only three or four emission branches in Figs. 3.26 a–c, since the combined etalon effects of the resonant cavity and uncoated Yb:CYB are different between the two-mirror and four-mirror cavity. Under the absorbed pump power of 3.0 W, there are three nonoverlapping emission branches located at 1042 nm, 1047 nm and 1051 nm. Similar to that in the Q-switched mode, the spectrum shifts to the long side with the increase of the absorbed pump power owing to the reabsorption effect. When the absorbed pump power reaches 6.1 W, a new branch in the short side (1040 nm) appears. The CW and Q-switched average output power versus absorbed pump power for T = 1% and 5% are plotted in Fig.3.27, (a) is T = 1% and (b) is T = 5%. The average output powers of 64 mW and 87 mW are obtained for T = 1% and T = 5% output coupler, respectively. Fig.3.28 shows the pulse energy of the Q-switched envelope versus the absorbed pump power at repetition rate of 1.7 kHz. In Fig.3.29, (a) is the oscilloscope traces of Q-switched pulse train with the T = 5% output coupler and the repetition rate of 1.7 kHz under the absorbed pump power of 6.1 W in the same situation. (b) is the typical QML pulse envelope of T = 5% in the same situation. (c) is the expanded traces of mode-locked train. The repetition rate of the periodic mode-locked pulses is about 118 MHz, which matches exactly with the axial mode interval. The output beam density distribution is close to the fundamental transverse mode (TEM00) and the quality parameter M2 factor is about 1.6.

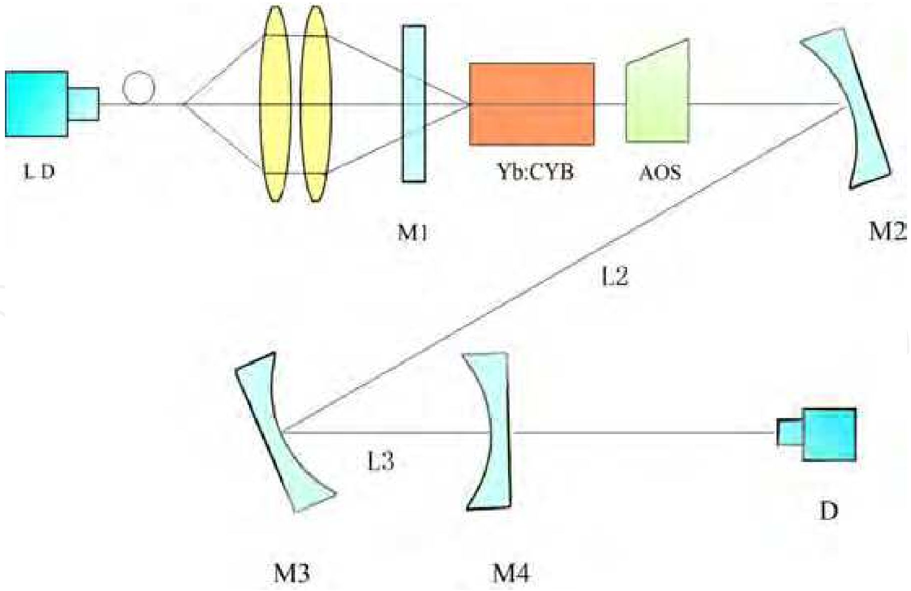

Fig. 3.25. The schematic arrangement of the four-mirror resonate cavity for Q-switched mode-locking operation

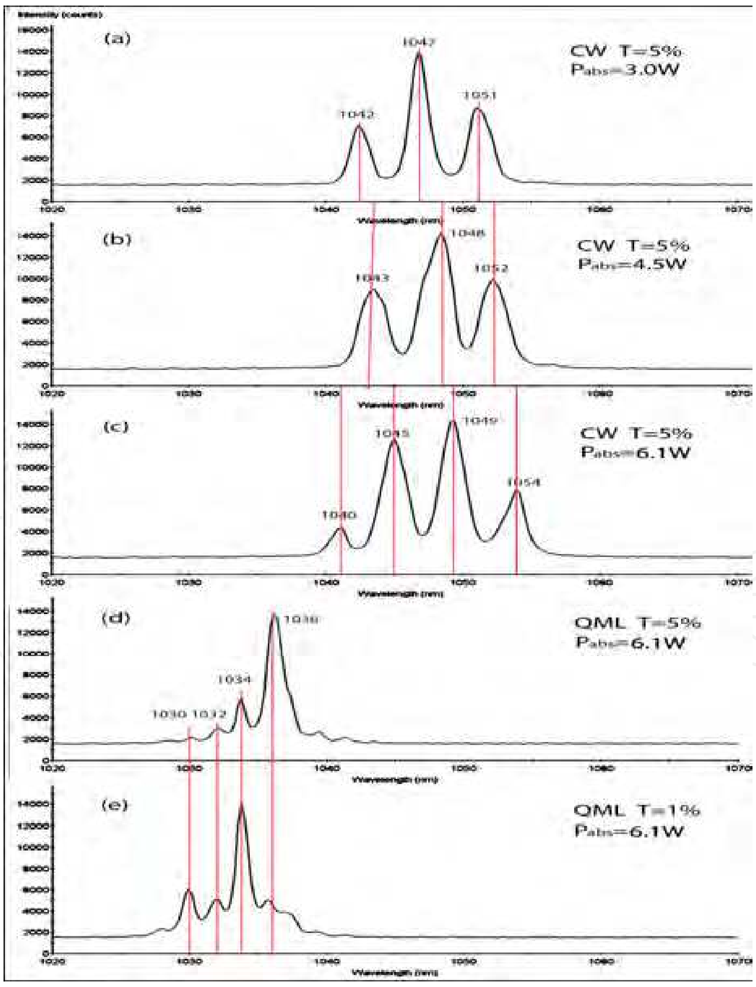

Fig. 3.26. Emission spectra of the Yb:CYB laser. (a)-(c) is in CW situation with T = 5% showing the absorbed pump power dependence.

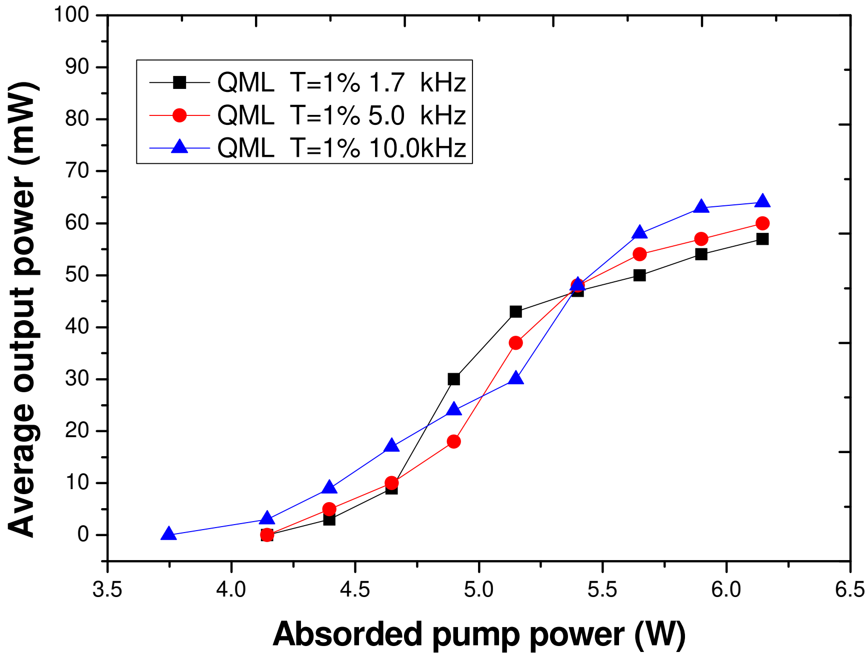

(a)

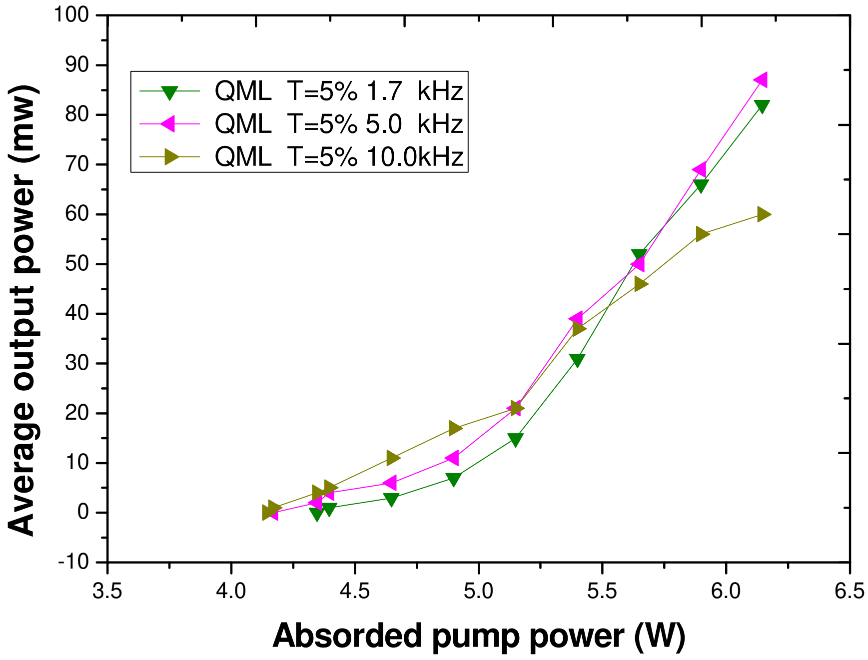

(b)

Fig. 3.27. The CW and Q-switched average output power versus absorbed pump power for *T* = 1% and 5%. (a) is *T* = 1% and (b) is *T* = 5%.

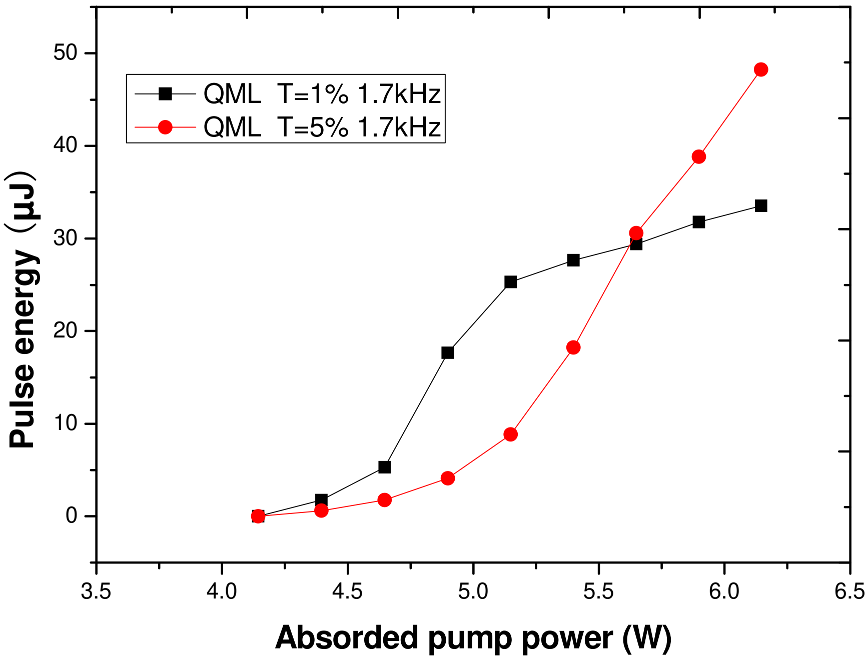

Fig. 3.28. Pulse energy of the Q-switched envelope versus the absorbed pump power at repetition rate of 1.7 kHz.

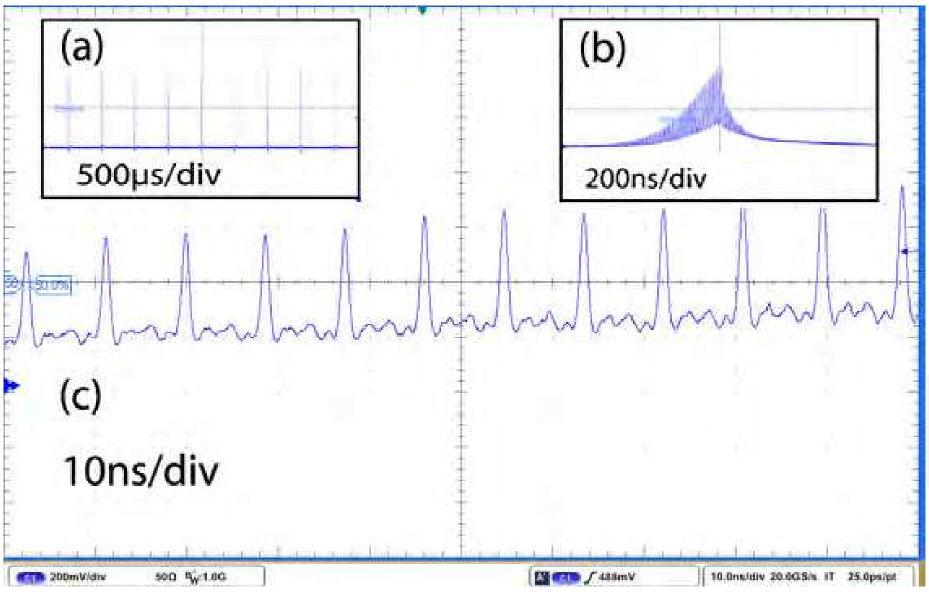

Fig. 3.29. (a) is the oscilloscope traces of Q-switched pulse train with the $T = 5\%$ output coupler and the repetition rate of 1.7 kHz under the absorbed pump power of 6.1 W in the same situation. (b) is the typical QML pulse envelope of $T = 5\%$ in the same situation. (c) is the expanded traces of mode-locked pulses.

The Yb^{3+}-doped $Y_2Ca_3B_4O_{12}$ diode-pumped laser operation in both continuous-wave (CW) and passively Q-switched modes was reached. The differential slopes of the CW output power are in the 22-40 % range under different experimental conditions. Continuous tuning of the laser wavelength is obtained in the 1020-1057 nm range, in agreement with the broad emission spectra. In pulsed regime the repetition rate occurs up to 1.6 kHz and pulse energies of 30-75 μJ with about 40 ns duration are obtained. Fig.3.30 demonstrates the polarized emission spectra of the CYB:Yb^{3+} crystal used for laser experiments. The two orthogonal polarizations of the eigenstates are labeled as *H* and *V*. The main peak at 976.3 nm has 6 nm full width at half maximum (FWHM) and is suitable for diode pumping. Fig.3.31 displays the spectral distribution of the laser emission in CW and passive *Q*-switch modes. We can see that the more intense one corresponds to the H polarization with a broadband peaking near 1040 nm. The time evolution of the fluorescence was displayed with a 9410 Lecroy oscilloscope. The decay time was found to be 1 ms. Fig.3.32 presents repetition rates and pulse energies obtained in passive *Q* switching the $Ca_3Y_2(BO_3)_4$:Yb^{3+} laser. Lasing was obtained in H polarization in agreement with the polarized emission spectra, near 1045 nm (with the 97.5% transmission coupler) and up to 1 W power. Fig.3.33 shows the tunability of the laser emission obtained from rotation of a birefringent filter. Fig.3.34 presents the laser output power versus pump power obtained under different experimental conditions. The obtained slope efficiencies were in the 29%–40% range with the 5 cm radius curvature output coupler and 22% with the 7.5 cm coupler. Table 3-10 shows the pulse energy obtained in passive Q-switching different Yb^{3+}-doped hosts. In particular, we can see that the performances for Yb^{3+} doped GGG and GAB crystals obtained with similar experimental conditions were better than for Yb^{3+}:CYB, with no instability of the pulsed regime and less thermal problems. A plausible explanation is the lower laser emission cross section in Yb^{3+}:CYB and a too low absorbed pump power (61% absorption) of our sample.

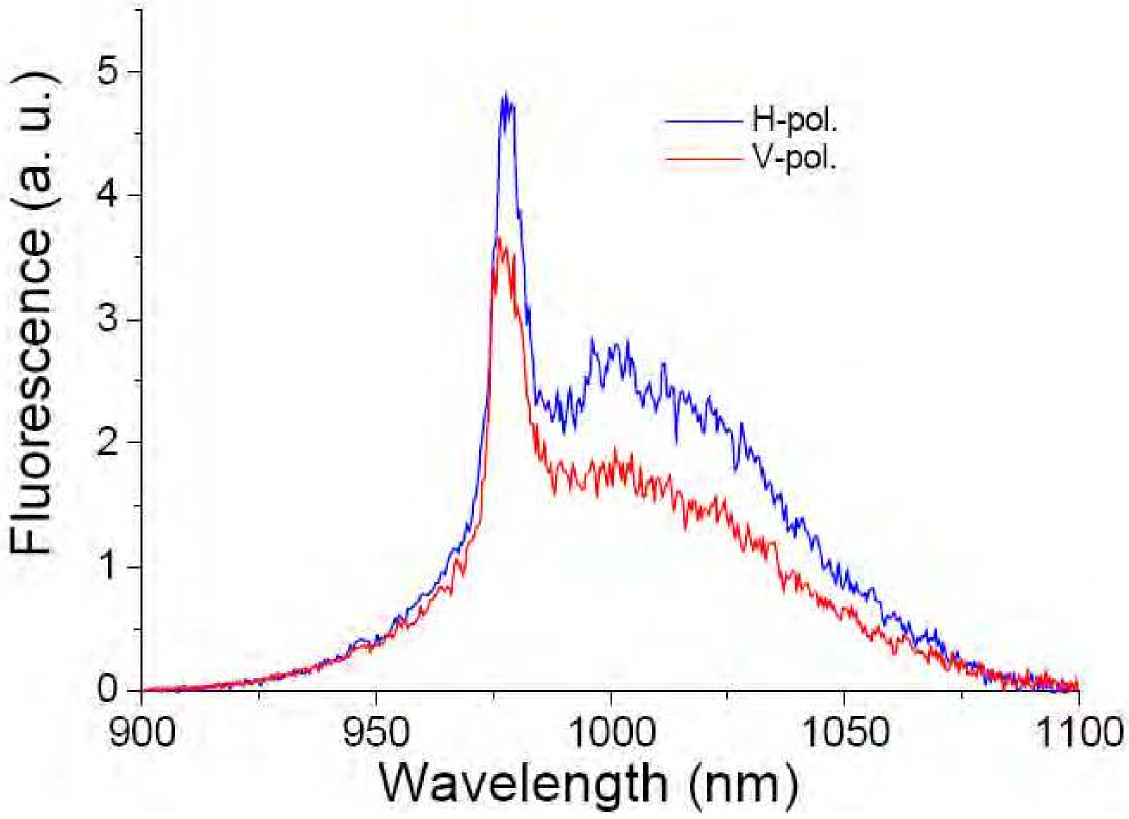

Fig. 3.30. Polarized emission spectra of the CYB:Yb^{3+} crystal used for laser experiments

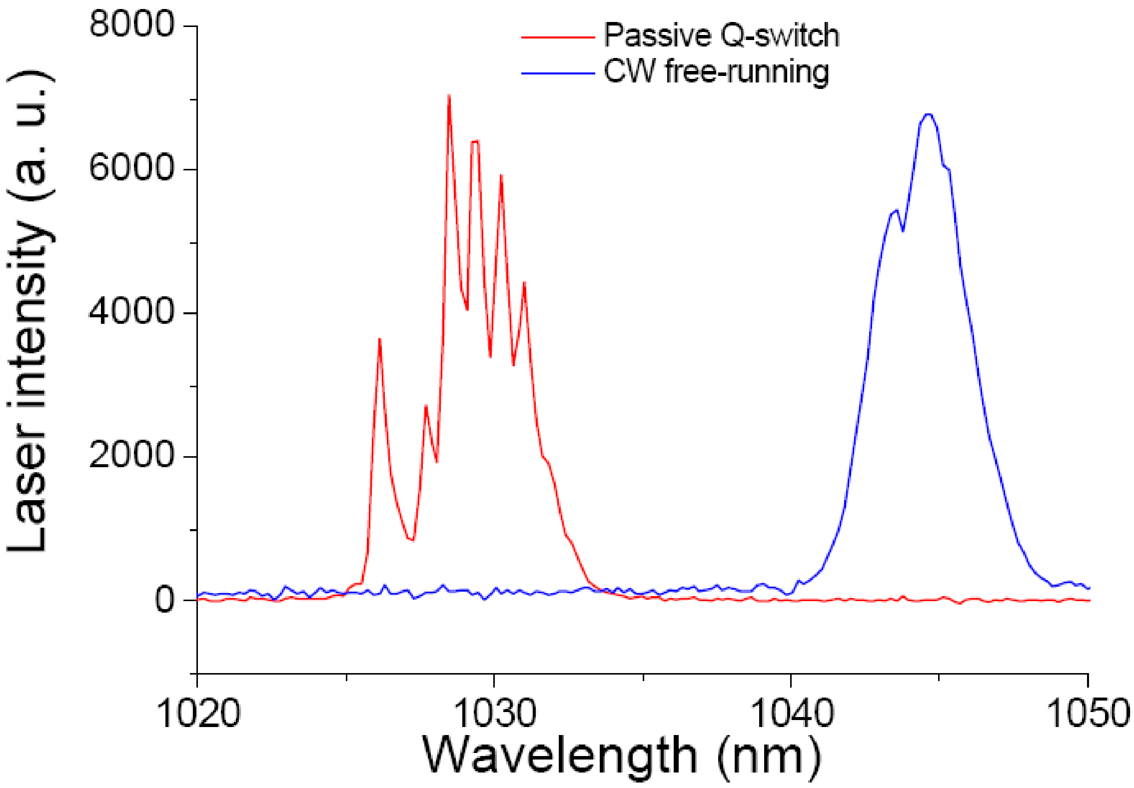

Fig. 3.31. Spectral distribution of the laser emission in cw and passive *Q*-switch modes

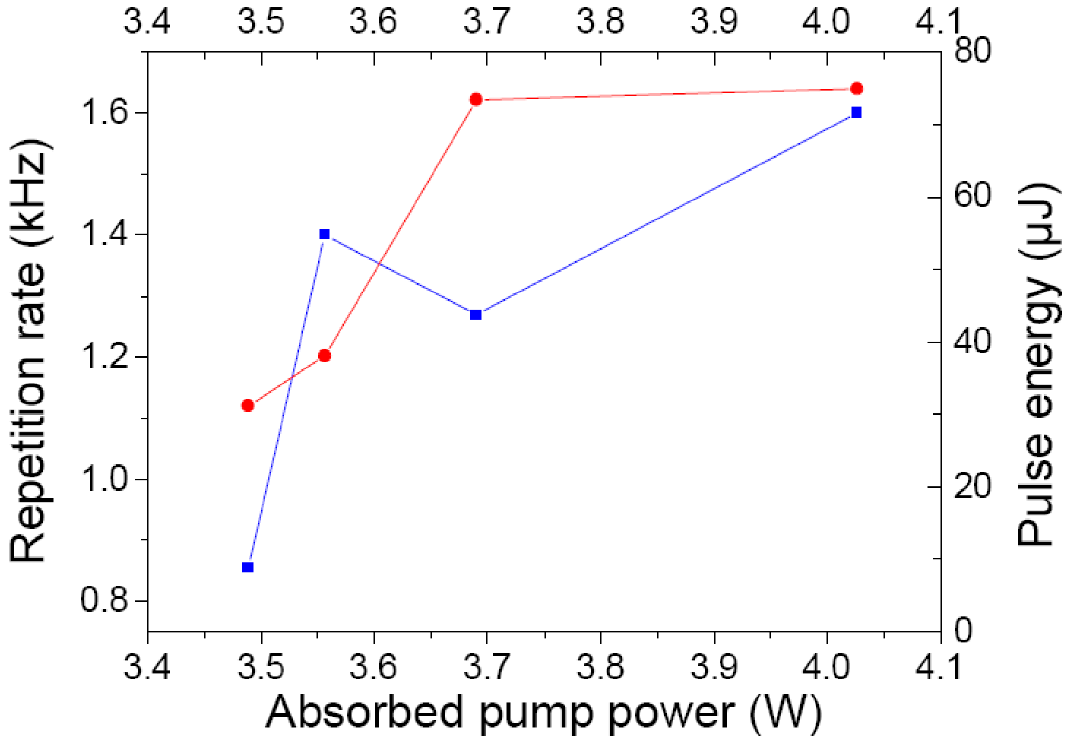

Fig. 3.32. Repetition rates and pulse energies obtained in passive *Q* switching the $Ca_3Y_2(BO_3)_4:Yb^{3+}$ laser. The inset represents a typical time evolution of the laser pulse

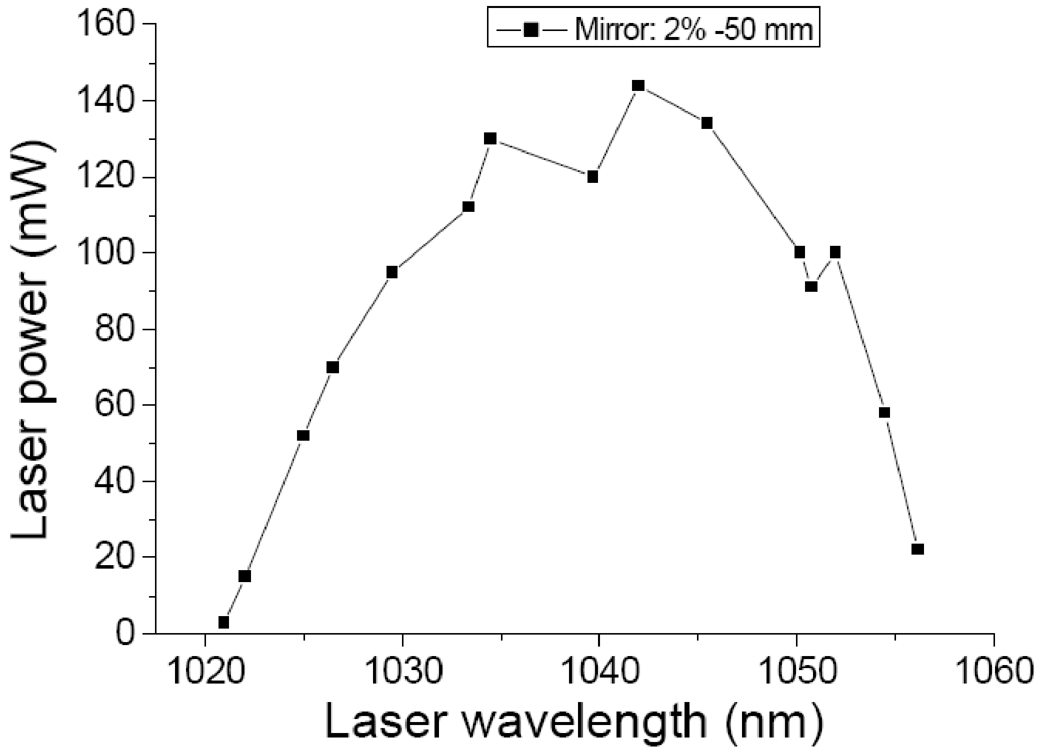

Fig. 3.33. Tunability of the laser emission obtained from rotation of a birefringent filter

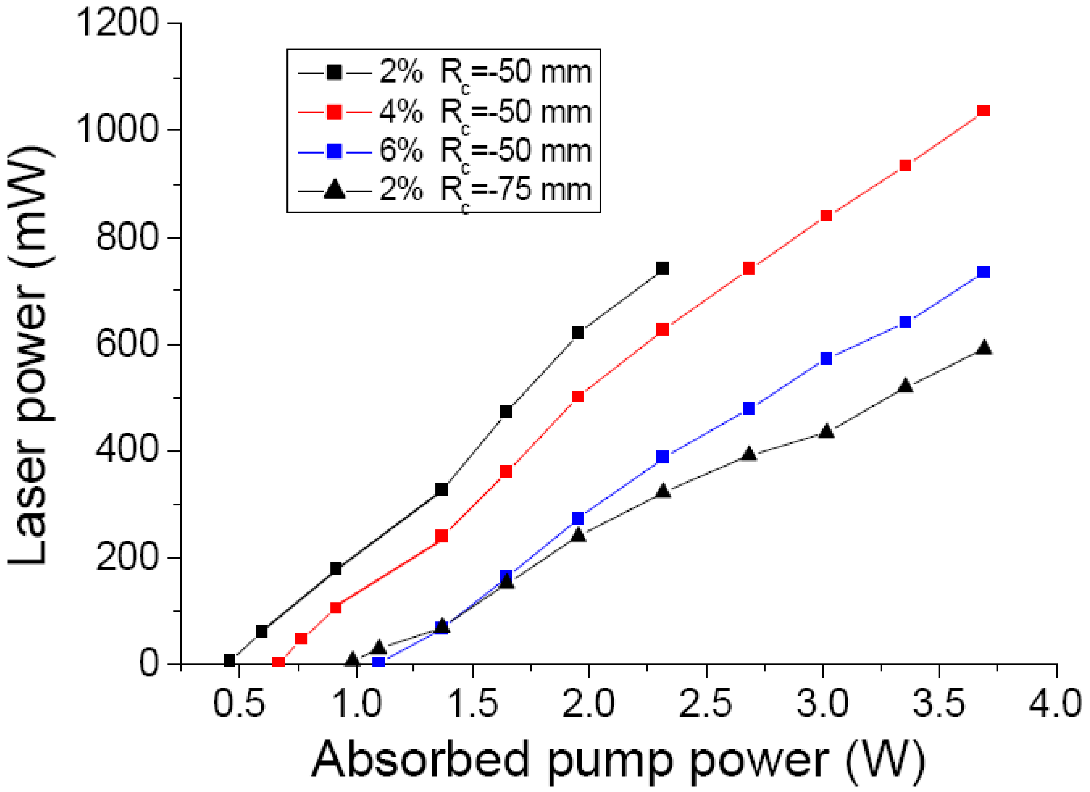

Fig. 3.34. Laser output power versus pump power obtained under different experimental conditions.

Crystal	cw emission wavelength (nm)	Lifetime τ (μs)	Emission cross section (10^{-20}cm^2) at cw lasing wavelength	Pulse energy (μJ)
Yb^{3+}:KGdW	1029	951	2.7	3.4[70]
Yb^{3+}:KLuW	1031.7	…	…	32.4[71]
Yb^{3+}:YAG	1023	600	2.03	54,100,179,500[72]
Yb^{3+}:GGG	1025	800	2.0	40,48,87,96[73]
Yb^{3+}:GAB	1045	800	0.83	125,165[74]
Yb^{3+}:CYB	1044	1000	0.60	30-70[69]

Table 3.10. Pulse energy obtained in passive Q-switching different Yb^{3+}-doped hosts

3.4.2 The laser characteristics of Yb^{3+}:$Ca_3Gd_2(BO_3)_4$ crystal[75]

The diode-pumped multi-wavelength continuous-wave laser operation of the disordered Yb:$Ca_3Gd_2(BO_3)_4$ (Yb:CGB) crystal was investigated. The number of the oscillating wavelengths varied from two to five in the range from 1045.4 to1063.6 nm with the absorbed pump power and Yb:CGB crystal length. An output power of 1.4 W was obtained when quadruple wavelengths were emitted simultaneously, corresponding to a slope efficiency of 23.7%. The quintuple-wavelength oscillation at 1049.4, 1051.3, 1053.4, 1055.6 and 1057.4 nm was realized with an output power of 1.0 W. The experiment results exhibited the further possible application of Yb:CGB crystal in terahertz-wave generation. Fig.3.35 represents the experimental setup of the CW Yb:CGB laser oscillator. M1 was a plane mirror with antireflection coating at the pump wavelength and high-reflection coating at a broad band from 1040 to 1070 nm. A concave mirror with 75-mm curvature radius and ~99% reflectance from 1040 to 1070 nm was used as the output coupler M2. Fig.3.36 shows the absorbed pump power and absorption efficiency versus incident pump power for the two Yb:CGB samples, with the same cross section of 3×3 mm^2 but different lengths of 2 and 5 mm (described as sample 1 and 2, respectively). It can be seen that the absorption efficiency of sample 1 was around 40% if the incident pump power was below 4.0 W. But the efficiency decreased dramatically from 40% to 30% when the incident pump power was increased from 4.0 to 8.0 W. Then the efficiency was stable again, varying within a narrow range of 30% ~ 32 %. That was possibly attributed to the saturation of pump absorption to some extent, resulting from the depletion of the population in ground state. The similar phenomenon was observed when sample 2 was tested. Fig.3.37 depicts the relationship between the output power (P_{out}) and absorbed pump power for the two samples. The laser operation was realized with threshold absorbed pump powers of 0.4 and 0.9 W for sample 1 and 2, respectively. The maximum output power was 1.4 W by using sample 2 under the absorbed pump power of 6.8 W, with a slope efficiency of 23.7% and an optical conversion efficiency of 20.6%. The sample 1 exhibited higher slope efficiency of 30.3% and optical conversion efficiency of 27.0% with the output power of 1.0 W under the absorbed pump power of 3.7 W. Fig.3.38 gives the emission wavelengths versus absorbed pump power for the two Yb:CGB samples. Fig.3.39 and Fig.3.40 shows the emission spectra of the simultaneous multi-wavelength Yb:CGB laser with sample 1 and sample 2, repectively. It can seen that the emission wavelengths at each stage were almost same in intensity. That is advantageous to the practice terahertz-wave generation. If the quintuple-wavelength simultaneous emission is employed, multiple terahertz waves can be generated theoretically through difference frequency nonlinear interaction. Furthermore, it is interesting to note the separation of emission peaks varied from 1.0 to 2.0 nm with the absorbed pump power and Yb:CGB crystals, which means the multi-wavelength CW Yb:CGB laser could support the tunable terahertz-wave generation from 0.27 to 2.16 THz as calculated from Fig.3.38. Our experiment also showed that the reabsorption effect in quasi-three-level laser systems depended on the length of laser medium and the level of pump intensity. In addition, this effect had a great influence on the laser characteristics such as output power, optical efficiency and emission wavelength.

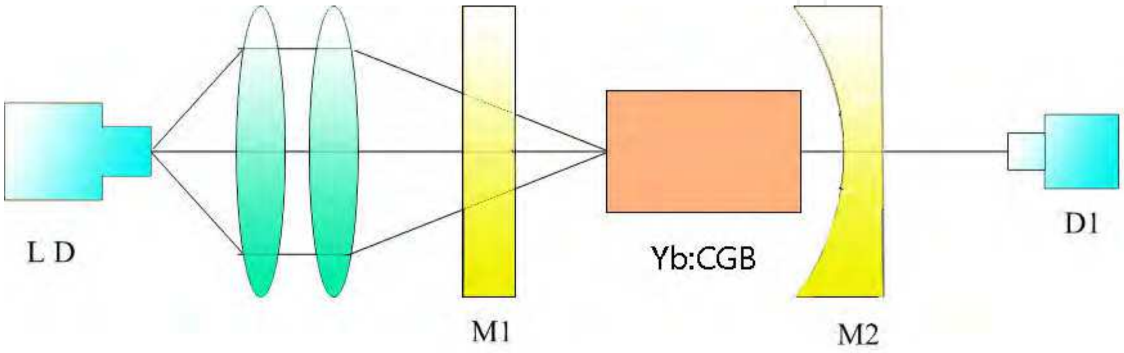

Fig. 3.35. Experimental setup of the CW Yb:CGB laser oscillator

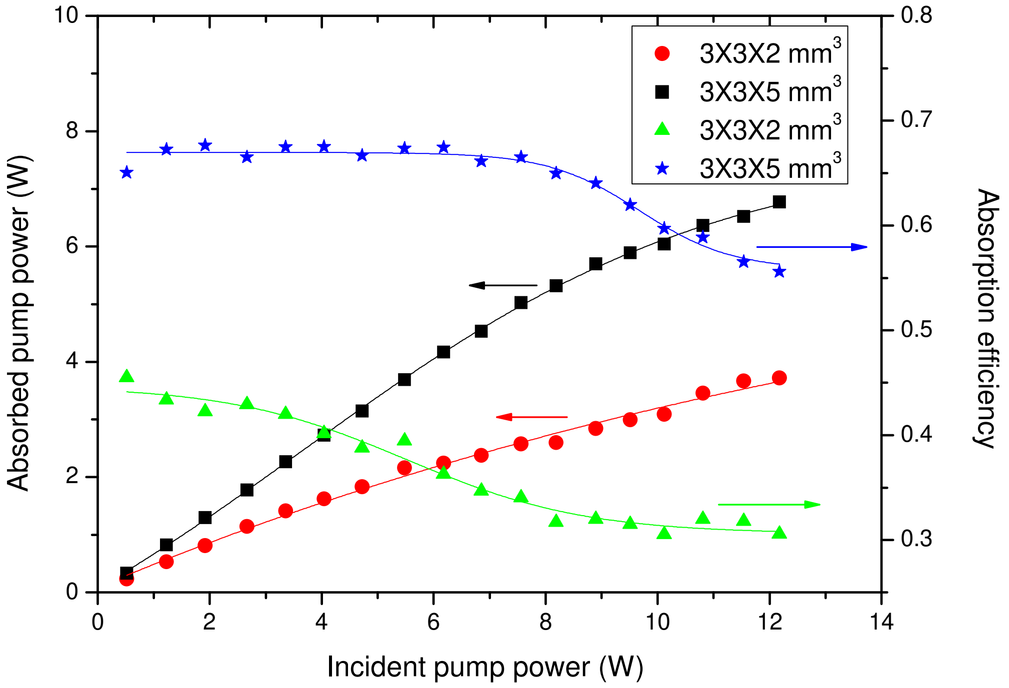

Fig. 3.36. Absorbed pump power and absorption efficiency versus incident pump power for the two Yb:CGB samples

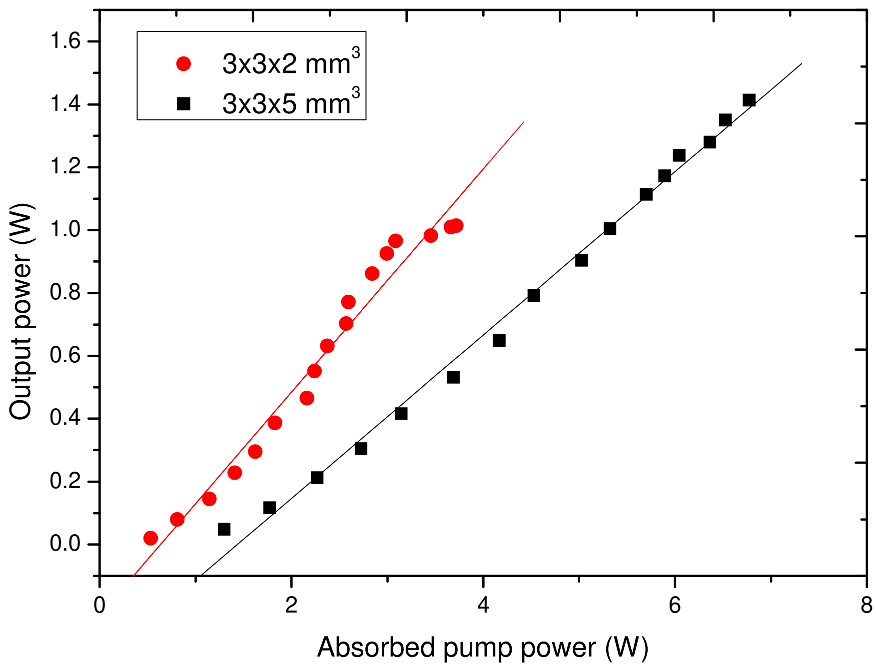

Fig. 3.37. Continuous-wave output power versus absorbed pump power of the Yb:CGB laser

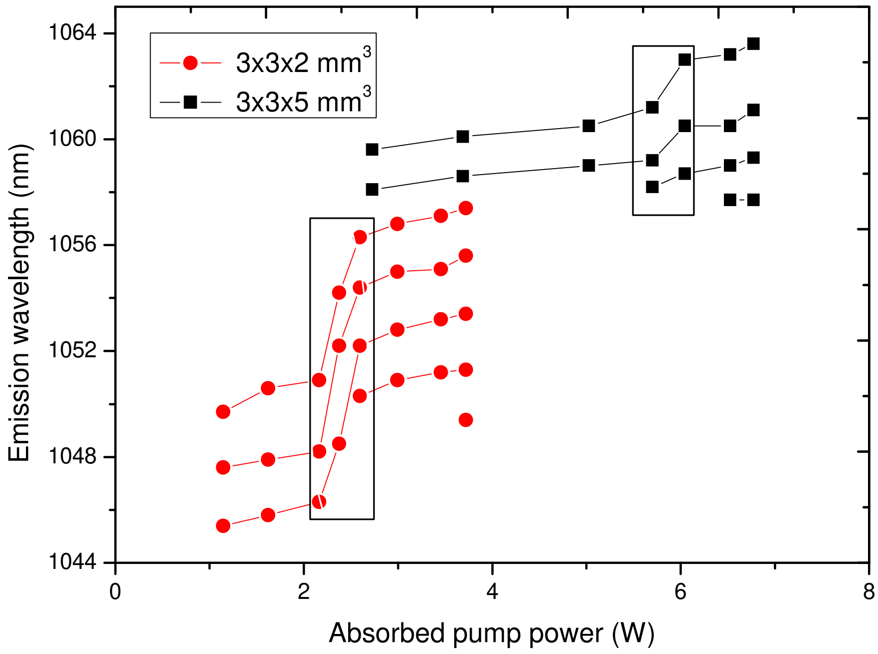

Fig. 3.38. Emission wavelengths versus absorbed pump power for the two Yb:CGB samples. The rapid redshift ranges are marked by squared pattern. The oscillating wavelengths varied in the region from 1045.4 to1063.6 nm with the absorbed pump power and Yb:CGB sample length.

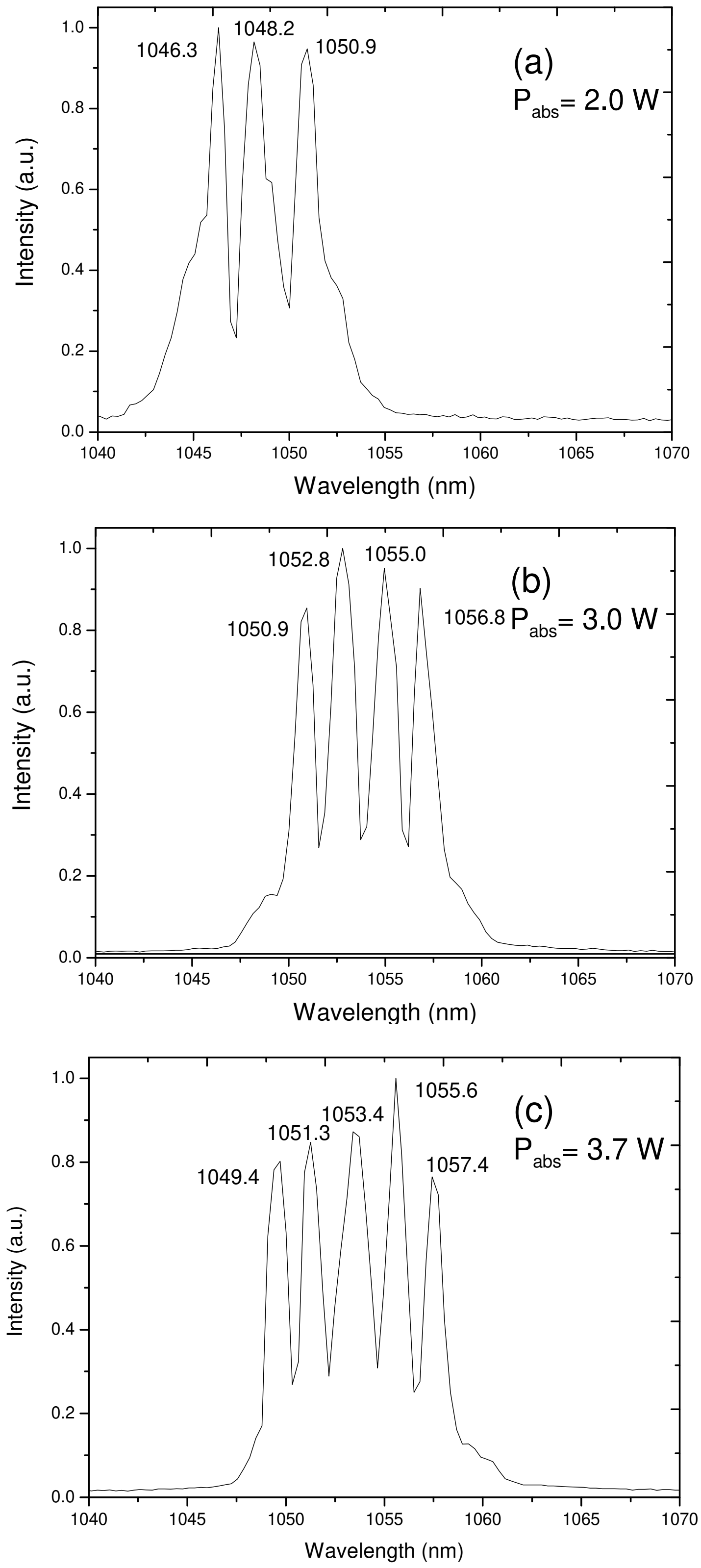

Fig. 3.39. Emission spectra of the simultaneous multi-wavelength Yb:CGB laser with sample 1. (a) triple-wavelength oscillation with P_{out} = 0.4 W and P_{abs} = 2.0 W; (b) quadruple-wavelength oscillation with P_{out} = 0.9 W and P_{abs} = 3.0 W; (c) quintuple-wavelength oscillation with P_{out} = 1.0 W and P_{abs} = 3.7 W.

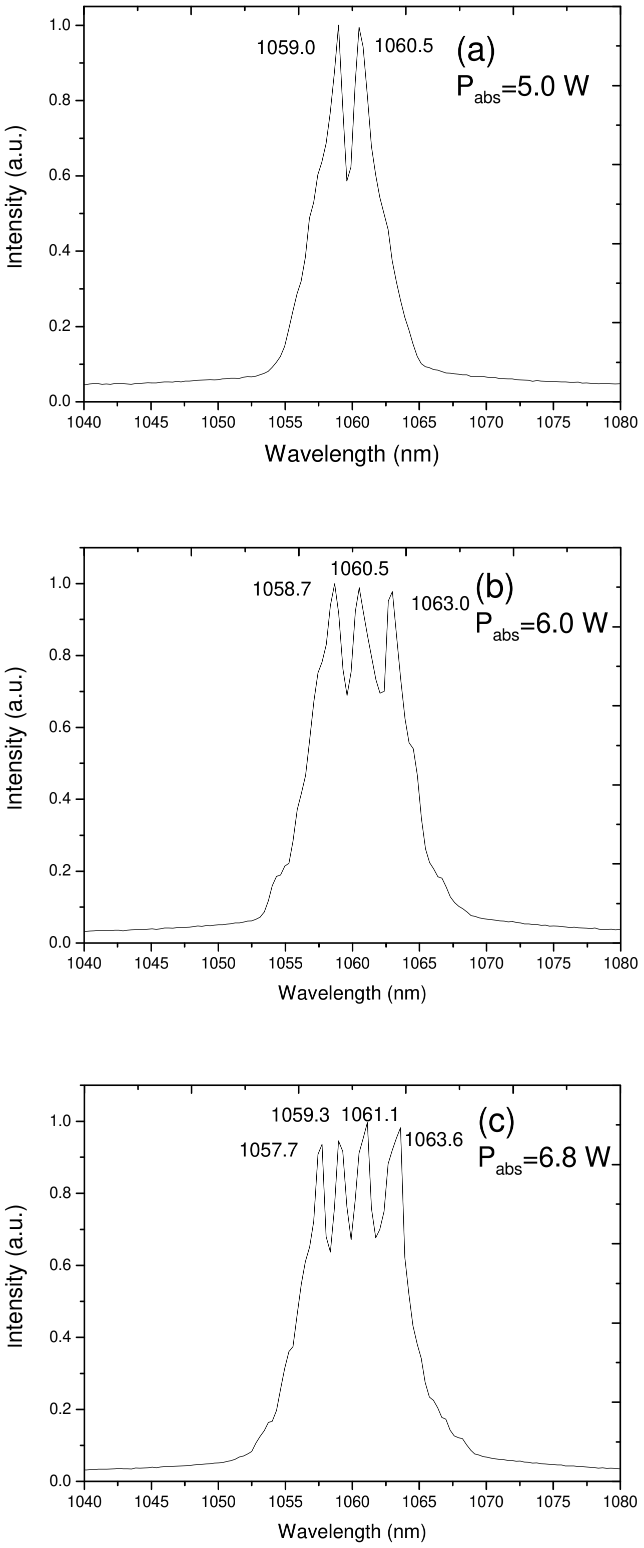

Fig. 3.40. Emission spectra of the simultaneous multi-wavelength Yb:CGB laser with sample 2. (a) is dual-wavelength oscillation with P_{out} = 0.9 W and P_{abs} = 5.0 W; (b) is triple-wavelength oscillation with P_{out} = 1.2 W and P_{abs} = 6.0 W; (c) is quadruple-wavelength oscillation with P_{out} = 1.4 W and P_{abs} = 6.8 W.

4. Nd^{3+}-doped LaB_3O_6 crystals

The LaB_3O_6 [LaBO] single crystal belongs to monoclinic system with the space group of I2/c [76,77]. The cell parameters are as follows[77]: a=9.946(1) Å, b=8.164(1) Å, c=6.4965(5) Å, β=127.06(1)°, [78]. V=420.9 Å^3, Dc=4.219 g/cm^{-3}. It melts congruently at 1145°C [76]. Therefore, this crystal can be obtained with large size by the Czochralski technique. Since the ionic radius of La^{3+} in LaB_3O_6 single crystal is about 1.04 Å [78], it can be substituted by laser exciting ions of lanthanide such as Nd^{3+}, Yb^{3+} ions. Therefore LaB_3O_6 crystal may be a new potential host for laser crystal. Furthermore, rare earth-doped LaB_3O_6 crystal can serve as a microchip laser crystal without any processing because of the cleavage of LaB_3O_6 crystal.

4.1 The crystal growth

Nd^{3+}-doped LaBO crystal with size up to ϕ20 mm×35 mm was grown using the Czochralski technique by Dr.Guohua Jia[4]. When the crystal was cut into laser bulk, it split into the cleavage crystal with the size of 2.5 mm×9 mm×35 mm as shown in Fig.4.1.

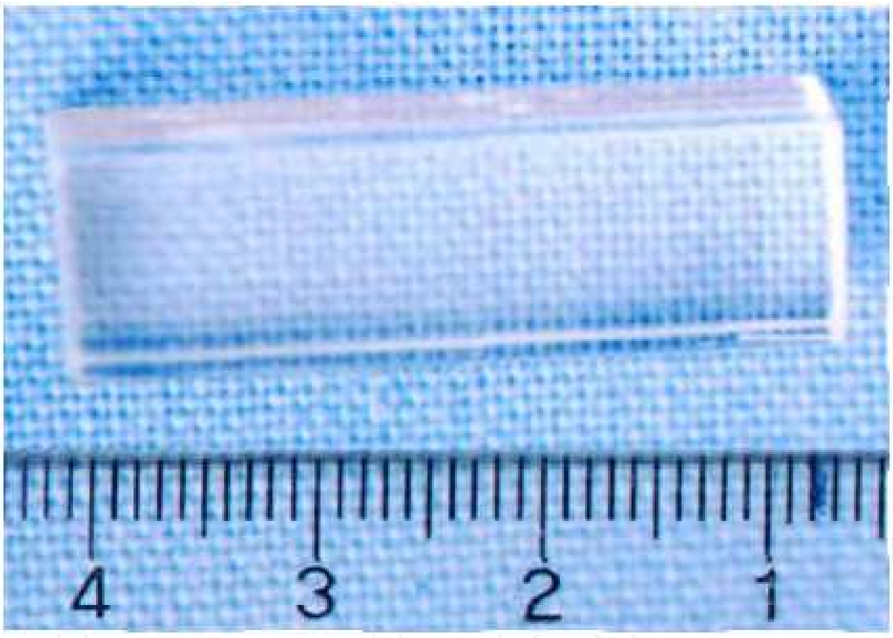

Fig. 4.1. Image of the unprocessed cleavage microchip along the (101) planes directly obtained from the as-grown crystal

4.2 The spectrum characteristics of Nd^{3+}-doped LaB_3O_6 crystal[80]

The room temperature absorption spectrum (Fig.4.2) consists of 10 groups of bands, which are associated with the observed transitions from the $^4I_{9/2}$ ground state. The absorption spectrum of the LaB_3O_6:Nd^{3+} crystal reaches its maximal value at about 800 nm and its FWHM is about 16 nm. The absorption cross-section was measured to be σ_{abs} = 3.37 × 10^{-20} cm^2. [7] This stronger absorption band corresponding to the transition $^4I_{9/2} \rightarrow {}^2H_{9/2}$ is very favorable for commercial GaAlAs diode pumping[4]. The room temperature emission spectrum with the light perpendicular to <1 1 1> planes is presented in Fig.4.3. The $^4F_{3/2} \rightarrow {}^4I_J$ (J = 9/2, 11/2, 13/2) transitions corresponding to the bands centered at 890.7, 1062 and 1329 nm, respectively, are the most important for laser applications. The value of the emission cross-section at 1062 nm of $LaB_3O_6:Nd^{3+}$ is 3.46×10^{-20} cm^2, which is a little smaller than that of other Nd^{3+} doped crystals. The emission cross-section and branching ratio (β) of the $^4F_{3/2} \rightarrow {}^4I_{9/2}$ transition are centered at 891 nm. The values of the emission cross-section at 891 nm and the branching ratio of this transition are 4.07×10^{-21} cm^2 and 0.336, respectively. Fig. 4.4 shows the room temperature fluorescence decay curve of $LaB_3O_6:Nd^{3+}$ crystal from which the fitting result of single exponential decay is 44.465 ns.

Table 4-1 shows the integrated absorbance, the experimental and calculated line and oscillator strengths of $Nd^{3+}:LaB_3O_6$ crystal (note: rms $f = 0.744 \times 10^{-6}$), and Table 4-2 presents the intensity parameters of $Nd^{3+}:LaB_3O_6$ crystal and the comparison of the intensity parameters of other Nd^{3+} doped crystals. Table 4-3 presents the calculated radiative probabilities, radiative branching ratios and radiative time for the emissions from the $^4F_{3/2}$ level of $LaB_3O_6:Nd^{3+}$. Table 4-4 shows the comparison of the $^4F_{3/2} \rightarrow {}^4I_{11/2}$ emission cross-section and radiative branching ratios of Nd^{3+} doped crystals.

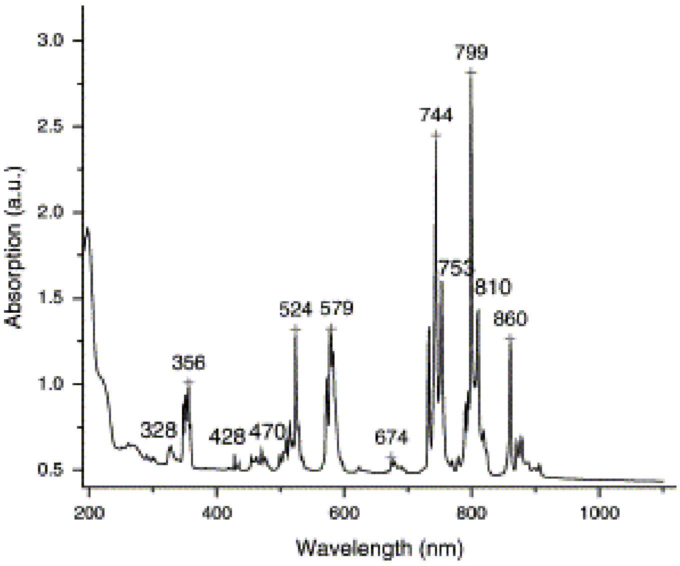

Fig. 4.2. The room temperature absorption spectrum

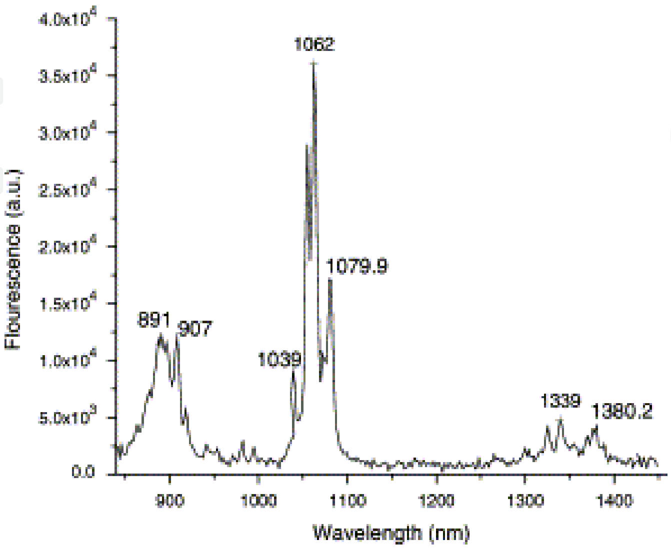

Fig. 4.3. Room temperature emission spectrum with the light perpendicular to <1 1 1> plane

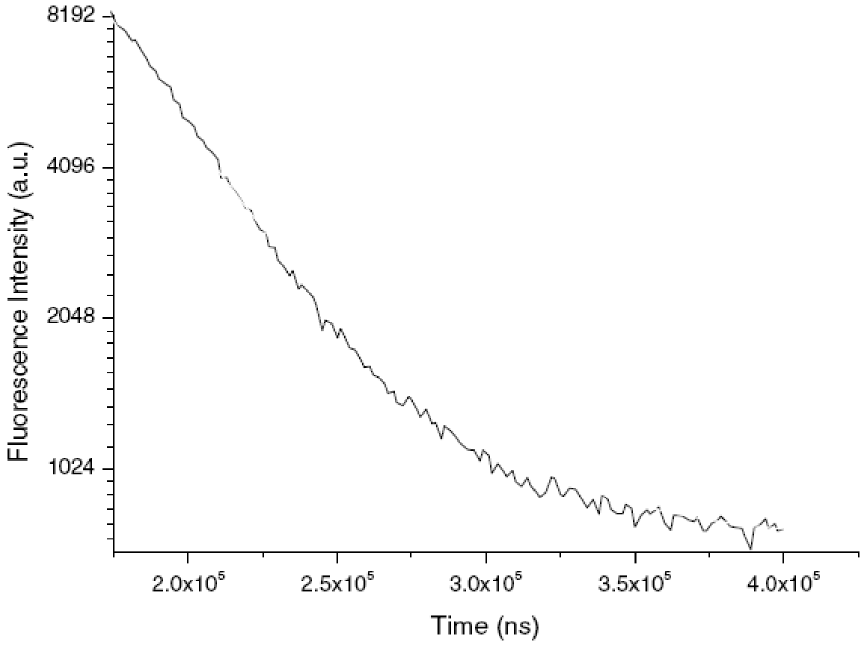

Fig. 4.4. Room temperature fluorescence decay curve of LaB_3O_6:Nd^{3+} crystal

Excited state	Wavelength (nm)	I (nm/cm)	S_{mea} (10^{-20} cm^2)	S_{cal} (10^{-20} cm^2)	f_{exp} (10^{-6})	f_{cal} (10^{-6})
$^4F_{3/2}$	860	35.86	0.411	0.778	1.656	0.329
$^4F_{5/2}$,$^2H_{9/2}$	799	240.81	2.969	2.885	6.810	6.891
$^4F_{7/2}$,$^4S_{3/2}$	744	221.79	2.937	3.081	0.163	0.379
$^4F_{9/2}$	674	41.89	0.612	0.210	1.595	0.970
$^4G_{5/2}$,$^2G_{7/2}$	579	127.94	2.177	2.204	4.900	3.633
$^2K_{13/2}$,$^4G_{7/2}$,$^4G_{9/2}$	524	79.91	1.502	1.114	6.426	6.507
$^2K_{13/2}$,$^2G_{9/2}$,$^2P_{3/2}$,$^4G_{11/2}$	470	20.92	0.483	0.267	1.533	0.532
$^2P_{1/2}$,$^2D_{5/2}$	428	1.77	0.041	0.095	6.746	7.708
$^4D_{3/2}$,$^4D_{5/2}$,$^2I_{11/2}$,$^4D_{1/2}$	356	51.26	1.418	1.435	6.351	6.171
$^4D_{7/2}$,$^2L_{17/2}$	328	10.58	0.318	0.063	0.816	1.547

Table 4.1. The integrated absorbance, the experimental and calculated line and oscillator strengths of Nd^{3+}:LaB_3O_6 crystal (note: rms $f = 0.744 \times 10^{-6}$)

Crystals	Ω_2 (10^{-20} cm^2)	Ω_4 (10^{-20} cm^2)	Ω_6 (10^{-20} cm^2)	References
LaB_3O_6	0.54	2.31	4.51	[80]
YVO_4	5.88	4.08	5.11	[81]
$CaZn_2Y_2Ge_3O_{12}$	0.94	3.25	3.68	[82]
$Sr_2GdGa_3O_7$	2.94	6.93	6.96	[83]
$Gd_3Ga_5O_{12}$	0.05	2.9	9.3	[81]
YAG	1.0	2.9	9.3	[81]
$Ca_3Sc_2Ge_3O_{12}$	0.99	4.24	7.14	[90]
$Lu_3ScGa_3O_{12}$	0.082	2.844	3.137	[84]

Table 4.2. The intensity parameters of Nd^{3+}:LaB_3O_6 crystal and the comparison of the intensity parameters of other Nd^{3+} doped crystals

Start levels	Wavelength (nm)	A	β (s^{-1})	τ (μs)
$^4I_{9/2}$	891	917.29	0.336	366.03
$^4I_{11/2}$	1062	1.47×10^3	0.538	
$^4I_{13/2}$	1329	326.55	0.12	
$^4I_{15/2}$	1852	17.05	6.24×10^{-3}	

Table 4.3. The calculated radiative probabilities,radiative branching ratios and radiative time for the emissions from the $^4F_{3/2}$ level of $LaB_3O_6:Nd^{3+}$

Crystals	Wavelength (nm)	σ_p (10^{-20} cm^2)	β	References
$NdAl_3(BO_3)_4$	1060	28.4	0.518	[85]
$CaSc_2Ge_3O_{12}:Nd^{3+}$	1060	2.6	0.37	[24]
$NdSc_3(BO_3)_4:Nd^{3+}$	1061	2.0×10^2	0.38	[86]
$La_2(WO_4)_3:Nd^{3+}$	1058	11.2	0.5098	[87]
$NdAl_3(BO_3)_4$	1063 (σ polarized)	16.0	0.52	[88]
	1063.5 (π polarized)	14.3	0.52	[88]
$Gd_{0.8}La_{0.2}VO_4:Nd^{3+}$	1063	33.2	0.498	[89]
$LaB_3O_6:Nd^{3+}$	1062	3.46	0.538	[80]

Table 4.4. The comparison of the $^4F_{3/2} \rightarrow {}^4I_{11/2}$ emission cross-section and radiative branching ratios of Nd^{3+} doped crystals.

4.3 The laser characteristics of Nd^{3+}-doped LaB_3O_6 crystal

A method utilizing an unprocessed Nd^{3+}-doped LaB_3O_6 crystal cleavage microchip as the solid-state laser gain medium was proposed by Prof. Huang[10]. Pumped by a Ti:sapphire laser at 871 nm, 1060 nm continuous-wave laser emission with slope efficiency of 23% has been achieved in an unprocessed microchip directly obtained from a cleavage $Nd^{3+}:LaB_3O_6$ crystal. Fig.4.5 shows the infrared laser output power at 1060 nm as a function of absorbed pump power at 871 nm. A maximum output power of 112 mW was obtained when the absorbed pump power was 580 mW. The laser performance of the unprocessed cleavage Nd^{3+}:LaBO microchip cannot compare with those of other microchip lasers yet, such as widely investigated Nd^{3+}:YAG and $Nd^{3+}:YVO_4$.[91~94]

5. Summary

The growth, thermal, optical and spectrum characteristics and laser characteristics of rare earth-doped $Ln_2Ca_3B_4O_{12}$ (Ln = La, Gd, or Y) double borate family laser crystals, $Ca_3(BO_3)_2$ and LaB_3O_6 laser crystals were reviewed.

From a passively mode-locked $Yb:Y_2Ca_3(BO_3)_4$ (Yb:CYB) laser, the 244 *fs* pulses with a repetition rate of ~55 MHz were obtained at the central wavelength of 1044.7 nm. The measured average output power amounted to 261 mW. Q-switching and Q-switched mode-locked $Yb:Y_2Ca_3B_4O_{12}$ lasers with an acousto-optic switch were also demonstrated. In the Q-switching case, an average output power of 530 mW was obtained at the pulse repetition rate of 10.0 kHz under the absorbed pump power of 6.1 W. The minimum pulse width is 79 ns at the repetition rate of 1.7 kHz. The pulse energy and peak energy are calculated to be 231 μJ and 2.03 kW, respectively. In Q-switched mode-locking case, the average output

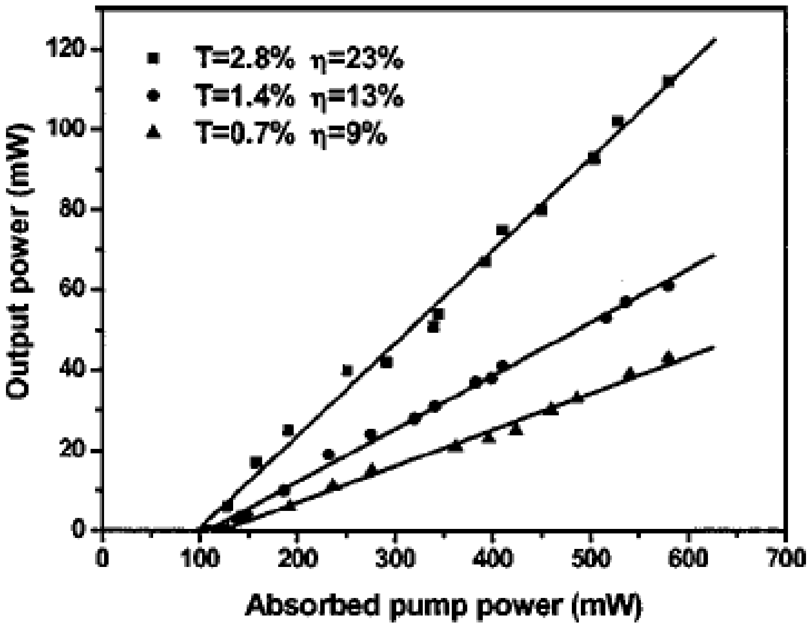

Fig. 4.5. Infrared laser output power at 1060 nm as a function of absorbed pump power at 871 nm

power of 64 mW with a mode-locked pulse repetition rate of 118 MHz and Q-switched pulse energy of 48 μJ was generated under the absorbed pump power of 6.1W. Meanwhile, Yb^{3+}-doped $Y_2Ca_3B_4O_{12}$ diode-pumped laser operation in continuous-wave (CW) was reached. The differential slopes of the CW output power are in the 22-40% range under different experimental conditions. Continuous tuning of the laser wavelength is obtained in the 1020-1057 nm range, in agreement with the broad emission spectra. Also, the diode-pumped multi-wavelength continuous-wave laser operation of the disordered $Yb:Ca_3Gd_2(BO_3)_4$ (Yb:CGB) crystal was reached. An output power of 1.4 W was obtained when quadruple wavelengths were emitted simultaneously, corresponding to a slope efficiency of 23.7%.

Finally, the laser property of microchip $Nd^{3+}:LaB_3O_6$ crystal are reviewed. Pumped by a Ti:sapphire laser at 871 nm, 1060 nm continuous-wave laser emission with slope efficiency of 23% has been achieved in an unprocessed microchip directly obtained from a cleavage $Nd^{3+}:LaB_3O_6$ crystal. A maximum output power of 112 mW was obtained when the absorbed pump power was 580 mW.

6. Acknowledgements

Some works of this chapter were supported by National Nature Science Foundation of China (50902129, 61078076, 91122033), Major Projects from FJIRSM (SZD09001), the Knowledge Innovation Program of the Chinese Academy of Sciences (KJCX2-EW-H03), Science and Technology Plan Major Project of Fujian Province of China (2010I0015).

7. References

[1] Xiuai Lu,Zhenyu You,Jianfu Li,et al., Journal of Crystal Growth,281(2-4)(2005) 416;

[2] Xiuai Lu, Master dissertation, The study of new－style rare earth doped $Ca_3(BO_3)_2$and $NaY(MoO_4)_2$ laser crystals, Graduated School of Chinese Academy of Sciences, 2006.

[3] P.H. Haumesser and R. Gaume et al., J. Crystal Growth 233 (2001), 233.

[4] Guohua Jia, Chaoyang Tu*,Zhenyu You, et al., J. Cryst. Growth, 266 (4) (2004)492;

[5] Chaoyang Tu, Yan Wang, Zhenyu You, Journal of Crystal Growth, 265(1-2)(2004) 154-158;

[6] Yan Wang，Chaoyang Tu*, ChangChang Huang, Journal of Materials Research 19 (4) (2004) :1204;

[7] E. Cavalli, E. Bovero, and A. Belletti, J. Phys.: Condens. Matter 14, 5221 (2002).

[8] Y. J. Chen, X. H. Gong, Y. F. Lin, et al., J. Appl. Phys. 99(2006)103101.

[9] Y. J. Chen, X. H. Gong, Y. F. Lin, et al., Appl. Phys. B 83(2006)195.

[10] Y. J. Chen, Y. D. Huang*, X. Q. Lin,et al., Appl. Phys. Lett. 86(2005)021115.

[11] A. Vegas, F.H. Cano and S. Carcia-Blanco, Acta Crystallographica B 31 (1975), 1416;

[12] H. Choosuwan, R. Guo, A.S. Bhalla, U. Balachandran, J. Appl. Phys. 91(2002):5051

[13] J.J. Carvajal, R. Sole, Jna. Gavalsa, et al. Chem. Matt. 15 (2003):2730;

[14] Xiuai Lu, Zhenyu You, Jianfu Li, et al., Journal of Crystal Growth, 281(2-4)(2005)416-425;

[15] Xiuai Lu, Zhenyu You, Jianfu Li, et al., Physica Status Solidi (a) 203 (2006)551;

[16] E. Cavalli, E. Bovero, and A. Belletti, J. Phys.: Condens. Matter 14(2002)5221;

[17] A. A. Kaminskii, in: Crystalline Lasers: Physical Processes and Operating Schemes (Boca Raton, FL: Chemical Rubber Company, 1996);

[18] H. R. Xia, X. L. Meng, M. Guo, L. Zhu, H. J. Zhang, and J. Y. Wang, J. Appl. Phys. 88, 5134 (2000);

[19] M. H. Randles, J. E. Creamer, and R. F. Bclt, Opt. Soc. Am. B 10(1998)289;

[20] T. Jansen, V. G. Ostroumov, J.-P. Meyn, G. Huber, A. I. Zagumennyi, and I. A. Scherbakov, Appl. Phys. B 58(1994)373;

[21] G. H. Jia, C. Y. Tu, J. F. Li, et al., Opt. Commun. 242 (2004)79;

[22] H. D. Jiang, H. J. Zhang, J. Y. Wang, et al., Opt. Commun. 198(2001)447;

[23] E. Cavalli, E. Zannoni, A. Belletti, V. Carozzo, A. Toncelli, M. Toncelli, and M. Bettinelli, Appl. Phys. B 68 (1999)677;

[24] A. A. Kaminskii, Zh. Tekh. Fiz. Pis. 1 (1975)256;

[25] R. C. Powell, in: Physics of Solid-State Laser Materials (Springer, New York, 1998)

[26] D. Jaque, O. Enguita, U. Caldino, G. M. O. Ramirez, J. Garcia Sole, C. Zaldo, J. E. Munoz-Santiuste, A. D. Jiang, and Z. D. Luo, J. Appl. Phys. 90(2001)561;

[27] Y. J. Chen, X. Q. Lin, and Y. D. Huang, Chem. Phys. Lett. 381(2003)598;

[28] Xiuai Lu, Zhenyu You, Jianfu Li, et al., J. Appl. Phys ,100(2006)033103;

[29] I. Sokólska, Appl. Phys. B: Lasers Opt. 71(2000)157;

[30] S. A. Payne, L. L. Chase, L.-K. Smith, L. Kway, and W. F. Krupke, IEEE J. Quantum Electron. 28(1992) 2619;

[31] G. S. Ofelt, J.Chem.Phys.37(1962)511

[32] S. Zhang, X. Wu, Y. Song, D. Ni, et al., J. Cryst. Growth 252(2003) 246;

[33] W. T. Carnall, P. R. Field, and K. Rajnak, J. Chem. Phys. 49(1968)4424;

[34] M. J. Weber, Phys. Rev. 157(1967)262;

[35] F. S. Ermeneux, R. Moncorge, P. Kabro, et al., OSA Trends Opt. Photon. Series 1(1996)498;

[36] Xiuai Lu, Zhenyu You, Jianfu Li, et al., Journal of Physics and Chemistry of Solids, 66(10)(2005)1801;

[37] S. Zhang, X. Wu, Y. Song, et al., J. Cryst. Growth 252 (2003)246.

[38] B.R. Judd, Phys. Rev. 127 (1962)750.

[39] B.V.Mill,A.M.Tkachuk et al. Opt.& Spec.84(1)(1998)65;

[40] Khamaganova,T.N.,Trunov.V.K.et al.Kristallografiva, 35(1990)856;

[41] W.bardsley,D.T.J.hurle & J.B.Mullin.(ed.)Crystal Growth: a tutorial Approach, North-Holland Publishing Company,1979:160;

[42] Chaoyang Tu, Yan Wang, Zhenyu You, et al.,Journal of Alloys and Compounds, 368(1-2)(2004)123;

[43] Chaoyang Tu, Yan Wang, Zhenyu You, et al.,Journal of Crystal Growth, 260(3-4)(2004)410;

[44] H.Jiang,J.Wang, H.Zhang et al.Chem.Phys.Lett. 361(2002)499;

[45] Gaume,B.Viana et al.Opt.Mater. 22(2003)107;

[46] W.F.Krrupke. Curr. Opin. Solid State Mater.Sci.4(1999)197;

[47] P.H.Haumesser,R.Gaume et al. J.Opt.Soc.Am.B, 19(10) (2002)2365;

[48] .H.Jiang, J.Li,J.Wang et al. J.Cryst.Growth. 233(2001)248;

[49] Chaoyang Tu, Doctor Dissertation,The study on the growth,structure,spectra and laser characteristics of new rare earth-actived laser crystals, Graduated School of Chinese Academy of Sciences,2005.

[50] Bruesselbach H, Umida D S. Optics Letter , 21(1996)480;

[51] Shimokozono M, Sugimoto N, Tate A and Katoh Y.Appl.Phys., 68(1996)2177;

[52] Payne S A, Deloash L D, Smith L K et al. J , . Appl. Phys., 76(1994)497;

[53] Deloach L D , Payne S A, Smith L K et al. J. Opt . Soc . Am ., B, 11(1994) 269;

[54] Kuleshov N V, Lagatsky A A, Shcherbitsky V G, et al . Appl. Phys., B64(1997)409;

[55] Yan Wang, Chaoyang Tu*, Zhenyu You, et al.,Optical spectroscopy of $Ca_3Gd_2(BO_3)_4$:Nd^{3+} laser crystal", Journal of Modern Optics, 53(8) (2006):1141-1148;

[56] Chaoyang Tu, Yan Wang, Zhenyu You, et al.,Optical Materials, 29(2-3)(2006)257;

[57] Hart D W, Jani M, Barnes N P. Optical Letters , 21(1996)728 Communications, 132(1996)107;

[58] Jojmson L F, Geusic J E & Van Uitert L G, Appl. Phys, Lett.,7(5)(1965)127;

[59] Bums G. Phys .Rev., 167(2)(1968)31;

[60] Reinberg A.R. Riseberg L A. Brown R M,et al .GaAs:Si IED Pue

[61] Chen Y , Majior L , and Kushawaha V. Applied Optics, 35(1996) 3203;

[62] Shen D, Wang C, Shao Z, Meng X. and Jian M. Appiled Optics, 35(1996)3203;

[63] Meyn J-P, Jensen T and Huber G.IEEE, Quantum ;

[64] Ostroumov V G, Heine F, K? ck S, et al. Appl. Pyhs ., B64(1997)301;

[65] Wang Guofu, Doctor Dissertation, in Thesis of Growth and optical Characterisation of Cr^{3+}, Ti^{3+}; and Nd^{3+} doped $RX_3(BO_3)_4$ Borate Crystals, 1996, University of Strathclyde UK;

[66] J.-L. Xu, J.-L. He, H.-T. Huang,et al., Laser Phys. Lett., 1–4 (2010) / DOI 10.1002/lapl.201010089 1;

[67] J.-L. Xu, J.-L. He, H.-T. Huang, et al.,Laser Phys. Lett. 7 (3) (2010)198;

[68] C.-Y. Tu · Y.Wang · J.-L. Xu et al., Appl Phys B 101(2010) 855;
[69] A.Brenier, Chaoyang Tu, Yan Wang,et al., Journal of applied physics,104(2008)013102;
[70] A. A. Lagatsky, A. Abdolvand, and N. V. Kuleshov, Opt. Lett. 25(2000)616;
[71] J. Liu, U. Griebner, V. Petrov, H. Zhang, J. Zhang, and J. Wang, Opt. Lett. 30(2005) 2427;.
[72] Y. Kalisky, C. Labbe, K. Waichman, L. Kravchik, U. Rachum, P. Deng, J. Xu, J. Dong, and W. Chan, Opt. Mater. (Amsterdam, Neth.) 19(2002)403;
[73] X. Zhang, A. Brenier, Q. Wang, Z. Wang, J. Chang, P. Li, S. Zhang, S. Ding, and S. Li, Opt. Express 13(2005) 7708;
[74] A. Brenier, C. Tu, Z. Zhu, and J. Li, Appl. Phys. Lett. 90(2007) 071103;
[75] Jin-Long Xu, Chao-Yang Tu, Yan Wang, Jing-Liang He, Optical Materials, In Press, Corrected Proof, Available online 5 July 2011;
[76] G.K. Abdullayev, Kh.S. Mamedov and G.G. Dzhafarov. Kristallografiya 26 (1981) 837.
[77] J.S. Ysker and W. Hofmann. Naturwissenschaften 57 (1970) 129.
[78] A.N. Shekhovtsov, A.V. Tolmachev, M.F. Dubocik et al.. Nucl. Instrum. Methods A 456 (2001) 280.
[79] E.F. Dolzhenkova, A.N. Shekhovtsov, A.V. Tolmachev et al.. J. Crystal Growth 233 (2001) 473.
[80] Guohua Jia, Chaoyang Tu, Jianfu Li, et al.,Optics Communications, 242(1-3)(2004) 79-85;
[81] A.A. Kaminskii, Crystalline Lasers, Physical processes and Operating Schemes, CRC Press, New York (1996).
[82] D.K. Sardar, S. Vizcarra, M.A. Islam, et al., J. Lumin. 60 (1994) 97.
[83] W. Koechner, Solid State Laser Engineering (third ed.), Springer, Berlin, Heidelberg (1992).
[84] A.A. Kaminskii, G. Boulon, M. Buoncristiani, et al., Phys. Status Solidi A 141 (1994) 471.
[85] Xueyuan Chen, Zundu Luo, D. Jaque, et al., J. Phys.: Condens. Mat. 13 (2001) 1171
[86] John B. Gruber, Thomas A. Reynolds, Douglas A. Keszler and Bahram Zandi, J. Appl. Phys. 87 (2000) 7159.
[87] Yujin Chen, Xiuqin Lin, Xiuqin Lin and Yidong Huang, Chem. Phys. Lett. 381 (2003)598.
[88] D. Jaque, O. Enguita, U. Caldino, et al., J. Appl. Phys. 90 (2001)561.
[89] H.D. Jiang, J.Y. Wang, H.J. Zhang, et al., J. Appl. Phys. 92 (2002)3647.
[90] K.A. Gschneidner and Le Roy Eyring, Handbook on the Physics and Chemistry of Rare Earths vol. 9, North Holland (1987) pp. 11.
[91] T. Sasaki, T. Kojima, A. Yokotani, O. Oguri, and S. Nakai, Opt. Lett. 16(1991)1665;
[92] G. J. Spuhler, R. Paschotta, M. P. Kulloerg, M. Graf, M. Moser, E. Mix, G. Huber, C. Harder, and U. Keller, Appl. Phys. B: Lasers Opt. 72(2001)285;
[93] V. Lupei, N. Pavel, and T. Taira, Appl. Phys. Lett. 80(2002)4309;
[94] Y. Sato, T. Taira, N. Pavel, and V. Lupei, Appl. Phys. Lett. 82(2003)844;

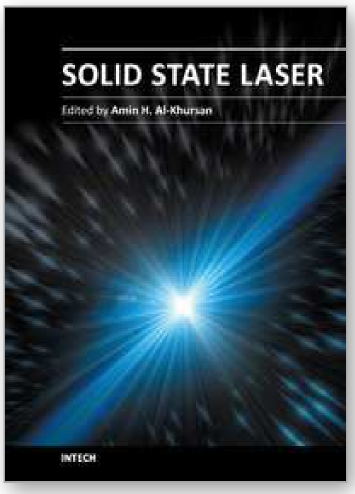

Solid State Laser

Edited by Prof. Amin Al-Khursan

ISBN 978-953-51-0086-7
Hard cover, 252 pages
Publisher InTech

This book deals with theoretical and experimental aspects of solid-state lasers, including optimum waveguide design of end pumped and diode pumped lasers. Nonlinearity, including the nonlinear conversion, up frequency conversion and chirped pulse oscillators are discussed. Some new rare-earth-doped lasers, including double borate and halide crystals, and feedback in quantum dot semiconductor nanostructures are included.

Chaoyang Tu and Yan Wang (2012). The Recent Development of Rare Earth-Doped Borate Laser Crystals, Solid State Laser, Prof. Amin Al-Khursan (Ed.), ISBN: 978-953-51-0086-7, InTech, Available from: http://www.intechopen.com/books/solid-state-laser/the-study-on-some-new-rare-earth-doped-borate-laser-crystals

INTECH
open science | open minds

InTech Europe
University Campus STeP Ri
Slavka Krautzeka 83/A
51000 Rijeka, Croatia
Phone: +385 (51) 770 447
Fax: +385 (51) 686 166
www.intechopen.com

InTech China
Unit 405, Office Block, Hotel Equatorial Shanghai
No.65, Yan An Road (West), Shanghai, 200040, China
中国上海市延安西路65号上海国际贵都大饭店办公楼405单元
Phone: +86-21-62489820
Fax: +86-21-62489821